Micromachined fiber optic accelerometer based on intensity modulation

Dissertation

Submitted to the faculty of Sciences of the University of Neuchâtel, in fulfillment of the requirements for the degree of "*Docteur ès Sciences*"

by

Benedikt Guldimann

Diplômé en électronique-physique

de l'Université de Neuchâtel

Institute of Microtechnology

University of Neuchâtel

Rue Jaquet-Droz 1, CH – 2007 Neuchâtel

Switzerland

April 2001

IMPRIMATUR POUR LA THESE

Micromachined fiber optic accelerometer based on intensity modulation

de M. Benedikt Guldimann

UNIVERSITE DE NEUCHATEL

FACULTE DES SCIENCES

La Faculté des sciences de l'Université de Neuchâtel sur le rapport des membres du jury,

MM. N. de Rooij (directeur de thèse)
H.-P. Herzig et C.R. Marxer, Neuchâtel

autorise l'impression de la présente thèse.

Neuchâtel, le 27 mars 2001

Le doyen:

J.-P. Derendinger

Abstract

The present thesis was devoted to the development of a silicon micro-machined fiber optic based accelerometer based on low cost components. By using microfabrication technologies, structures with mechanical, optical and packaging functions allowed an increased design and fabrication simplicity combined with a significant performance improvement. The accelerometer mass displacement resolution has dropped 100-fold for micromachined intensity modulated fiber optic accelerometers, from 10 nm to 1 Angström. For this type of devices the dynamic range was improved by a factor 6. These improvements allowed to reach displacement measurement performances equal to a significantly more sophisticated and expensive wavelength dependent measurement method.

The approach of the presented work is based on the principle of a maximal simplicity in theory, design, fabrication, light source and detection means. The first part of the work analyzes therefore the simplest micro-opto-mechanical approach to obtain a displacement response equivalent to the response of a single segment of a segmented photodiode. In order to show the principle on a working device, a simple accelerometer is presented. It shows that a displacement resolution of 1nm can be reached In the second part of the work shows how the fabrication process can be simplified to a single mask process and how damped resonance and immunity to light

source fluctuations can be reached. A differential displacement detection with two photodiodes is performed. Chapter 5 presents the final micro-machined equivalence to a segmented photodiode. This accelerometer has integrated damping structures, a dynamic range close to 40 dB and an estimated mass displacement detection resolution below an angström over a bandwidth of 300 Hz. This represents an improvement of again a factor ten compared to the device of chapter 3 and has a displacement resolution equivalent to a Fabry-Perrot based device.

Table of contents

1 Introduction 1

1.1 Motivation 1

1.2 History 2

1.3 The situation at the beginning of this work 9

1.4 Introduction to the following chapters 15

2 Micromachined shutter for multimode optical fiber transmission modulation 19

2.1 Fiber optic shutter modulation 19

2.1.1 Numerical calculation of multimode fiber coupling with shutter 33

2.2 Microfabrication of a test structure for shutter modulation 40

2.2.1 Design considerations 40

2.2.2 Fabrication process 41

2.3 Characterization of the test structures for shutter modulation 45

2.3.1 Experimental set-up and measurements 45

2.3.2 Measurements and results with an LED source 50

3 Micromachined accelerometer based on optical fibers 55

3.1 Basic principle 55

3.2 Accelerometer mass displacement detection with shutter modulation 59

3.3 Mechanical design considerations 62

3.4 Fabrication 65

3.5 Characterization 67

3.6 Conclusions of the first generation accelerometer 70

4 Fiber optic MEMS accelerometer with integrated damping 72

4.1 Introduction to viscous damping 72

4.2 Gas-damped accelerometer 78

4.3 System design considerations 87

4.4 Fabrication 95

4.5 Characterization 100

4.6 Conclusions 102

5 Fiber optic MEMS accelerometer with high mass displacement resolution 105

5.1 detection electronics 105

5.2 Accelerometer design considerations 107

5.3 Characterization 110

5.4 Conclusions 112

6 Conclusions 116

1 Introduction

1.1 Motivation

The combination of fiber optics and micromachining has recently become of great interest for telecommunication products such as optical switches and attenuators. A lot of effort has therefore been undertaken to solve various packaging, optical coating and other technical problems. Fiber packaged optical components such as light emitting diodes (LED's) and detectors are now readily available. But optical micro electro mechanical system (MEMS) components are not limited to telecommunications applications. A fiber optic-based MEMS can also be a sensor. The main advantages of fiber optic sensors are their immunity to electromagnetic interference (EMI), and the capability of operation in hazardous environments and high temperatures [1]. However, except for some pressure sensors for high temperature applications, no fiber optic-MEMS device has found its way to the market. In the work presented here, the goal is to fabricate a fiber optic-based accelerometer with low-cost components with an eye ultimately to low-cost fabrication.

1.2 History

To our knowledge, the first accelerometer based on the combination of optical fibers and micromachined components was reported in 1984 by C. Ovrén, M. Adolfsson and B. Hök of the Asea company (now Asea Brown Boveri) [2,3]. Three patents deal with the accelerometer and its components [4,5,6]. Later, a great variety of fiber optic or wave-guide based micromachined accelerometers were published. Most of them are based on light intensity modulation [7,8,9,10], interferometric [11] or wavelength dependent [12,13] methods.
The device fabricated by Asea incorporates a lot of innovative approaches, which will be briefly discussed here. It is based on a micromachined silicon cantilever beam, with a small frame bonded to the end of a multimode optical fiber (fig 1.1). The air cushion between the cantilever and optical fiber surface is used for a viscous damping of the resonant structure. The sensor is excited from a light emitting diode through a multi-mode fiber. Two signals are generated in the sensor, one mechanically modulated signal proportional to the sensor acceleration and one reference signal which compensates for loss in the transmission path. Angular deflection of the beam due to spring-mass action causes a modulation of the reflected light intensity. The optical reference signal is generated by the same element by means of photoluminescence. This process does not exhibit the angular dependence of the reflected light. The ratio between the two signals is essentially independent of common intensity variations in the system. However, the specific cantilever-fiber arrangement [2] probably had a non-symmetric and nonlinear light power amplitude versus acceleration direction

response according to [14]. A direct time-dependent measurement and an acceleration amplitude response were unfortunately never shown for this device.

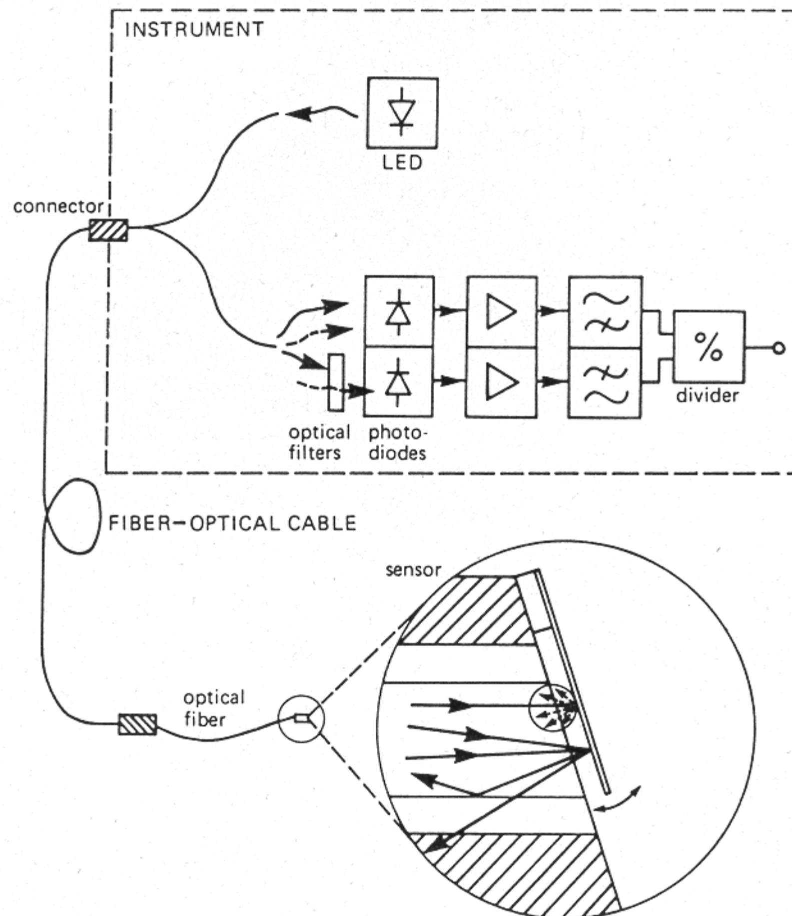

Fig 1.1: A fiber optic system for vibration monitoring by means of acceleration measurement. Light from an LED in the instrument is reflected back into the optical fiber at the sensor, the reflection being modulated by the acceleration of the sensor. The modulation of the returned light is detected in the optoelectronics as a measure of the acceleration. A reference signal is created by a wavelength conversion process in the sensor [5].

The same company patented a second cantilever-to-fiber arrangement with a vertically cleaved fiber tip (fig. 1.2) [5]. As the cantilever beam is bent under

acceleration the optical beam reflected back into the collimating lens is deflected. This induces a light coupling loss at the lens-fiber interface and therefore intensity modulation. The drawback of this method is that the light power loss are the same for a cantilever bent to the right and to the left. This leads to an accelerometer system with undefined acceleration direction. Later, other approaches based on intensity modulation were proposed. They generally had low sensitivity, did not detect the acceleration direction [5,7,8] or needed to be bonded to conventionally fabricated structures [9]. The devices published by Burcham et al. [7] and Uttamchandani et al. [8] cannot detect the acceleration direction since wave-guide to wave-guide coupling loss are the same under upwards and downwards cantilever deflection (figures 1.3 and 1.4). The device published by Malki et al. [9] overcame the problem of the undetermined acceleration direction but was based on a conventional mirror (fig. 1.5) which had to be aligned and bonded to the micromechanical structure. An integrated optical wave-guide accelerometer [10] also overcame the problem of the undetermined acceleration direction but was still not very sensitive (fig. 1.6). Its mass displacement resolution was about 10 nm over a frequency bandwidth of 450 Hz.

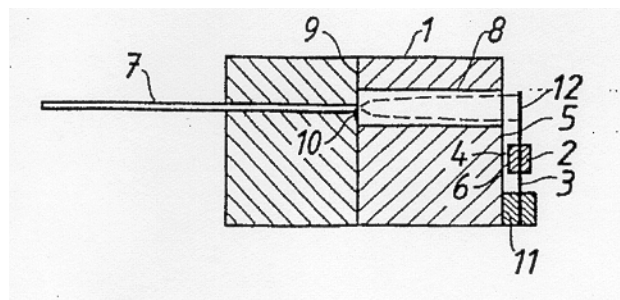

Figure 1.2: Fiber optic accelerometer drawing taken from patent [5]. In front of the optical fiber (7) there is a collimating lens. The light beam is reflected on the cantilever beam (12).

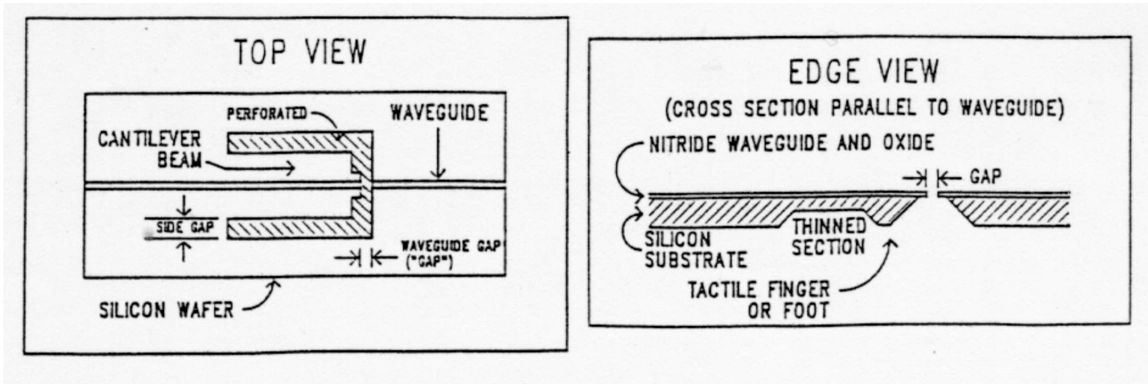

Figure 1.3: Two views of the cantilever beam accelerometer with integrated wave-guides published by Burcham et al. [7].

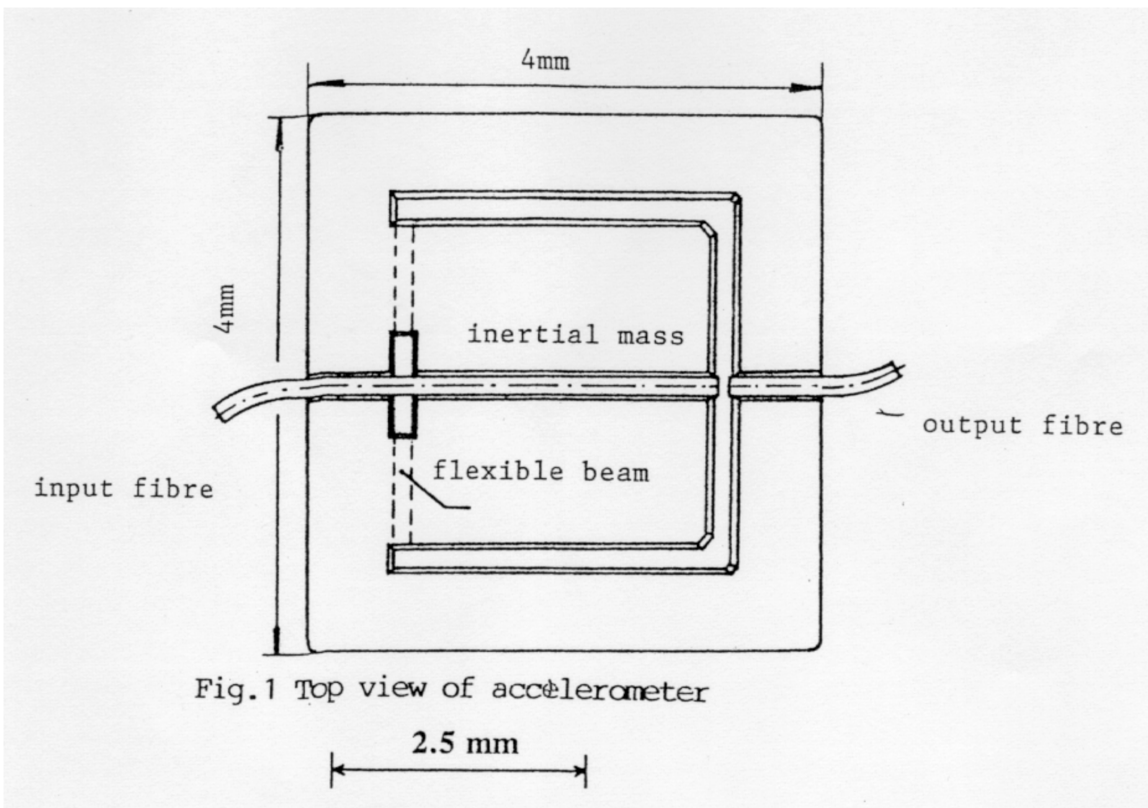

Figure 1.4: Top view of a micromachined cantilever fiber optic accelerometer published by Uttamchandani et al. [8].

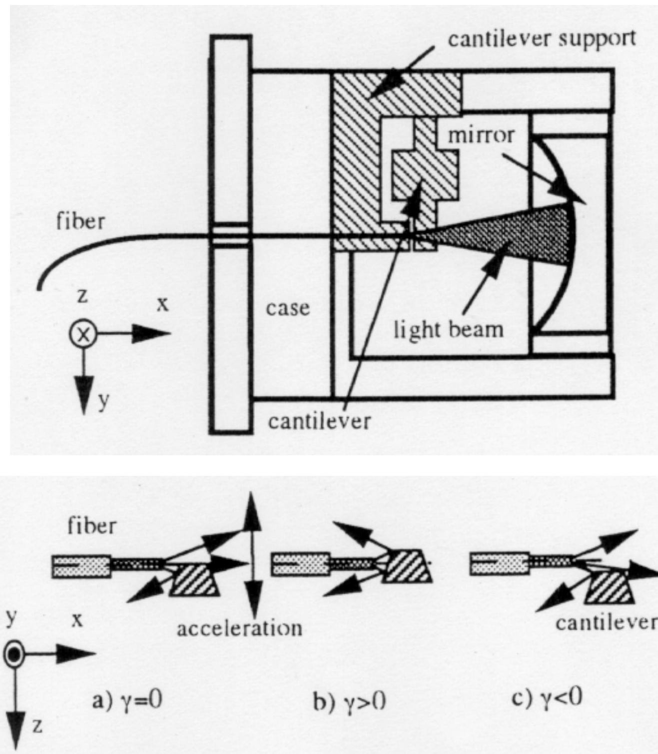

Figure 1.5: Top: Sensor head top view. Bottom: Principle cantilever positions. Figures from [9].

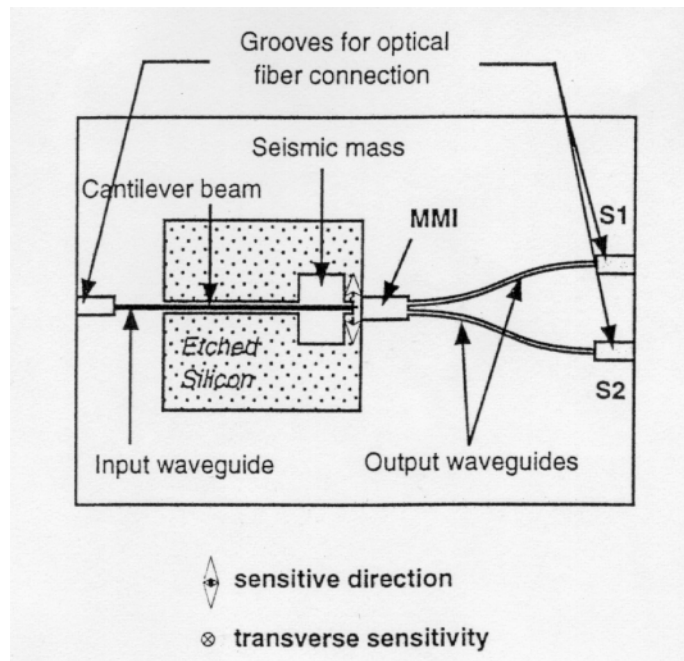

Figure 1.6: Sensor head top view. Figures from [10].

Various fiber optic-MEMS accelerometers based on measurement techniques other than intensity modulation were published [11,12,13]. For instance a wave-guide based accelerometer using an interferometric measurement technique [11] was published in 1998. In the same year a two-axis fiber optic based accelerometer (fig. 1.7) using a Fabry-Perrot measurement technique was presented by Schröpfer [12]. He used a broadband light source coupled to an optical fiber. The air gap between the accelerometer mass and the fiber end served as a low finesse Fabry-Perrot cavity. As the mass was moving, a shift in the central wavelength of the reflected part was observed. The acceleration was then detected through an external integrated wave-guide interferometer based wavelength detection system. It showed an estimated displacement resolution below an Angström. An opto-mechanical accelerometer based on strain sensing by a Bragg grating in a planar wave-guide was published by Storgaard [13]. He also used a broadband light source coupled to an optical fiber. The Bragg grating on the chip (fig. 1.8) reflected a narrow-band wave. As the mass was moving the grating was compressed or extended which induced a shift in the central wavelength of the reflected part of the light. The acceleration was then detected through an interferometer based wavelength detection system.

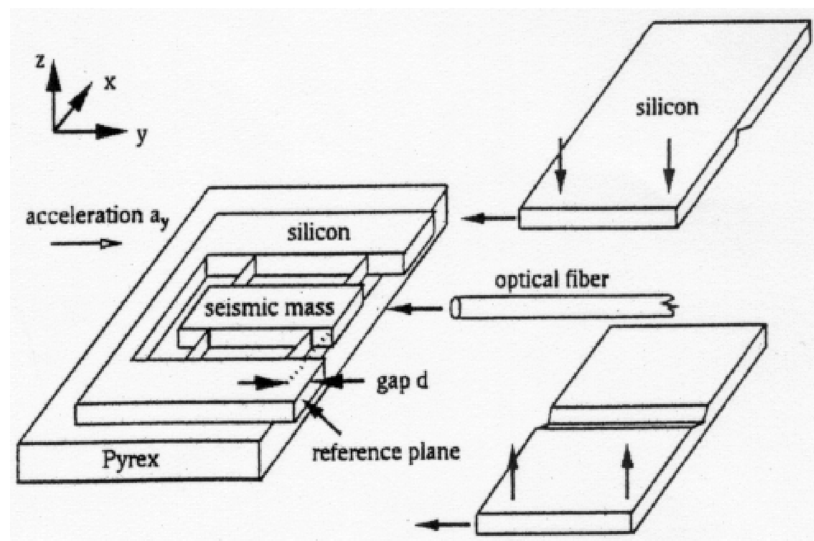

Fig. 1.7: Schematic (from Schröpfer [12]) of the opto-mechanical silicon sensor based on a Fabry-Perot cavity between the optical fiber and the seismic mass

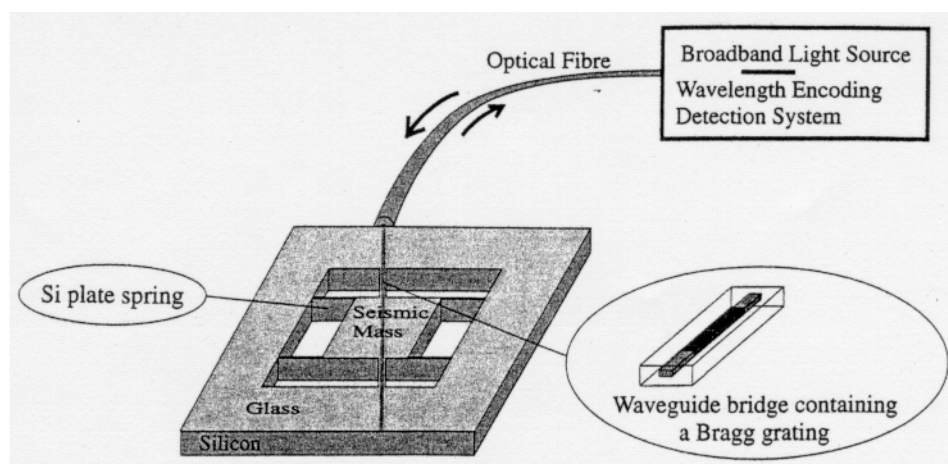

Fig. 1.8: Opto-mechanical accelerometer based on a Bragg grating as strain sensing element. Drawing taken from [13].

The advantage of intensity modulation techniques is that they require only an LED as light source and simple detection electronics. However, they generally exhibit a lower sensitivity [1]. The other optical measurement techniques used for acceleration measurements require a clearly more expensive fiber coupled laser diode [11] or super-luminescent diode,

integrated wave-guide modulator and interferometer [12] or a whole external conventional interferometer [13] as basic components, but are characterized by higher sensitivity. A purely mechanical characteristic of micromachined accelerometers is the damping of the resonant structure. It is important to damp the resonance to protect the mechanical structure against breakage, to increases the usable acceleration frequency bandwidth and to avoid detection signal non-linearity. Except of the first accelerometer [2] all previously mentioned accelerometers had a non-damped resonance.

1.3 The situation at the beginning of this work

State-of-the-art for fiber optic and waveguide-based accelerometers at the time this thesis research was begun in 1999 is described above. At the same time the telecommunications market was booming and a lot of effort to develop micromachined device solutions for optical switching was being, and continues to be expended [15]. Marxer [16] presented an optical switch in which the wave comb actuator structures, the fiber grooves and the moving vertical mirror are etched in one process step using deep reactive ion etching (DRIE) [17]. The degree of freedom offered by this technique allows the fabrication of not only active optical MEMS components such as switches, attenuators and spectrometers [18] but also passive ones, such as accelerometers [19,20].

Table 1.1: Fiber Optic MEMS Accelerometers up to 1999. The italic written rows correspond to an accelerometer based on a wavelength dependent detection method.

	Dyn. range	Displacement resolution	referenced	Damped resonance	Fabrication complication	Component costs
1984 [2]	-	-	yes	yes	2	low
1992 [7]	-	-	no	no	2	moderate
1992 [8]	-	-	no	no	2	moderate
1995 [9]	700	-	yes	no	3	low
1996 [11]	-	-	*yes*	*no*	*3*	*high*
1997 [10]	1400	10nm	Yes	no	2	moderate
1998 [13]	-	-	*yes*	*no*	*2*	*high*
1998 [12]	*10000*	*1A*	*yes*	*no*	*2*	*high*

The low displacement sensitivity of the light intensity modulation technique used in optical MEMS components is generally accepted. Conventional intensity modulated devices, such as atomic force microscopes (AFM), which are based on segmented photodiodes [21] however can detect cantilever beam deflections below an angström for a detection bandwidth of several hunderts of kilo-Herz. In actual facts it is angular deflection rather than pure displacement which is being determined. However it is noteworthy that a segmented photodiode costing $10 and illuminated by a deflected laser beam are enough to get measurements of atomic resolution. The principle is explained, among others, by Sarid [22] (fig. 1.9). The effectiveness of the measurement is due to an imbalance in the power incident on two side-by-side photo-detectors (fig 1.9). A typical response curve of the two photo detectors for displacements of a light spot is shown in figure 1.10.

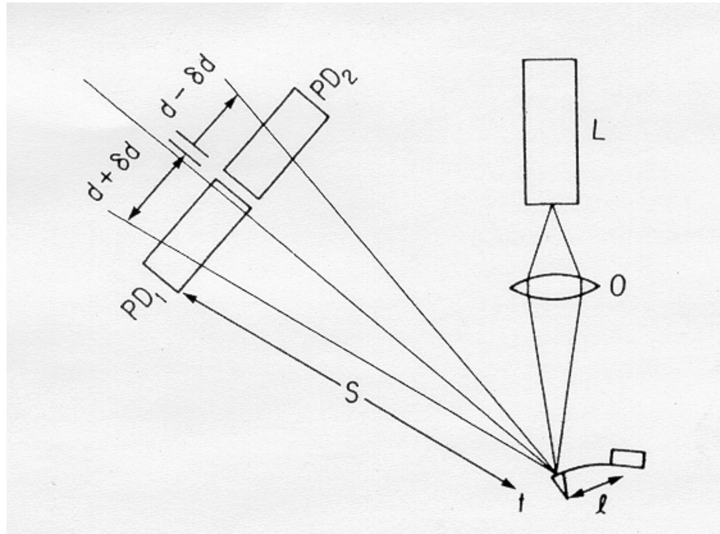

Figure 1.9: The trajectory of the laser beam that is focused by the objective (0) on the micro-machined lever (l) and is reflected onto two photo-detectors (PD1 and PD2). As the lever is bent, the laser beam is deflected by δd and a light power imbalance between the photodiodes is obtained.

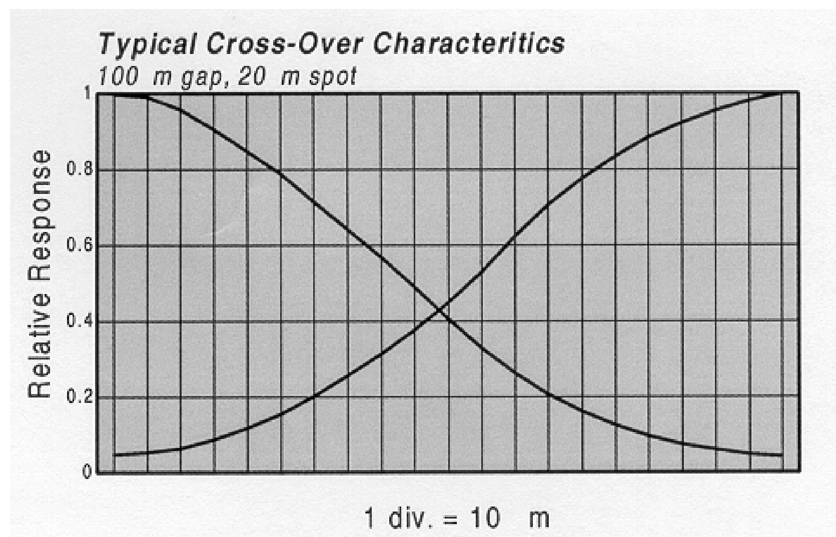

Figure 1.10: Typical response of a segmented photo detector with photo diodes lying side by side illuminated by a light spot of 100 mili-inch in diameter. As the light spot is completely on the left, the whole light power is detected by the left photodiode. As the light spot is exactly in the middle of both photodiodes both get the same response. It's in this situation where the slope of the response curves is maximal and it's the point where

the highest displacement sensitivity is reached. For small displacements around this point the response is linear.

In the case of an accelerometer where a small mass displacement has to be measured the light power unbalance using two photodiodes has also been used [23]. The device published by Bochobza-Degani (figure 1.11) was using a CMOS chip with two photodiodes under the silicon micromachined mechanical part of the accelerometer. On top of this assembly an LED was mounted. For this device the authors did not mention the mass displacement resolution. This accelerometer shows however some clear drawbacks. Its mechanical resonant structure is not damped, the three-component assembly is not simple and the optomechanical sensor includes electronic components. In the design of Bochobza-Degani [23] it is the outer part of the light spot emitted from the LED which is detected and not, what a higher efficiency would suggest, the central part where intensity is highest. The effectiveness and simplicity of the power imbalance principle was therefore not fully exploited.

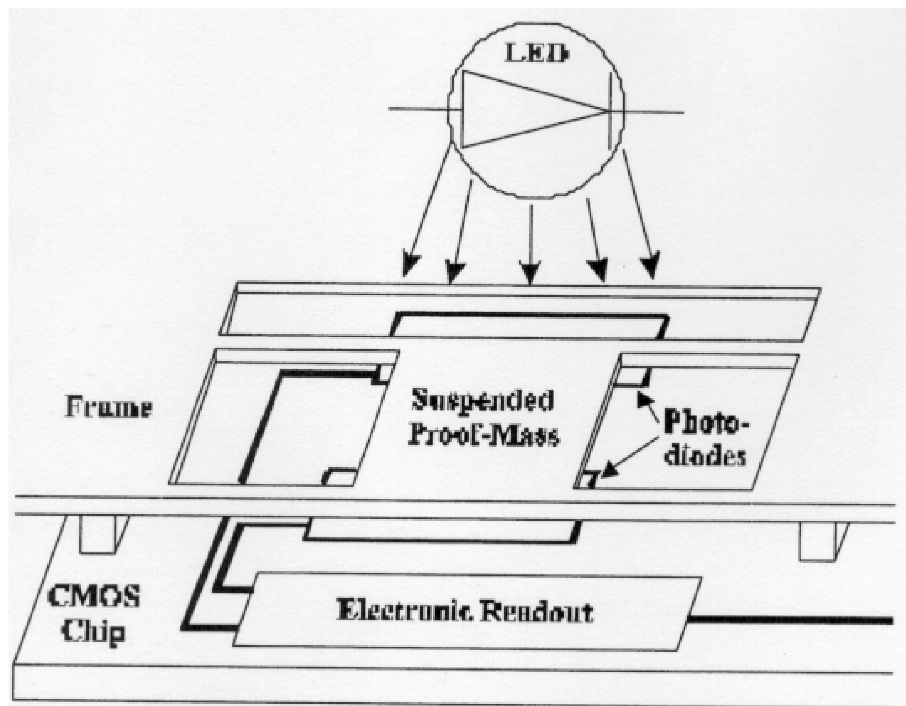

Figure 1.11: Schematic view (from Bochobza-Degani [23]) of the accelerometer's microsystem using a CMOS chip with signal processing and two photodiodes under the silicon micromachined mechanical part of the accelerometer. On top of this assembly an LED is mounted.

To optimize this simple method to measure an as small mass displacement as possible, the light power imbalance due to a certain displacement has to be as important as possible. In the case where the light power of the source is limited this could be reached for instance by reducing the light spot diameter illuminating the segmented photodiode. In the case of a micro-opto-mechanical sensor the natural "wire" is an optical fiber. In this way the immunity against electromagnetic fields is insured also along the fiber. The light source and detection electronics can be packaged in a shielded box remote from the sensor head. The core diameter of silica optical fibers can vary from 3 μm up to 200 μm depending on the light wavelength and type of fibers.

The goal of the work described in this thesis is to explore the power imbalance method using a micro-mechanical device in conjunction with optical fibers. To replace the conventional segmented photodiodes on the device chip, particular arrangements of self aligned optical fibers in micromachined structures are proposed. The next figure (fig. 1.12) shows one way to detect a power imbalance using only optical fibers and micromachined structures.

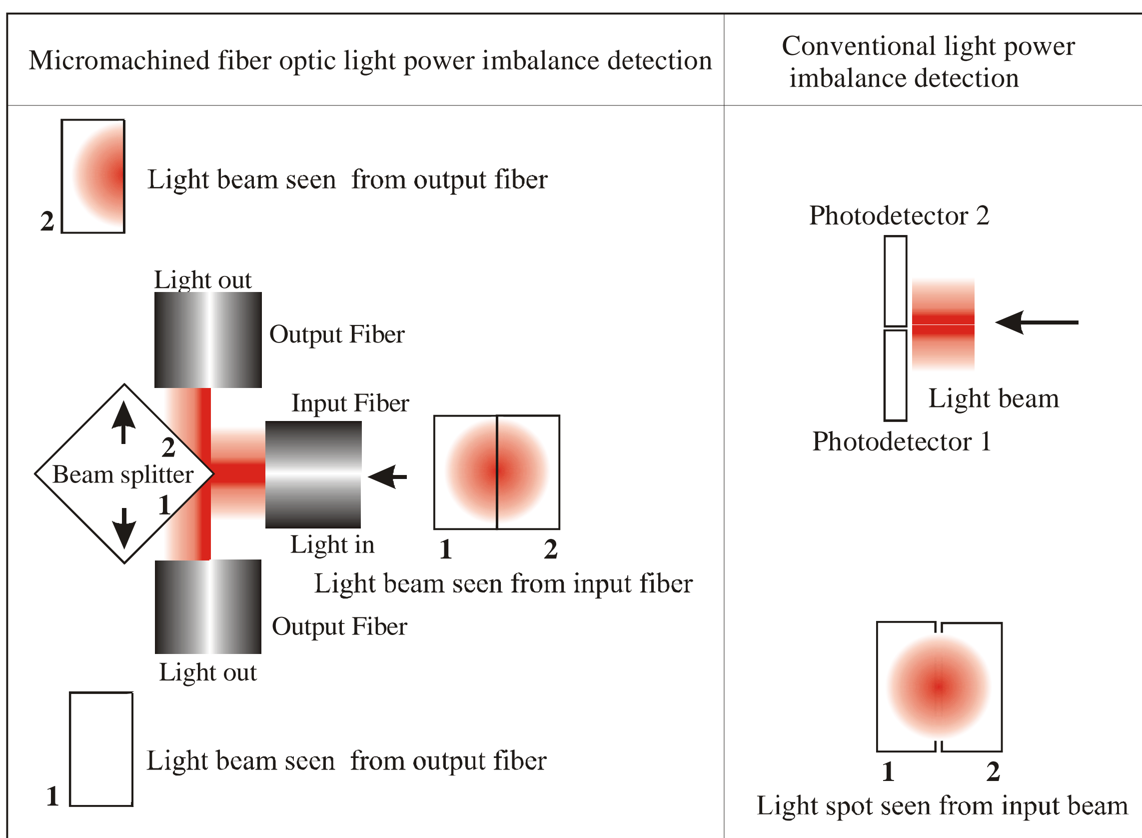

Figure 1.12: On the right: Conventional light beam position detection with a segmented photodiode. Left: Micromachined beam splitter position detection with optical fibers (Chapter 5)

1.4 Introduction to the following chapters

The approach of the presented work is based on the principle of a maximal simplicity in theory, design, fabrication, light source and detection means. The next chapter analyzes therefore the simplest micro-opto-mechanical approach to obtain a displacement response equivalent to the response of a single segment of a segmented photodiode. In order to show the principle on a working device, a simple accelerometer is presented [19]. This is done in chapter 3. It shows that a displacement resolution of 1nm can be reached which is already a factor 10 better compared to another intensity modulated device published recently [10]. A similar device, from the principle point of view, to the one presented here has been published by Malki [9], but he used a much larger core diameter and a conventionally fabricated mirror. Chapter 4 shows how the fabrication process can be simplified to a single mask process and how damped resonance and immunity to light source fluctuations can be reached [20]. A differential displacement detection with two photodiodes is performed. Chapter 5 presents the final micro-machined equivalence to a segmented photodiode. This accelerometer has integrated damping structures, a dynamic range close to 40 dB and an estimated mass displacement detection resolution below an angström over a bandwidth of 300 Hz. This represents an improvement of again a factor ten compared to the device of chapter 3 and has a displacement resolution equivalent to a Fabry-Perrot based device [12].

References:

[1] A. J. Jacobs-Cook,”MEMS versus MOMS from a systems point of view”, J. Micromech. Microeng., 6, (1996) 148-156.

[2] C. Ovrén, M. Adolfsson and B. Hök, ”Fiber-Optic systems for temperature and vibration measurements in industrial applications”, Optics and Lasers in Engineering, 5 (1984), 155-172.

[3] L. Jonsson and B. Hök, “Multimode fiber-optic accelerometers” SPIE 514 (1984), pp. 191-194.

[4] EP 0 096 262 A1, European Patent, ASEA, 1983.

[5] EP 0 151 958 B1, European Patent, Takaoka Electric, 1985.

[6] EP 0 151 957 A2, European Patent, ASEA, 1985.

[7] K. Burcham, G.N. De Brabander and J.T. Boyd, “Micromachined silicon cantilever beam incorporating an integrated optical waveguide”, SPIE 1793, (1992), 12-18.

[8] D. Uttamchandani, D. Liang and B. Culshaw, “A micromachined silicon accelerometer with fiber optic interrogation”, SPIE 1792, (1992), 27-33.

[9] J. Marty, A. Malki, C. Renouf, P. Lecoy, F. Baillieu, “Fiber-Optic accelerometer using silicon micromachined techniques”, Sensors and Actuators A 46-47 (1995), 470-473.

[10] E. Ollier, P. Lebey and P. Mottier, “Integrated micro-opto-mechanical vibration sensor connected to optical fibers”, Electron. Lett. (1997), 6, 525-526.

[11] Dan Haronian, “Geometrical modulation-based interferometry for displacement sensing using optically coupled suspended waveguides”, J. MEMS Vol. 7, Nr. 3, (1998), 309-314.

[12] G. Schröpfer, W. Elflein, M. de Labachelerie, H. Porte, S. Ballandras, ”Lateral optical accelerometer micromachined in (100) silicon with remote readout based on coherence modulation”, Sensors and Actuators A 68 (1998), 344-349.

[13] T. Storgaard-Larsen, S. Bouwstra, O. Leistiko, “Opto-mechanical accelerometer based on strain sensing by a Bragg grating in a planar waveguide”, Sensors and Actuators A52 (1996) 25-32.

[14] K. M. Taylor, “Misalignment losses in fiber optic joints due to angular misalignment for arbitrary energy distribution”, Opt. Eng. 34 (1995), 12, 3471-3479.

[15] Proceedings Int. Conf. Optical MEMS 2000 IEEE/LEOS, 00EX399

[16] C. Marxer, Ch. Thio, M.A. Grétillat, N.F de Rooij, R. Bättig, O. Anthamatten, B. Valk, P. Vogel, “Vertical mirrors fabricated by deep reactive ion etching for fiber-optic switching applications”, J. MEMS 6 (1997), 3, 277-285.

[17] P.A. Clerc et al., “Advanced deep reactive ion etching: a versatile tool for microelectromechanical systems”, J. MEMS, (1997), 6, 277-285.

[18] O. Manzardo, B. Guldimann, C. Marxer, N.F. de Rooij, H.P. Herzig, “Optics and actuators for miniaturized spectrometers”, Proc. IEEE Optical MEMS 2000, 24-25.

[19] B. Guldimann, P. Thiébaud, N.F. de Rooij, “Micromachined, fiber-optic based accelerometer with shutter modulation”, Proc. IEEE, MEMS 2000, 710-714.

[20] B. Guldimann, P.A. Clerc, N.F. De Rooij, “Fiber optic MEMS accelerometer with integrated damping”, Proc. IEEE Optical MEMS 2000, 141-142.

[21] UDT Sensors, Technical Catalogue, 2000.

[22] D. Sarid, “Scanning force microscopy”, Oxford Univ. Press 1991, pp. 119-121.

[23] O. Bochobza-Degani, D.J. Seter, E. Socher, S. Kaldor, E. Scher and Y. Nemirowsky, “Comparative study of novel micro-machined accelerometer employing MIDOS”, Proc. IEEE MEMS 99, pp 191-195.

2 Micromachined shutter for multimode optical fiber transmission modulation

2.1. Fiber optic shutter modulation

Shutter modulation is one of the simplest extrinsic fiber optic sensing principles. It can be realized in the transmission or reflection mode as shown in (fig. 2.1). Transmission mode is independent of the optical quality of the shutter. The shutter needs only to block the light beam. However, this configuration requires an input and an output fiber. There are two possible configurations for the reflection mode, either direct shutter reflection or reflection from an additional reflector (fig. 2.2). An additional reflector is required if the shutter cannot be fabricated with a sufficient reflective surface to redirect the light beam back into the optical fiber. The reflection mode does have the advantage that it requires only one fiber connected to the sensor, but an additional fiber splitter between light source and sensor head is also necessary. The transmission mode seems therefore to be the simplest approach for realizing shutter modulation.

Shutter modulation with multimode optical fibers

Shutter modulation can be achieved with two self-aligned optical fibers separated by a certain air gap through which a shutter can move perpendicularly to the central propagation axis of the optical fibers (fig. 2.1(a)). As the shutter moves up or down,

more or less light is coupled from the input fiber to the output fiber. The primary role of the shutter in this case is to introduce a light power loss-based modulation. The total effect of this arrangement depends on how the input fiber emits into the air gap, on the shape and position of the shutter and how the shuttered light beam is coupled into the output optical fiber.

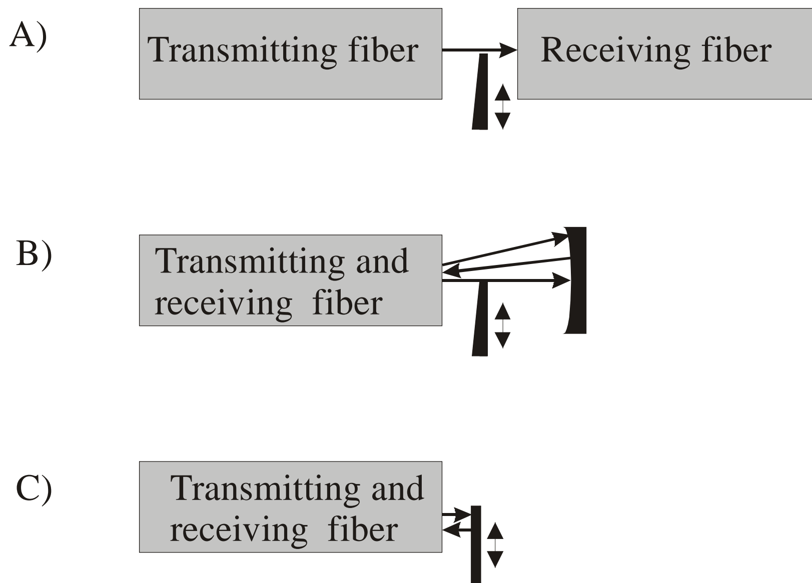

Figure 2.1: Different arrangements for shutter modulation: (A) transmission mode, (B) reflection mode with additional reflector, (C) reflection mode with reflecting shutter.

Most of the following text dealing with the propagation and coupling theory is taken from the book written by Miller [3]. The propagation of light is most accurately described by Maxwell's equation for the electromagnetic field [1]. However, the complexity of the solutions to these equations for all but the simplest wave-guiding structures tends to obscure the basic underlying physical principles and phenomena. Maxwell's equations describe the interaction of the electric and magnetic fields that together constitute the physical description of light. The difficulty with this approach is that a field, being a specification of a quantity at all points in space and its evolution in time, is hard to visualize and comprehend. In

general it is easier to understand a localized phenomenon, a particle, and its evolution with time, the trajectory. In the particulate theory of light (geometric optics) the ray path is the trajectory of a “particle” of light [2]. Although geometric optics cannot be used to describe many optical phenomena (diffraction, interference), the physical intuition gained from this approach can provide an understanding of many optical phenomena by simplifying the analysis of the more exact field (wave) theory. Strictly speaking, geometric optics is the limiting case of electromagnetic theory as the wavelength of light tends to zero ($\lambda \rightarrow 0$). If the core diameter is much larger than the wavelength of light ($\lambda/a << 1$), then geometric optics is accurate. These conditions hold for most multimode optical fibers, so that many aspects of light propagation in multi-mode optical fibers, including the loss in fiber connectors and splices [3], are accurately quantified by a geometric optics approach.

Multimode fiber coupling theory

As explained before, the coupling loss between multimode fibers can be quantified using a geometric optics approach. For single mode fibers where the core diameter is only a few factors higher than the wavelength of the light the geometric optics approach cannot be used. Therefore the coupling behavior between multi-mode fibers only can be predicted intuitively.

Shutter modulation as previously explained can be obtained with two aligned multi-mode fibers separated by a small air gap. In this air gap, a thin shutter introduces varying losses of the optical beam propagating from one fiber to the next. To model this shutter modulation, the coupling behavior between two multi-mode fibers separated by a small air gap must first be understood. This particular configuration is very common in practical telecommunications, namely in fiber optic connectors

(figure 2.2) or splices. Following conventional copper media terminology, permanent connections are referred to as splices, whereas connections designed to be disconnected many times are referred to as connectors. The total effect of a splice in a multi-mode optical fiber system depends on how the connector is excited (input power distribution), how the connector couples light from one fiber to the other (local connector characteristics), and how the connector

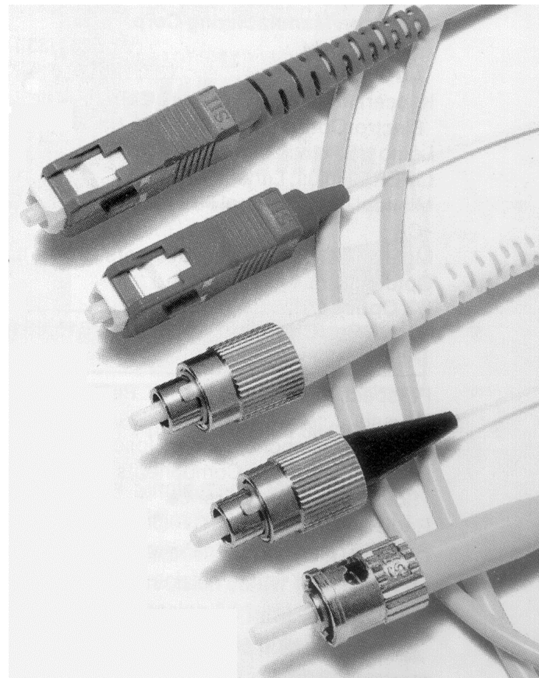

figure 2.2: The picture shows various standard optical fiber connector types. They are plugged or screwed together. These butt-joint connections (both fiber ends are aligned and brought to contact) represent the predominant method for connecting optical fibers (single-mode or multi-mode).

affects the loss of the receiving fiber. Losses in the receiving fiber are extremely difficult to calculate because the various loss and coupling coefficients of the individual modes in a multi-mode fiber are not known. Real fibers are far from ideal. Statistically distributed imperfections like irregular variations in the refractive index profile on the fiber, geometric tolerances due to the production

process, and impurities that cause light scattering, influence the power distribution within the modes all along the fiber. The model for coupling behavior discussed in this chapter is based on fibers that have a core index of refraction profiles of the form shown in (figure 2.3) developed by Gloge and Marcatili [4], where the radially symmetric index of refraction, n, is a power law function of radial position, r.

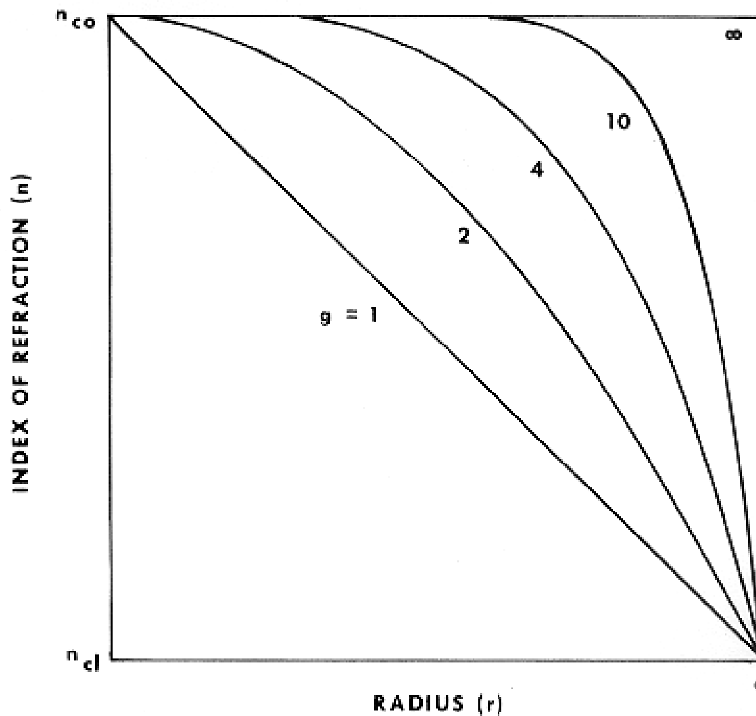

figure 2.3: Index profiles of the form $n=n_{co}[1-2\Delta(r/a)^g]^{1/2}$ for g=1,2,4,10 and ∞. For parabolic fibers g≈2. From Gloge and Marcatili, 1973. Here, n_{co} =maximum index in the core, $\Delta \cong (n_{co}-n_{cl})/n_{co}$, $n_{cl} \cong$index of the cladding, a=fiber core radius, g=index profile parameter

(Figure 2.3) shows the index profile for several values of the profile parameter, g. The most commonly used values of g for multimode fibers are ~2 (parabolic graded-index fibers) and ∞ (step index fibers). The maximum bandwidth for multi-mode fibers results from a g value near 2, and these multi-mode fibers dominate in

telecommunications and other applications requiring modest bandwidth * distance products. An ideal graded index multi-mode fiber is shown in (figure 2.4).

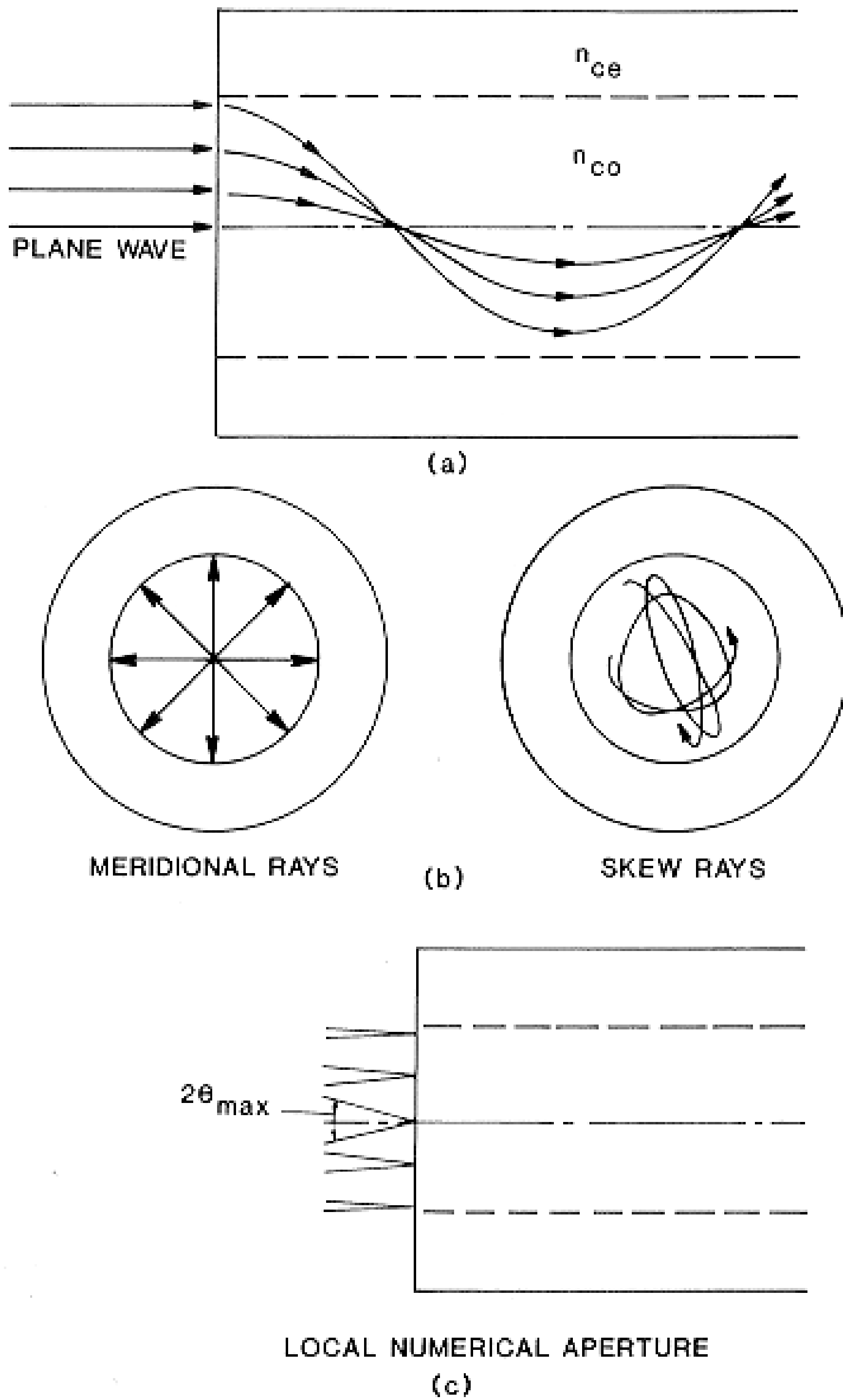

Figure 2.4: Graded index fiber indicating sinusoidal paths for meridional rays and helical paths for skew rays [3]. Acceptance angle varies with radial position on the core. (a) Side view. (b) End view. (c) Acceptance angle (explained in 2.1.3) for various core positions.

Point sources

To simplify and generalize the concepts involved in splice loss modeling for optical fibers from a geometric optics point of view, a point light source is defined. The geometric representation of any given ray of light at some point P(r,ψ) on the face of the fiber core is shown in (fig. 2.5). θ is the angle between the ray and the direction of the fiber optical axis, z, and ϕ is the angle between the projection of the ray on the face of the fiber and a line in the plane of the face perpendicular to the line from the center of the core to the point P.

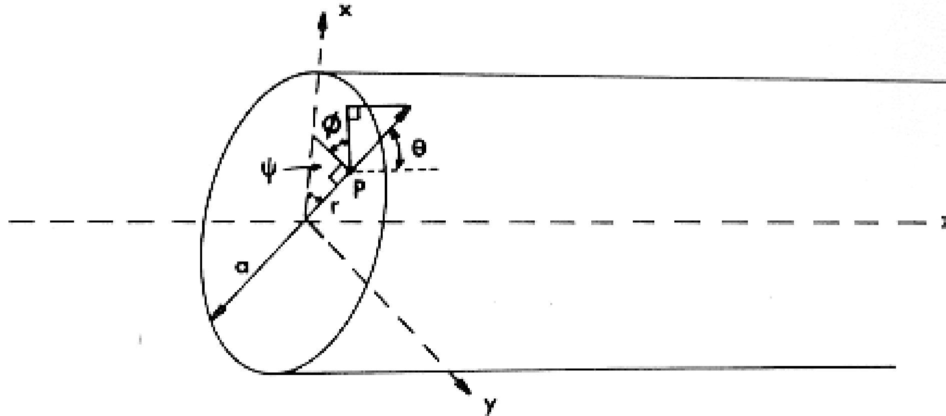

Figure 2.5: Coordinate system for ray at point P(r, ψ) on the face of an optical fiber core.

For a small element of area, dA, at this point, the power launched into the rays with angles θ to θ+dθ and ϕ to ϕ+dϕ is:

(2.1) $dP = I\, dA\, d\Omega$

where $d\Omega$ is the element of solid angle $\sin\theta\ d\theta\ d\phi$ and I is the source intensity function. Fibers with a core index of refraction which obey the equation of figure caption (fig. 2.3) have numerical aperture (NA) given by (equation 2.2).

$$NA(r) \cong n_{co}\sqrt{2\Delta}\left[1-\left(\frac{r}{a}\right)^{g}\right]^{1/2} \quad (2.2)$$

This equation defines the local numerical aperture for any point on the core and clearly has the same shape as the index profile as a function of radius, r. The numerical aperture decreases monotonically from a maximum at the center of the core to zero at the core cladding boundary. The NA gives the acceptance angle for each point on the core, that is, the maximum angle θ with respect to the longitudinal axis of the fiber at which light rays can propagate and still be guided by total internal reflection. Any light entering the fiber at that point on the core at angles greater than θ_a=arc sin [NA(r)] is very rapidly lost through radiation or leaky modes. The model presented assumes that the fiber carrying light into the splice contains all rays at any point on its core within the NA at that point, as discussed. Each point on the core of the transmitting fiber is considered as a point source with light distributed over the acceptance angle at that point.

For a perfect splice between identical, perfectly aligned fibers with perfect ends and no gap, the angle θ does not change across the interface between the two fiber end faces. For non-identical or misaligned fibers, the acceptance angle at the corresponding, contiguous point on the face of the receiving fiber core determines what fraction of the light from the point source is launched into propagating modes in the receiving fiber, and how much is lost locally at the splice (radiation modes)

or within a few meters of it (leaky modes). If the NA of the receiving fiber is equal to or greater than that of the transmitting fiber at a given point on the core, all light incident from the transmitting fiber at that fiber is assumed to be received and the point transmission is 100% for index-matched splices. For splices with an air gap, the reflection losses must be taken into account. However, if the NA of the receiving fiber at that point is less than that of the transmitting fiber, the rays at angles greater than θ_a cannot propagate in the receiving fiber and are lost through radiation or leaky modes. The light lost is proportional to the ratio of the NA's squared [5]. To calculate splice loss using point transmission, it is also necessary to know both the amount of power propagating in the transmitting fiber at each radial point of the core and how it is angularly distributed. If this is known, then the fractional splice loss is simply the sum of integral of the product of the point transmission ratios and the point power distribution over the receiving fiber core divided by the total power in the transmitting fiber.

Optical power distribution over the fiber core surface

The angular distribution of the power is a function of both the modal power distribution in the fiber and the shape of the core index of refraction. In step index ($g=\infty$) fibers, each mode is uniquely represented by the angle of propagation in the core. The angular power distribution at any point is therefore directly related to the modal power distribution. Since no unique ray angle is associated with each mode in a graded-index fiber, the angular power distribution is not directly related to the modal power distribution.

Gloge and Marcatili [4](1973) showed that if all modes of a multi-mode fiber are equally excited, the power distribution across any local numerical aperture at any point on the core is uniform and the overall power distribution exiting the end of

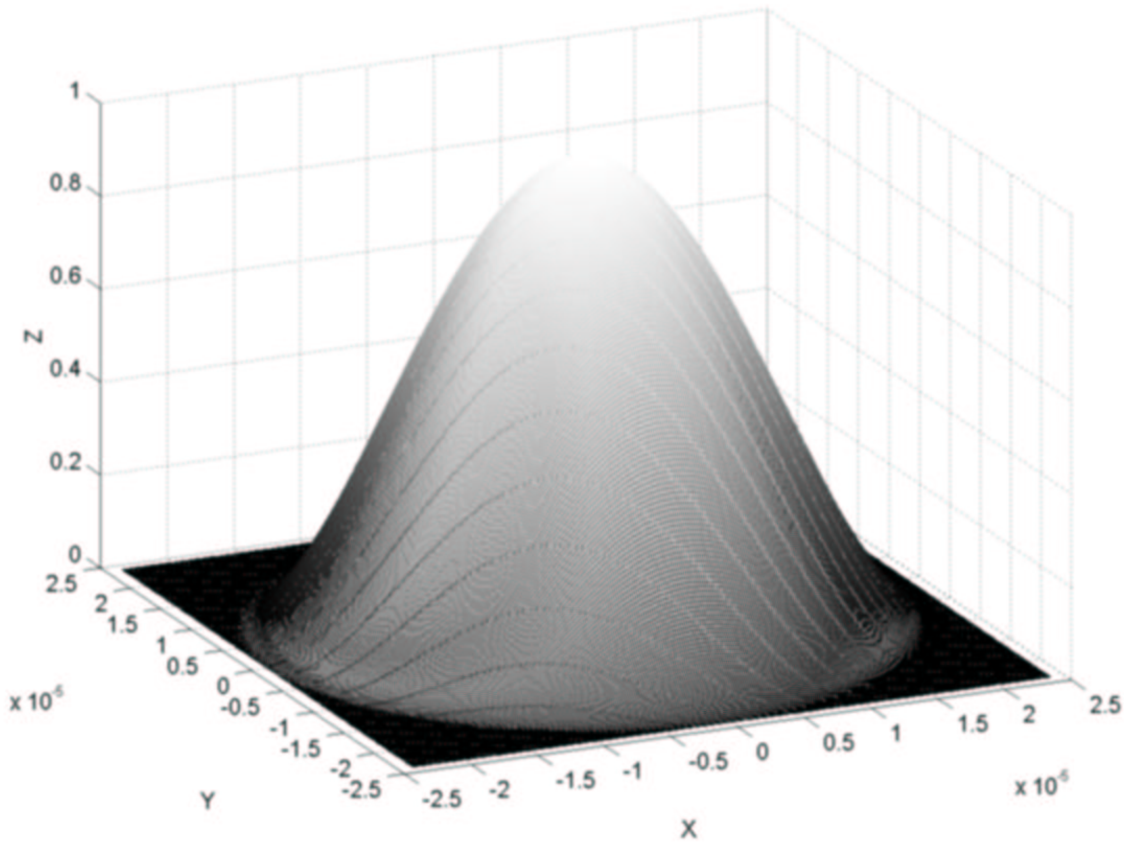

Figure 2.6: Calculated normalized power distribution of a graded index (parabolic) multimode fiber of 50μm.

the fiber has the shape of the index profile for profile parameters, g, between 2 and ∞ (fig. 2.3). Several authors have assumed this power distribution as the basis for calculating splice loss [6,7,8,9]. Using this model, Miller [7] calculated the splice loss caused by transverse offsets (fig. 2.8) for both identical and diameter mismatched fibers and showed that these uniform power model calculations for identical parabolic fibers were inaccurate. The discrepancies between calculated

and measured splice losses using the uniform power model led to the development of the Gaussian power distribution model [5,10] which was able to predict splice losses more accurately. The main interest of the work referred to was to predict connector and splice losses in telecommunication systems where a fiber line can have up to twenty connectors.

Intrinsic and extrinsic splice loss parameters

The major factors affecting multi-mode coupling loss are usually divided into two categories. These are intrinsic parameters, differences in the properties of the fiber being connected, and extrinsic parameters, the alignment and quality of the splice. The principle intrinsic parameters (fig.2.7) are core radius (a), normalized index difference (Δ) (figure caption 2.3), index parameter (g) (figure 2.3), core offset (ε), core eccentricity, and core ellipticity. Extrinsic parameters include transverse (lateral) offset, longitudinal offset (end separation), angular misalignment (tilt) (figure 2.8) and end quality (figure 2.9).

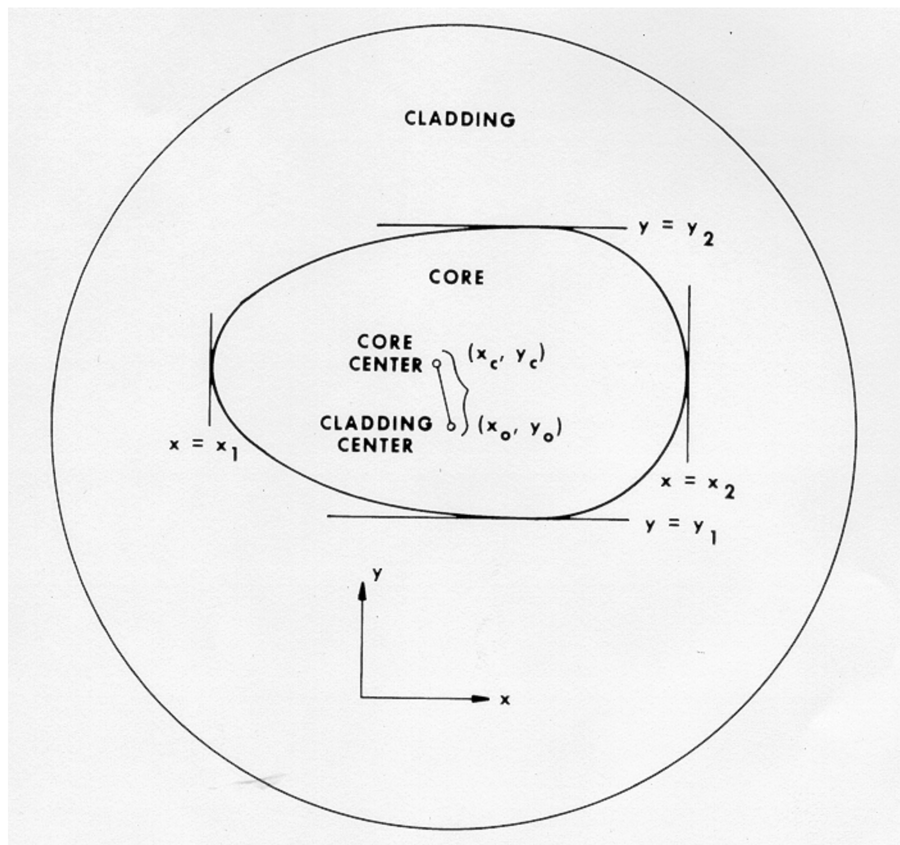

Figure 2.7: Mathematical definitions of core parameters-core diameter, ellipticity and eccentricity. Long diameter $d_L=(x_2-x_1)$; short diameter $d_s=(y_2-y_1)$; Core ellipticity = $2(d_L-d_S)/(d_L+d_S)$; Core offset =$\varepsilon= [(x_c-x_o)^2+(y_c-y_o)^2]^{0.5}$. Core eccentricity = $2\varepsilon/(d_L+ d_S)$. From [3].

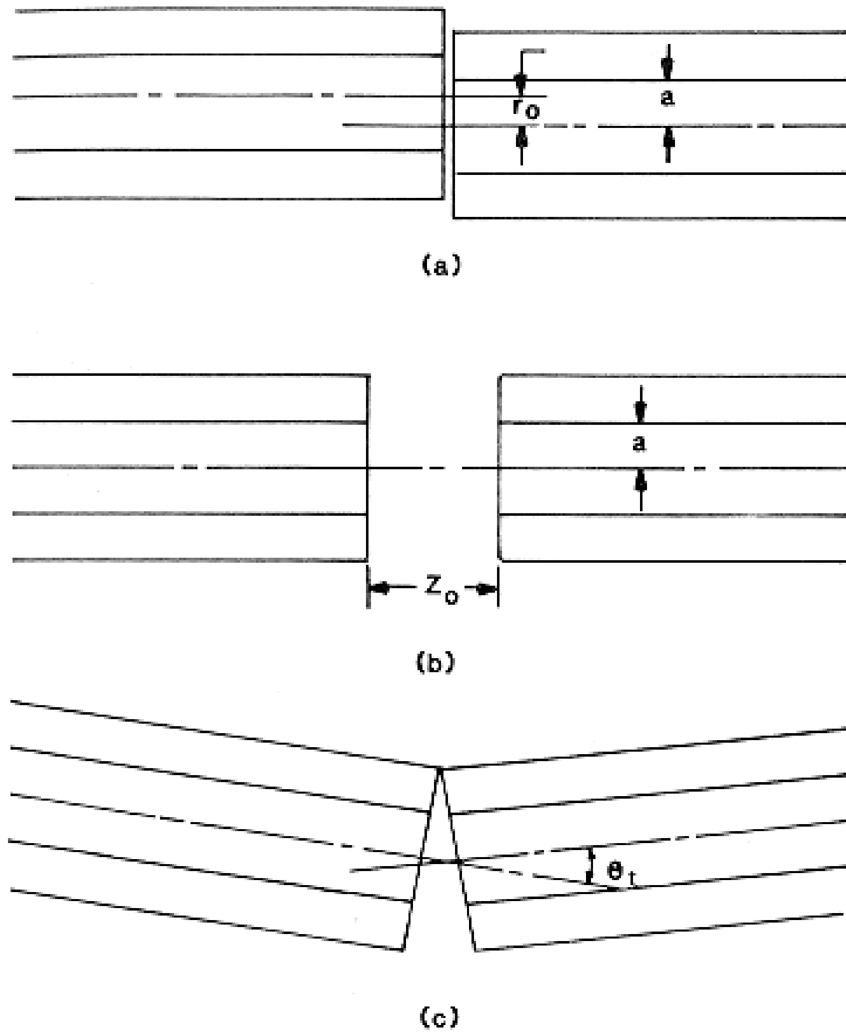

Figure 2.8: Alignment errors using optical fibers. (a) Transversal offset. (b) End separation or longitudinal offset. (c) Angular misalignment. From [3].

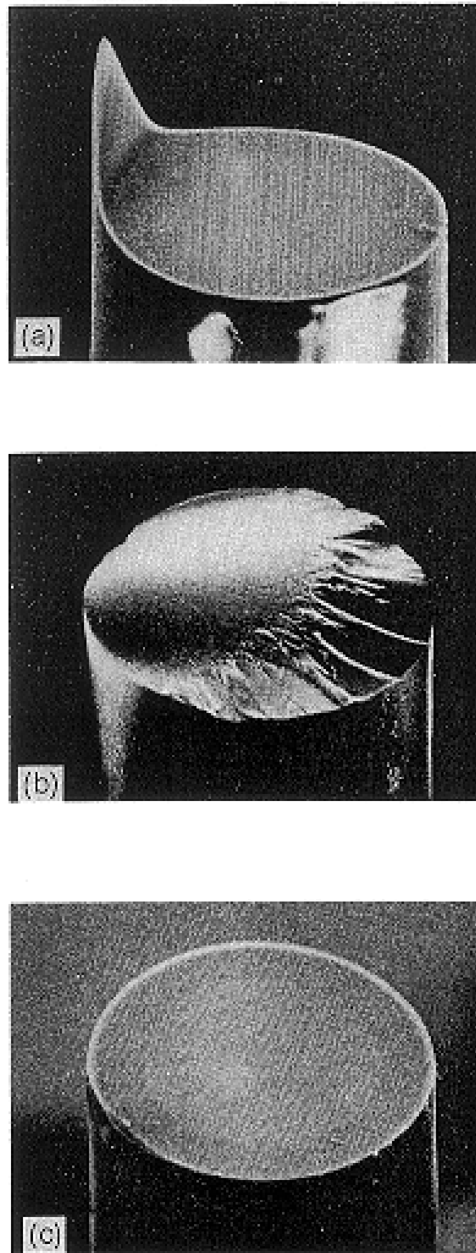

Figure 2.9: Fiber end quality. (a) lip. (b) mist and hackle. (c) An ideal fiber end. From [4]

2.1.1. Numerical calculation of multimode fiber coupling with shutter

Modeling

In the previous section the coupling behavior between two multi-mode was discussed. Introducing a thin shutter in the air gap between two self-aligned multi-mode optical fibers adds one more extrinsic loss factor into the fiber system (fig. 2.1). To analyze the effect of the shutter in a simple way, two perfectly aligned fibers with perfect ends and no gap are assumed. The air gap present in reality is neglected in this analysis since experimental loss versus longitudinal offset measurements [3] showed a very small magnitude compared to transversal offset. The position of the shutter (fig. 2.10) can vary between non blocking (open) and totally blocking (closed) states.

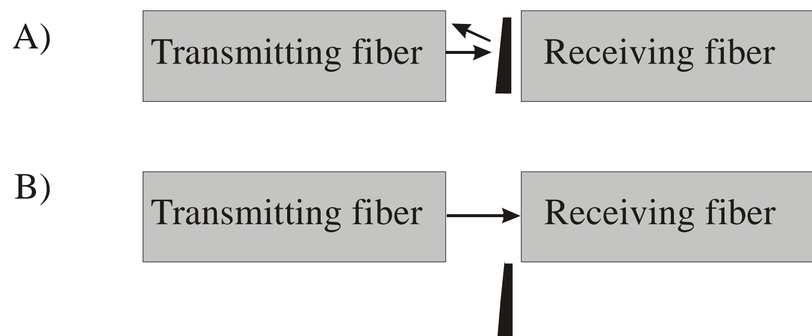

Figure 2.10: Extreme shutter positions for a test structure: (A) completely closed (blocking); (B) completely open.

Later in this work it will be shown that the most interesting position for sensing applications is where half of the light is coupled into the output fiber. To model the effect of the shutter, different shutter positions are now discussed:

1) In the case where the shutter is completely open, the same approach as for ideal fiber connectors is used. This means that the acceptance angle

of the receiving fiber is the same as the transmitting one. Again, it is assumed that both fibers are identical and perfectly aligned.

2) As soon as the shutter takes a position where a part of the light beam emitted from the transmitting fiber is affected, the coupled power can be modified. This is obvious in the case where the shutter blocks a coupled part of the beam. But also non-coupled light beams can suddenly be coupled into the receiving fiber due to scattering or reflection on the edge of the shutter. It is assumed however that this reflected or scattered light has a negligible power contribution to the overall power coupled, since in reality the shutter has a thin edge surface (fig. 2.17). The point sources distributed over the whole fiber core surface are pointing either onto the receiving fiber core or on to the shutter. Since ideal alignment and identical fibers are assumed the point sources facing the fiber are completely coupled to the receiving fiber. The point sources facing the shutter surface however are not transmitted.

3) When the shutter covers the whole core surface of either the transmitting or the receiving fiber no light is transmitted any more and the shutter is considered to be in the closed position.

Diffraction effects on individual modes are ignored in this analysis. There are two reasons for this: (1), the geometric optic based model has proven to be accurate also for high transversal offsets [13], and (2), the use of a white light source in this work averages eventual diffraction effects so that they are difficult to observe.

Most 50 µm graded index multi-mode fibers are specified as having fiber diameter tolerances of ±2µm for the cladding and ±3µm for the core. It is assumed that the core centers of these fibers will have in most cases a transversal offset varying from 0 to 3 µm when they are inserted in microfabricated self aligning grooves. Angular offset between the fibers is neglected since micromachined fiber grooves are used. As soon as a transversal offset is included into the shutter modulation model the power distribution over the solid angle of the individual point sources must be defined. In the previous section two models are presented, the uniform and the Gaussian distributions. These models have been developed to calculate connector and splice losses especially due to angular or transversal fiber mismatch. The Gaussian distribution model was shown to be more accurate for this type of mismatches.

In reality, when the fibers are aligned in micromachined fiber grooves the transversal core-offsets are not known. To compare measured with modeled values the assumption of perfect alignment is therefore the simplest choice. In the case of perfect alignment the uniform distribution model is accurate. For this reason as well as for the fact that the uniform model is simpler and faster to calculate the uniform model is implemented. In the present work the goal of modeling a small amount of transversal offset is to roughly quantify this effect in the presence of a shutter.

Modeling results

The effect of transversal fiber offset on the power distributions coupled into the receiving fiber is shown in (figure 2.11). Calculated transmission ratio versus shutter displacement are shown in (figure 2.12) for ideal alignment and for transversal offsets. Core diameter mismatch simulations are shown in (figure 2.13).

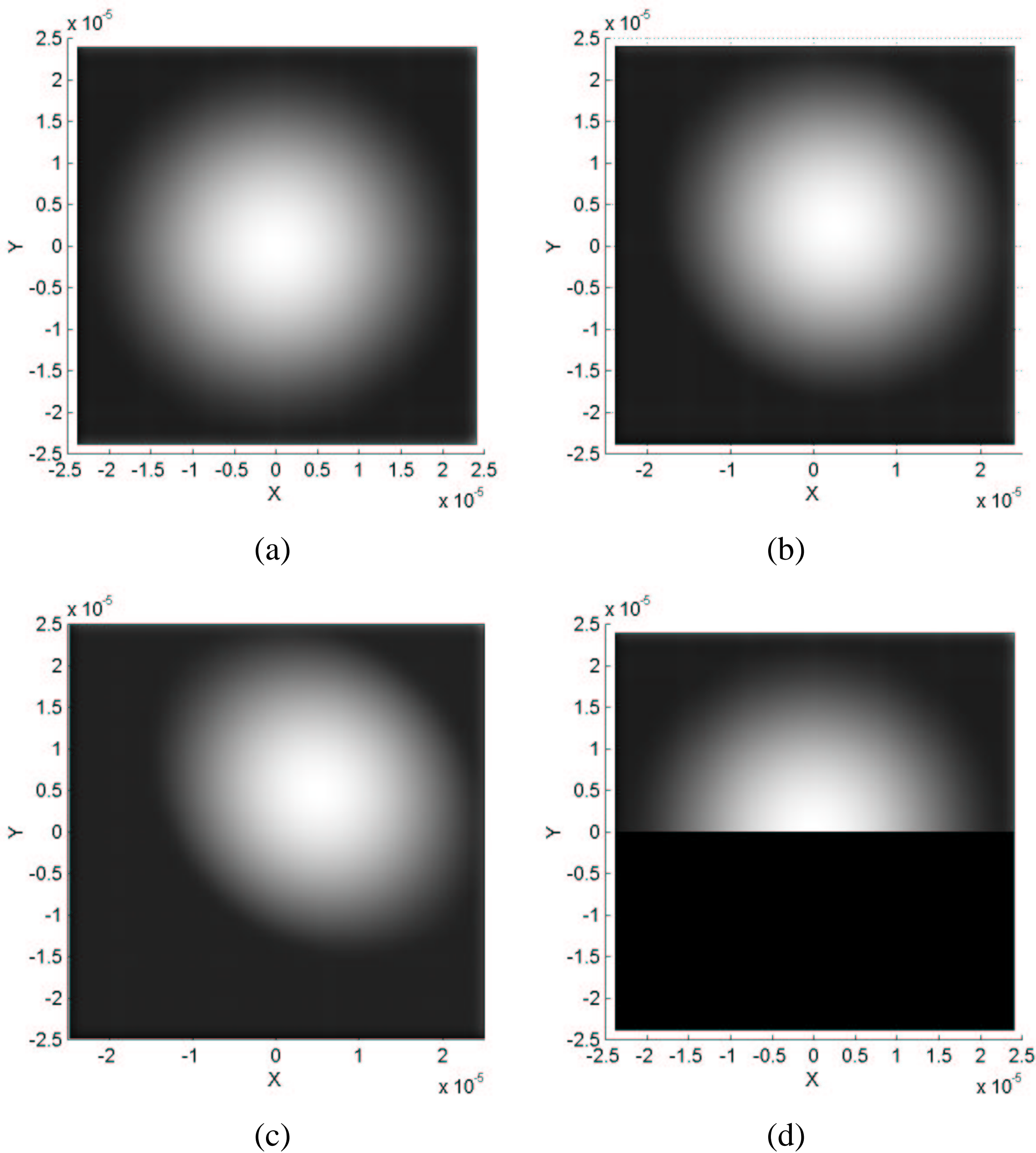

Figure 2.11: Modeled power distribution coupled into the receiving fiber of parabolic index multimode fibers with 50 μm diameter. The core center of the transmitting fiber is at the origin. (a) Receiving fiber core center at the origin, ideal alignment. (b) Receiving fiber core center offset (x/y: 5μm/5μm),calculated with uniform power distribution model. (c) Receiving fiber core center offset (x/y: 10μm/10μm), calculated with uniform power distribution model. Highest intensity point (bright) shifts due to transversal offset. Shifting is less than half of the core offset values. (d) Shutter edge at the origin of ideally aligned fibers.

Previous pictures show the deformation of the coupled power distribution due to transversal offset. As a shutter moves down along the y-axis an increasing part of the light power is coupled. The response to this shutter movement is shown in (figure 2.12). The half power point (transmission ratio = 0.5) shifts in direction of the transversal offset of the receiving fiber compared to the transmitting one. However the magnitude of the shift is around a half of the effective offset value. For a displacement sensing application the important parameters of the transmission rate curve are the linear range and the slope. Table 2.1 shows these characteristics for an ideal fiber alignment and for transversal offsets.

Models:	Ideal alignment	Transversal X/Y Offset of 2.5/2.5 [μm]	Transversal X/Y offset of 5/5 [μm]
Linear range limits seen from the origin	-5/+5 [μm]	-5/+3.5 [μm]	-5/+2.5 [μm]
Slope [μm^{-1}]	0.0401	0.0412	0.042
Slope change relative to ideal model	0%	2.7%	4.7%

Table 2.1: characteristics of the modeled transmission rate versus shutter position shown in figure 2.8.

The model shows a slope change below 5% between an ideally aligned fibers and fibers with an important transversal offset. The linear range and its center are clearly affected by a transversal offset.

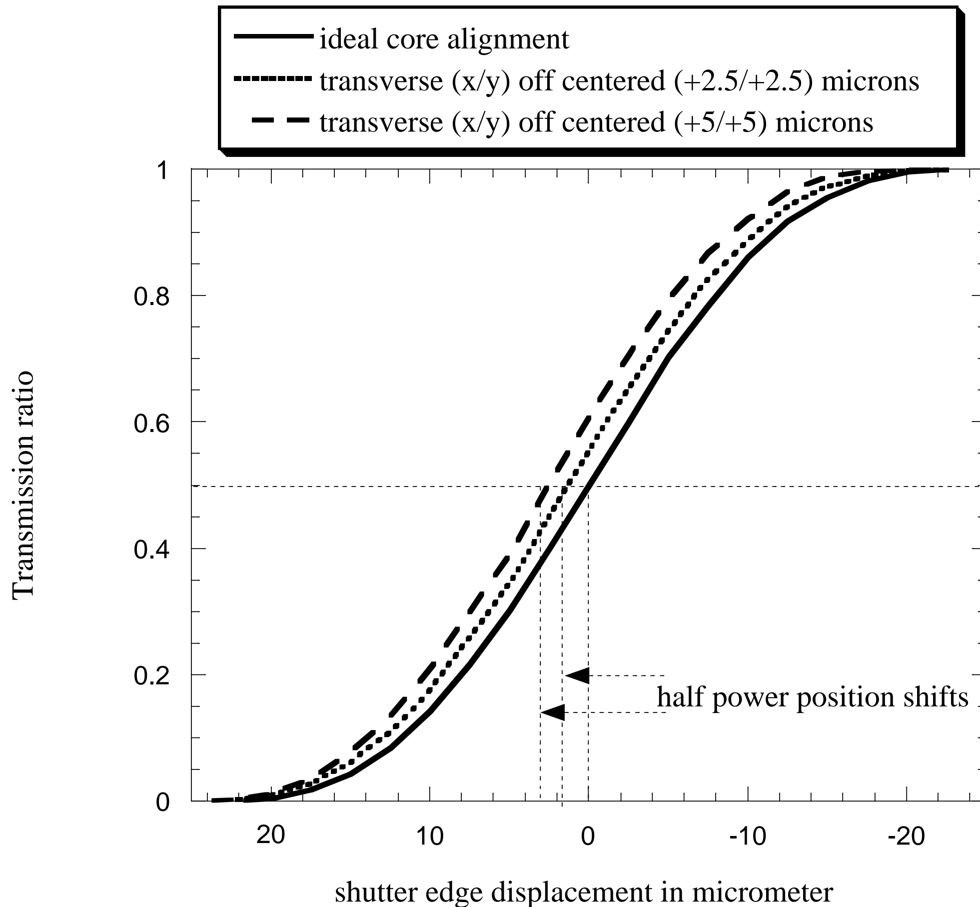

Figure 2.12: Simulated transmission ratio from transmitting fiber to receiving fiber. A maximum transmission rate of 1 corresponds to the shutter being completely open. Simulations are done for the ideal case and two different transversal x/y core center offsets. The core center of the transmitting fiber is at the origin. Half power position (transmission rate=0.5) shifts due to the transversal offset. It appears that shifting is around half of the core offset values. Transversal offset effects are calculated with the uniform power distribution model.

A pure diameter mismatch shows only very little effect on the transmission ratio in function of the shutter position (figure 2.13). Figure 2.14 compares the multi-mode transmission rate of a parabolic index fiber to a step index fiber.

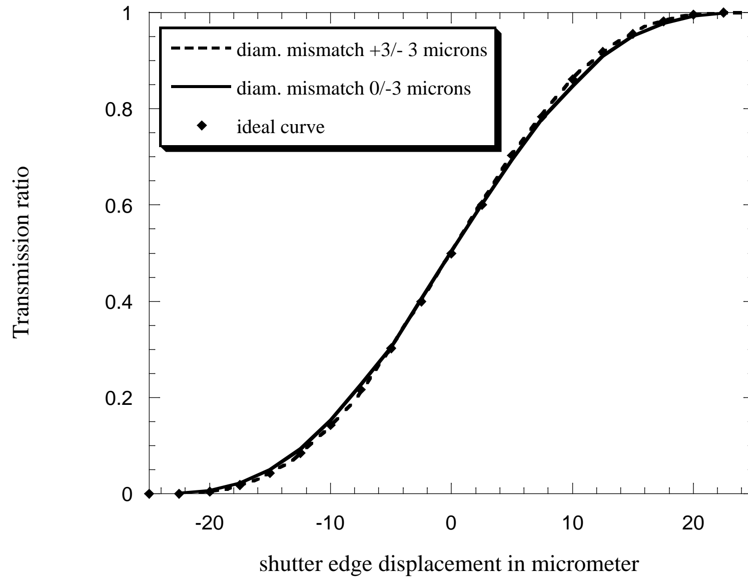

Figure 2.13: Simulated transmission ratio from transmitting fiber to receiving fiber. Maximum transmission ratio corresponds to the shutter in the open state. Simulations are done for the ideal case and two core diameter mismatches.

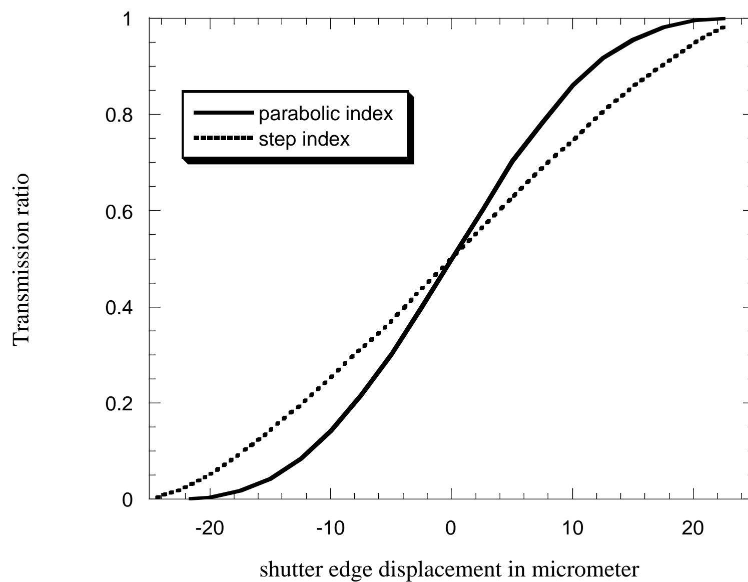

Figure 2.14: Transmission ratio versus shutter displacement for parabolic and step index multimode fibers.

2.2. Microfabrication of a test structure for shutter modulation

To test shutter modulation with multi-mode optical fibers, a shutter displacement of at least the fiber diameter is required, so that the fiber-shutter arrangement can completely block or transmit the light beam in the air gap (fig 2.12). The distance between the two fibers should be as small as possible in order to avoid unnecessary loss provide the conditions where multi-mode coupling theory is simple. This limits the space available for the shutter. A thin shutter is therefore the ideal solution.

2.2.1 Design considerations

In order to measure transmission ratio from the transmitting fiber to the receiving fiber as a function of the shutter position a moving shutter is required. The easiest solution seems to be a shutter attached to the end of a cantilever beam. An external force could bend the cantilever beam up to the desired shutter position. In practice it is more convenient to apply a vertical force with the help of gravity than a horizontal one. Displacement measurements in the order of a micrometer or less are easier to perform in the vertical direction, too. Therefore a test structure based on a vertically moving cantilever beam is preferred (fig. 2.15).

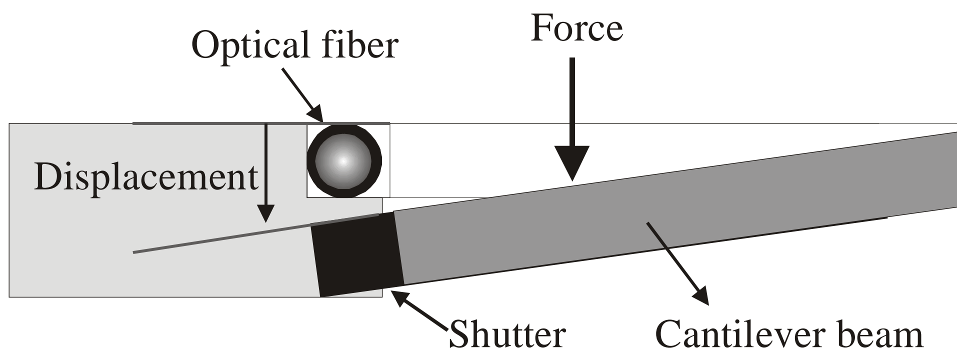

Figure 2.15: Test structure with vertically moving cantilever beam. Optical fibers are self aligned in a fiber groove.

Using silicon DRIE technique for fabrication, two different silicon substrate materials can be used, the classical silicon wafer and the silicon-on-insulator (SOI) wafer. SOI-wafers have a buried oxide layer in between two silicon layers. The buried oxide layer serves as an etch stop for the DRIE. However, these wafers are clearly more expensive than the silicon wafers. Therefore, a structure like that shown in (fig. 2.15) was first fabricated using conventional silicon wafers.

2.2.2 Fabrication process

The fabrication process is illustrated in (figure 2.16). It consist of initially micro machining the front surface of a silicon 390 µm wafer followed by the micro machining of the back surface. Etching of the front surface forms 87µm deep grooves for the optical fibers as well as cantilever and shutter structure. Etching 303 µm of the back surface releases the cantilever beam and shutter. In the process shown in (figure 2.16 (a)), first a silicon dioxide layer of 500 nm is thermally grown on the silicon wafer. A photolithography process (table2.2) is performed on the front side followed by a buffered HF bath to remove the oxide layer and so pattern the mask (figure 2.8(b)). Then the photoresist is stripped in an acetone bath and the wafer cleaned in isopropanol. Finally the deep reactive plasma etching is performed (c). Deep reactive ion beam etching rate is not uniform over the whole wafer surface and depends also on local feature width size and shape. Experience shows that the desired structure depth is etched locally while at other locations of the structure or wafer the structures do not have the required depth. At the locations where the etch rate is higher the plasma continues to etch either silicon or an etch stop layer. If a DRIE process from the back side of the wafer breaks through to the

Table 2.2: Photolithography processes used for test structure fabrication. Developer was buffered with 3 or 4 parts of de-ionized water. Before the wafers were spin-coated with resist they were placed in a 200℃ oven 30 minutes to remove water molecules from their surface. They were then primed with a gaseous hexamethyldisilazane for 10 min. to passivate remaining silane groups and improve adhesion of the photoresist layer.

Step	Photo-resist	Thickness	Spinning 1. ramp	Spinning 2. ramp	Prebake T=100°C	Develop-ment	Postbake
Front	AZ 1518	1.8 µm	5s 500 rpm	40s 3000 rpm	Hotplate 1 min	AZ B 351 1:3, 1 min	30 min 120°C
Back	AZ 4562	10 µm	3s 700 rpm	30s 1700 rpm	Hotplate 2 min	AZ B 401 1:4, 1 min	75 min 85°C

front side, there is a significant chance that previously formed front side structures will be damaged. This also can happen if SOI wafers are used. The buried oxide layers in this case form thin membranes which may be stressed enough to break after a certain etch time. However, the buried oxide layer is generally a good protective layer if etch process are properly controlled. The present structure requires a DRIE process also on the back side. The following steps are performed to protect the etched front side of the wafer while the back side is etched. A new layer of silicon oxide of 300 nm is grown thermally (fig. 2.16(d)). It serves at the same time as additional mask to the photo-resist and as etch stop for front structure protection. Then a 100 nm thick silicon nitride layer is deposited on the oxide layer (fig. 2.16(d)). It serves as protection layer to the front oxide layer during a later buffered HF bath. The back silicon nitride layer is then removed by reactive ion etching (RIE) (fig. 2.16(e)). A back-side photolithography (table 2.2) with 10 µm thick photo resist is performed as next step followed by a buffered HF bath to remove the silicon dioxide (fig. 2.16(f)). Prior to deep plasma etching the front side of the wafer is glued with photo-resist on a silicon wafer in order to protect the

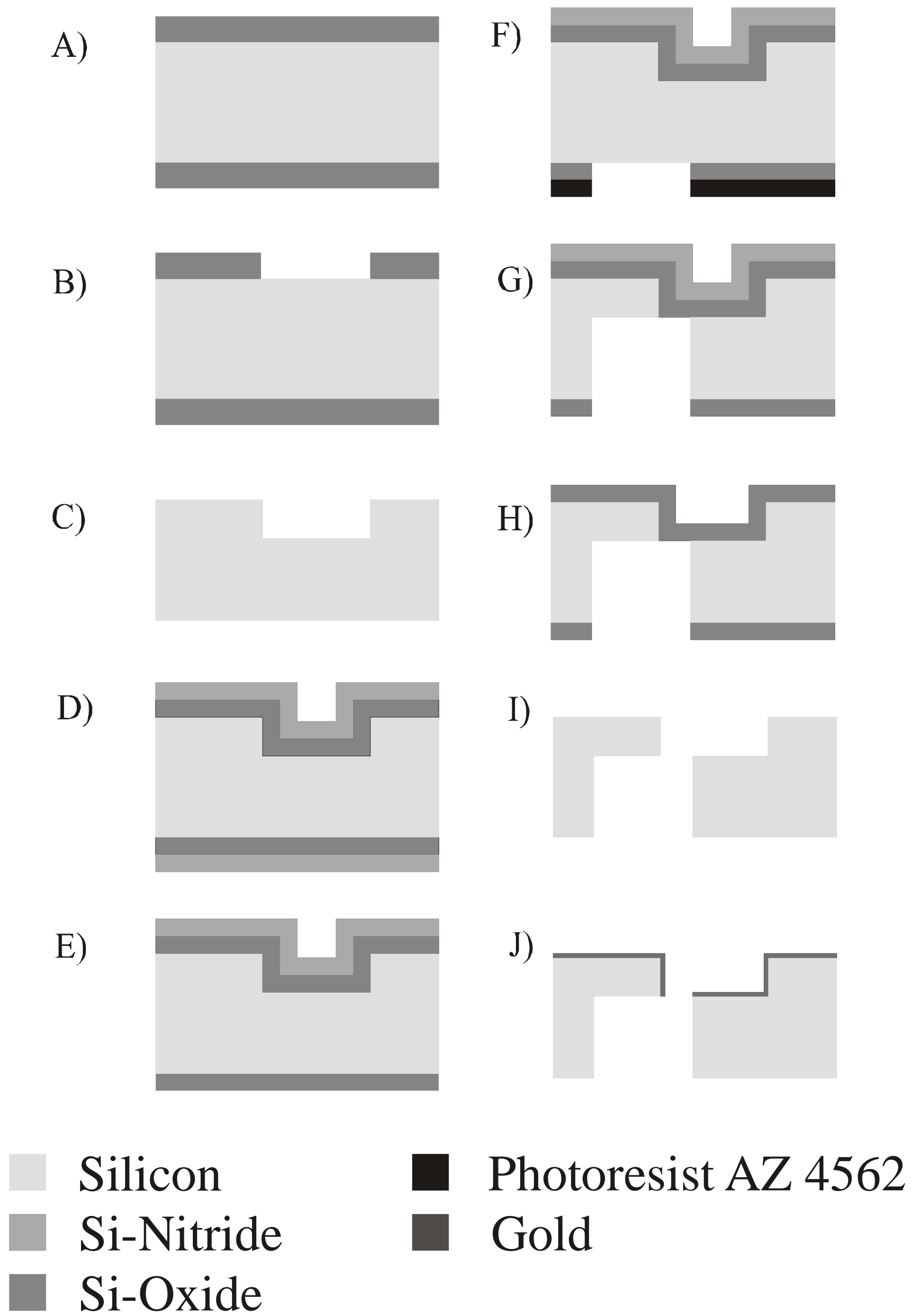

Figure 2.16: Fabrication process of test structures with a silicon wafer

aluminium chuck from a direct plasma exposure. This would occur if the silicon dioxide protective layer were to break during back side etching. After etching (fig.

2.16(g)) the wafers are left over night in an acetone bath so that the structured wafer can be separated from the protection wafer and rinsed. The silicon nitride layer on the front side is removed with RIE (fig. 2.16(h)) as well as the remaining oxide (fig. 2.16(i)). A 10 nm buffer layer of titanium is then deposited on the front side followed by a gold layer of 200 nm, both layers formed by electron beam evaporation technique (fig. 2.16(j)). After dicing the wafer, the sensing structures are glued onto a substrate so that they can easily be handled. The optical fibers are fixed with UV-glue. The sensing part of the structure is shown in (figure 2.17). Test structures with three different transmitting fiber-to-shutter distances are fabricated. The receiving fibers were always glued at the same distance from the shutter.

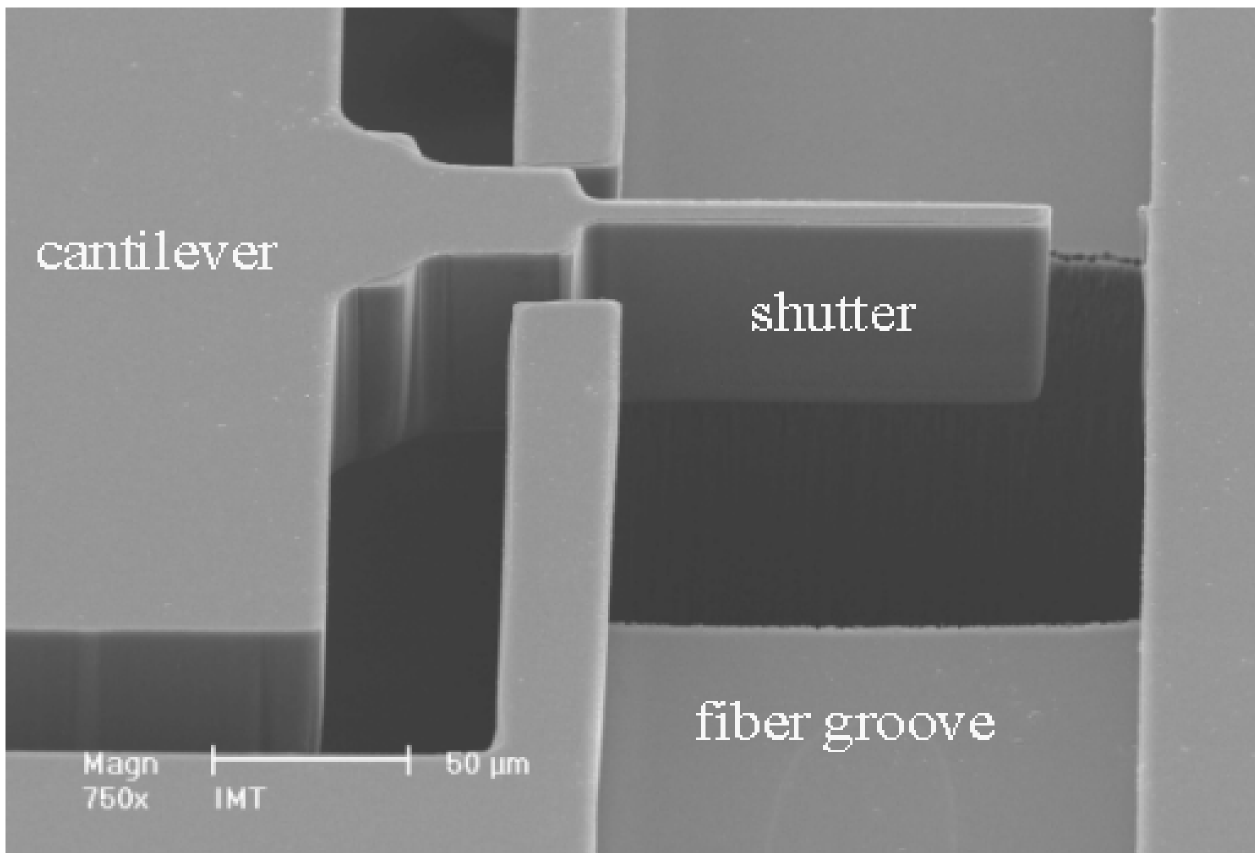

Figure 2.17: End part of the cantilever with shutter and fiber grooves

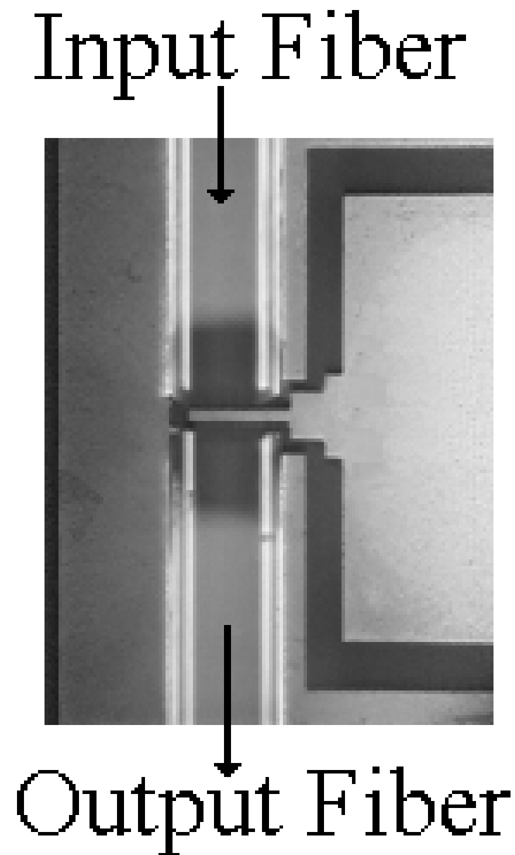

Figure 2.18: Top view of test structure with input (transmitting) and output (receiving) fibers glued in place.

2.3. Characterization of the test structure for shutter modulation

2.3.1. Experimental set-up and measurements

The goal of fabricating the test structures was to characterize the coupling efficiency from the transmitting fiber to the receiving fiber as a function of the

shutter position. The components and set-up used to determine this dependence is shown in (figure 2.19).

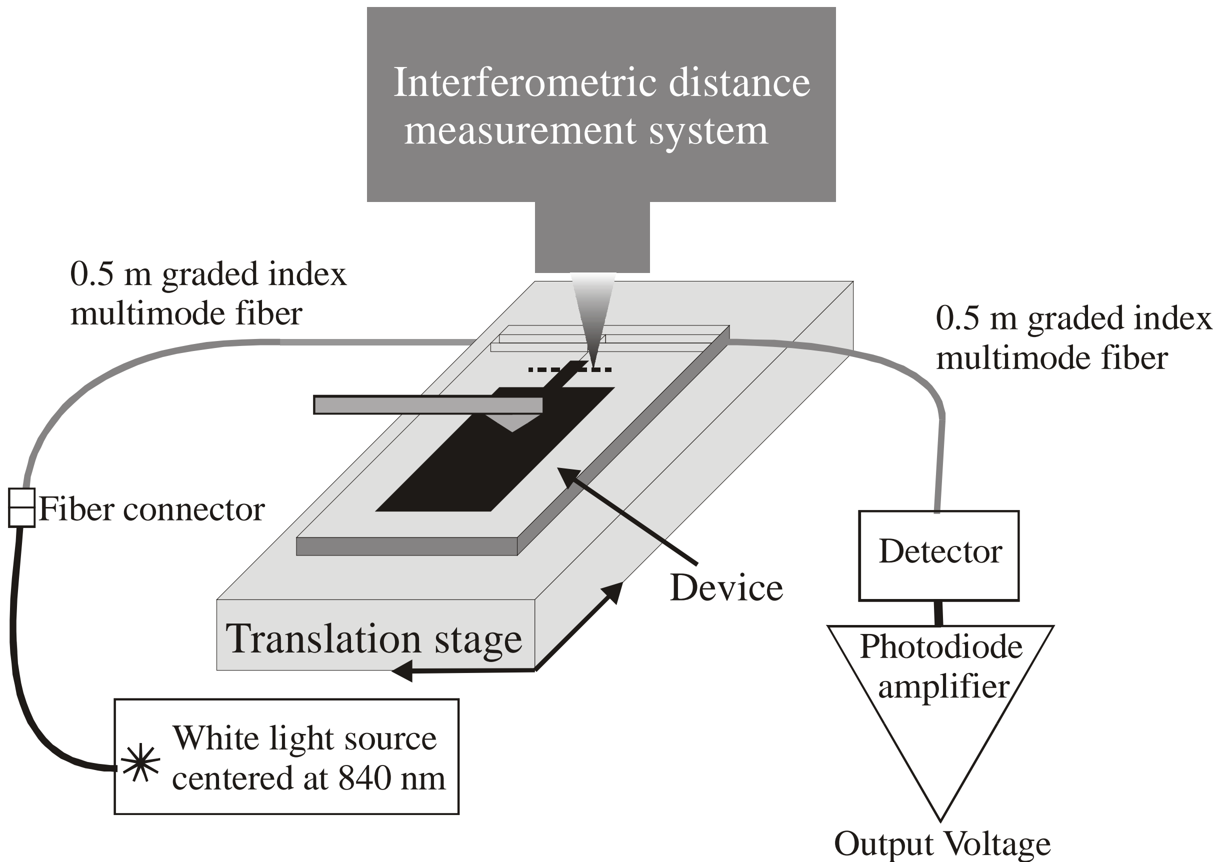

Figure 2.19: Experimental set-up for transmission ratio versus shutter position measurement

The first characterization was performed using a super luminescent diode (SLD). Such a diode source has a wide spectral width of around 40 nm. This results in a drastically reduced coherence length of 30 μm compared to a common laser diode with a coherence length of several meters and more. The SLD has a similarly large spectral width as a light emitting diode (LED). However, an SLD can inject much more light power into an optical fiber than an LED. It therefore offers greater experimental flexibility. The SLD used in this experiment was packaged with a single mode polarization-maintaining fiber. This fiber was connected to the 0.5m

long multimode optical fiber of the test structure. The test structure was fixed on the translation stage of an interferometric distance measurement system. A force spring mount was also fixed onto the translation stage. The receiving fiber was connected to a detector mount. The photo current of the detector was amplified by a photodiode amplifier. The signal could be read on a volt-meter. For each position of the shutter the interferometric measurement system scanned the surface of the test structure and measured the surface profile. The scan path crossed a part of the silicon frame (reference) and a part of the cantilever beam close to the shutter. The shutter position was then known relative to the fixed surface of the test structure. The obtained measurement curve is shown in figure 2.11. Table 2.3 shows the results for each test structure with a SLD as light source.

Table 2.3: Test structure characteristics. Received light power on the photo-detector is 100 μW.

Transmitting fiber-shutter/ Shutter - receiving fiber distance [μm],± μm	Linear range [μm], (linearity better than 2%)	Displacement sensitivity [μW/μm] in the linear range
a) 5/5	6.18	8.4
b) 12/5	6.87	7.4
c) 17/5	8.82	6.17

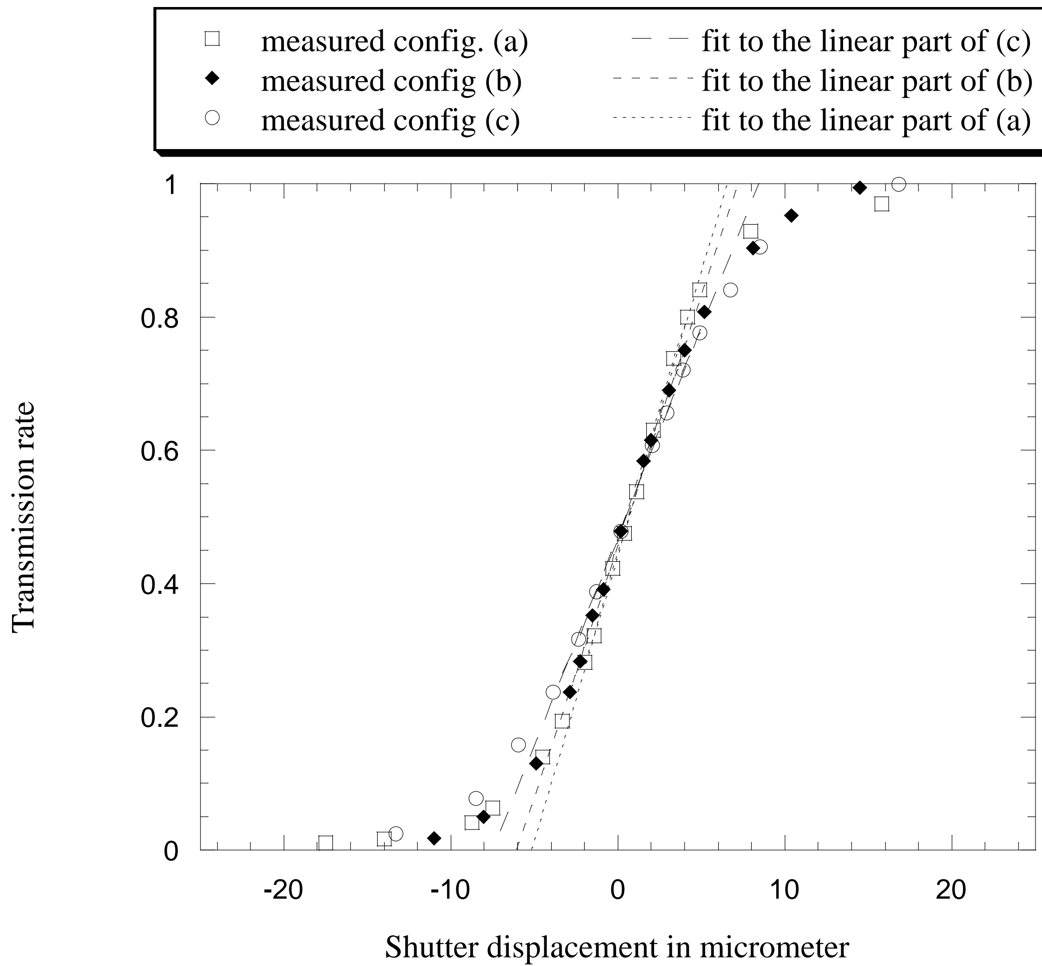

Figure 2.20: Measured transmission ratio for three different transmitting fiber-to-shutter distances: (a) 5 µm, (b) 12 µm and (c) 17 µm. For clarity the measured curves are plotted with the transmission ratio point = 0.5 at the shutter position origin. The dashed curves are the fits of the linear portions of the curves measured for the three different fiber-to-shutter distances.

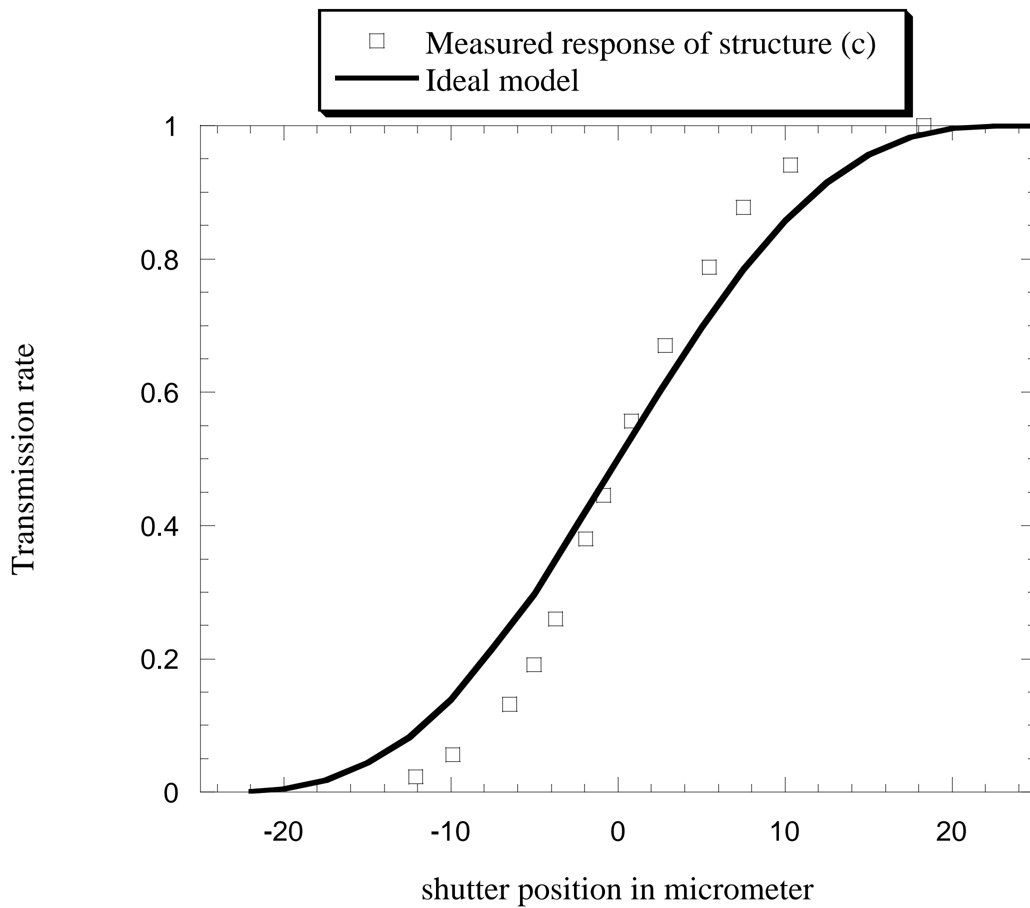

Figure 2.21: Comparison between measurement curve obtained with test structure (c) (see figure 2.11) and the ideal model curve.

Discussion

Table 2.3 shows that the distance between the transmitting fiber and shutter has only an influence on linear range and displacement sensitivity. However from a sensor user point of view these linear ranges are all acceptable. The assumption of negligible air gap thickness made for modeling seems acceptable for gap thicknesses up to 30 µm. (Figure 2.12) shows however a clear discrepancy between the measured curve and the ideal model curve. The measured curves indicate a

clearly higher power concentration in the center of the core compared to the model. The theories about multimode optical fibers [11] have generally been introduced for very long fibers, as they are in telecommunication. Experiments on splice loss versus transverse offset [12] showed different measurement curves for a LED and laser diode source on a 1 km long fiber. Multimode fibers applied in sensors, in contrast, are most often of shorter length. In the present work the SLD source is packaged with a single mode fiber having a core diameter of 9 µm and a numerical aperture of 0.13. This fiber is connected to a 0.5 m graded index multi mode fiber having a diameter of 50µm. The numerical aperture of the launching fiber (NA=0.13) is clearly smaller than the numerical aperture of the receiving fiber (NA=0.2). This particular fiber connection situation (receiving fiber is underfilled) with a receiving fiber length of one meter has been used in splice loss experiments [13]. The conclusions drawn from this experiment was that an under-filled launching excites only modes which propagate near of the fiber core. This explains the experimental curve behavior shown in figure 2.21.

2.3.2. Measurements and results with a LED source

In the first experimental part the test structure measurements were done using a super luminescent diode source. The power distribution in a short multi-mode fiber depends strongly on the light source employed. To have a more general experimental idea of the transmission ratio versus shutter position the same measurements were performed again but with an LED light source (fig. 2.13). An LED at 840 nm central wavelength was connected to a graded index multi-mode fiber one meter in length. Again a fiber connector linked the source fiber to the test structure fiber. In contrast to an SLD source the LED emits light within a high solid

angle. The probability that the modes far from the core center are also excited is therefore higher. The transmission ratio versus shutter displacement curve was therefore expected to correspond more to the theoretical value (figure 2.21). During the experiment the highest light power seen by the detector was 10 μW.

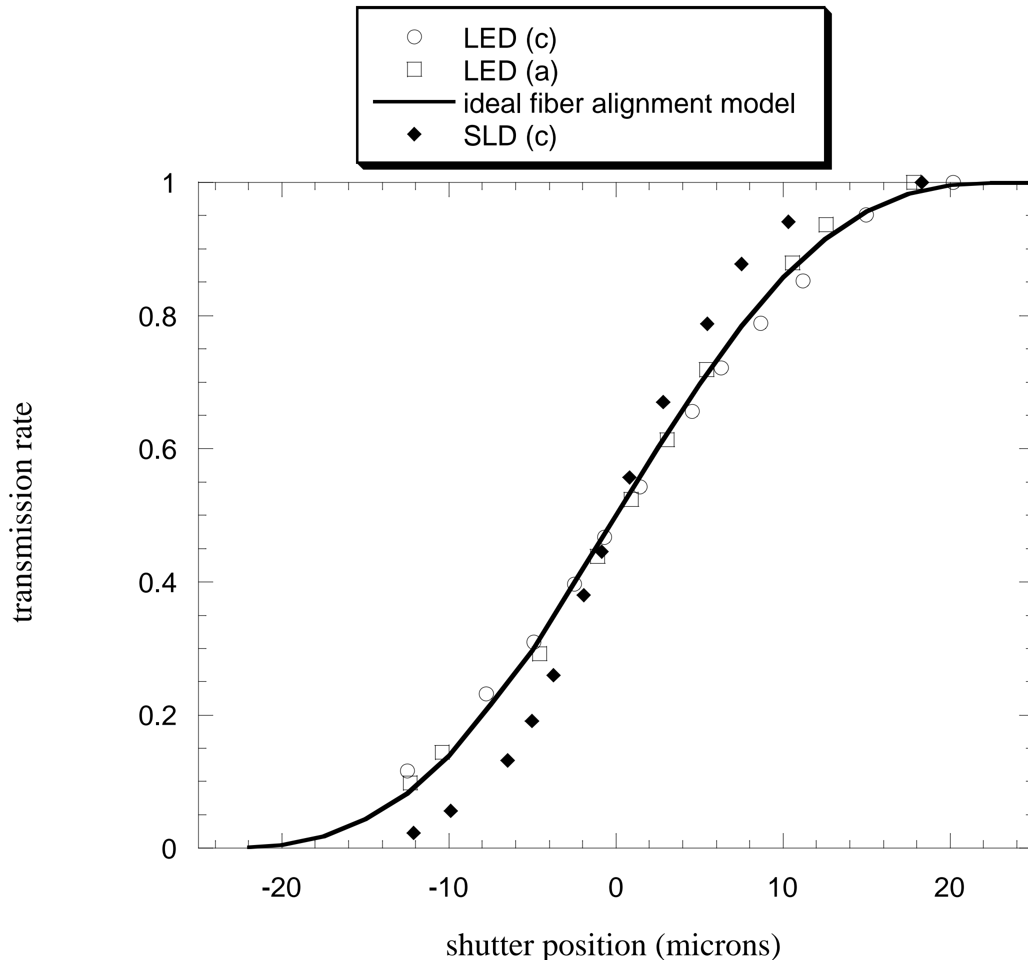

Figure 2.20: Comparison of experimental and calculated results. Measurements with LED source were performed on test structures (a) and (c) (see table 2.3). Measurements with the SLD source were performed on test structure (c). Calculated curve corresponds to the model with perfect alignment.

Figure 2.20 shows that the transmission ratio versus shutter displacement measurement with an LED source agrees well with the calculated values. The different longitudinal offsets (table 2.4) have from the user point of view only a small impact on the transmission ratio response. The measured slope values are close to the slope value for the ideal fiber alignment model.

	LED (a)	LED (c)	model
Linear range [µm]	8.1	8.9	10
Slope [μm^{-1}]	0.042	0.037	0.04

Table 2.4: Measured transmission ratio versus shutter position characteristics. Linear range is determined with a linearity better than 2%. The model assumes ideal fiber alignment.

Conclusions:

In this chapter, the theoretical basis for micro optical shutter modulation with multimode optical fibers was presented on a theoretical base. The theoretical model is based on a theory developed for fiber splice and connector losses [7]. To validate the theoretical model designed, test structures were fabricated and characterized. Experiments showed that the type of light source and the manner in which the light is launched into the input (transmitting) fiber of the sensor is most important for transmission ratio. The experimental results using an LED light source were consistent with the simple theoretical model. The user of this shutter displacement measurement method can simply remind that the useful measurement range is above a tenth of the optical fiber diameter.

References:

[1] Jean Rossel, “Physique générale”, Edition du griffon, Neuchâtel 1970

[2] B.E.A Saleh, M.C. Teich, “Fundamentals of photonics” John Wiley and sons, 1991

[3] C.M. Miller, “Optical fiber splices and connectors”, AT&T Bell Laboratories, Marcel Dekker, Inc, New York, Basel, 1986

[4] D. Gloge and E.A.J. Marcatili,” Multimode theory of graded-core fibers”, Bell System Tech. Journal, 1973, 1563-1578

[5] C.M. Miller and S.C. Mettler, “A loss model for parabolic-profile fiber splices”, Bell System Tech. Journal, 1978, 3167-1579

[6] M. J. Adams, D. N Payne and F. M. E. Sladen, Applied Physics Letters, 28, 524, 1976

[7] C. M. Miller,“ Transmission versus transverse offset for parabolic – profile fiber splices with unequal core diameters”, Bell System Tech. Journal, 1976, 917-927.

[8] D. Gloge, “Offset and tilt loss in optical fiber splices”, Bell System Tech. Journal, 1976, 905-915

[9] P. DiVita and U. Rossi, 1978, “Theory of power coupling between multimode optical fibres”, Optical and quantum electronics, 10, 1978, 107-117

[10] S.C. Mettler, “A general characterization of splice loss for multi-mode optical fibers”, Bell System Tech. Journal, 1979, 2163-2182.

[11] M. Eckerle, “Mode coupling analysis in optical multimode step index waveguides and their application” VDI Verlag, Reihe 10, Nr. 319, 1994, Düsseldorf

[12] I. A. White and S. C. Mettler, "Modal analysis of loss mode mixing in multimode parabolic index splices", Bell System Tech. Journal, 1982, 1189-1207.

[13] R. B. Kummer, "Light guide splice loss – effects of launch beam numerical aperture", Bell System Tech. Journal, 1979, 441-447.

3 Micro-machined accelerometer based on optical fibers

3.1 Basic principle

The principle of an acceleration sensor is shown in Figure 3.1. A seismic mass m is suspended with a spring in a sensor package. When the sensor is moved with an acceleration a, a relative displacement x of the seismic mass is produced by the inertia force and is detected as an electrical signal. The motion equation is given by:

(3.1) $ma = m \cdot \ddot{x} + c \cdot \dot{x} + k \cdot x$

where k is the spring constant and c the damping constant due to the viscosity of the medium. In the steady state, the relationship between the displacement x and the acceleration a is

(3.2) x/a=m/k

This means the sensitivity of the sensor, x/a, is proportional to m/k. On the other hand, the same ratio m/k dictates the resonance frequency of the damping-free system, f_r:

(3.3) $$f_r = 2\pi\sqrt{(k/m)}$$

Comparison of equations (3.2) and (3.3) leads to the conclusions that high sensitivity results in a low resonance frequency. The resonance frequency therefore limits the operational frequency range of a sensor, and sensor design must compromise for these opponing tendencies. To detect the displacement x of the seismic mass, there are two main possibilities, either to monitor the strain induced in the spring or to directly determine the position of the seismic mass. Before presentation of the optical shutter modulation technique for measurement of acceleration, the following sections briefly discuss [1] the most common techniques used in conjunction with silicon accelerometers to detect the movement of mass, based on piezoresistivity and capacitance.

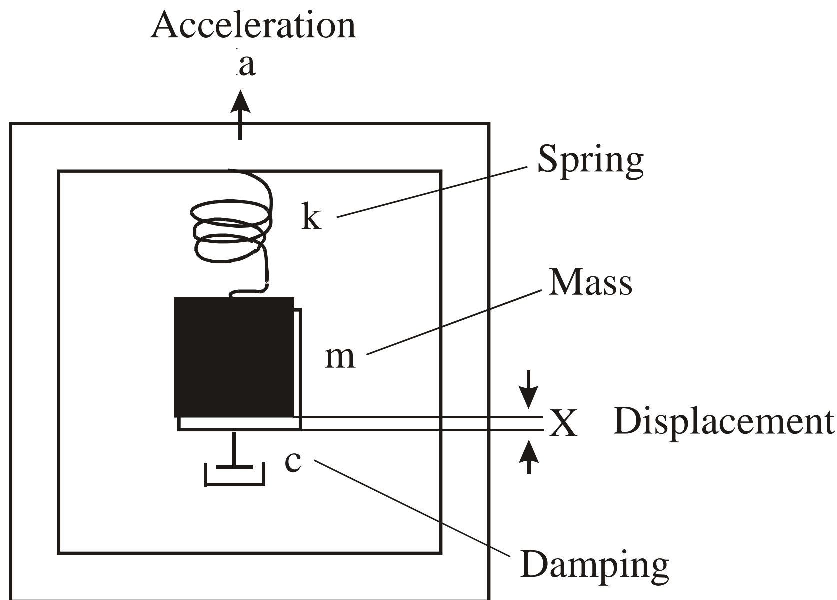

Figure 3.1: Accelerometer principle

Capacitive displacement measurement

The mass of the accelerometer forms an electrical capacitance together with an electrode fixed on the frame. A movement of the seismic mass due to applied acceleration changes the capacitance of this parallel-plate capacitor. In order to have a reasonable capacitance change, the mass and the outer electrode are separated by a few microns (≈ 2 µm). This small cavity leads to an over-damping of the sensor at atmospheric pressure. Thus, the pressure inside the cavity has to be reduced and to be well controlled, which complicates the production process. An other problem with capacitive sensors is that the external leads to the sensor tend tend to have stray capacitances which are of the same order of magnitude as the sensor itself. This makes it necessary to include electronic circuitry on the sensor chip in order to convert the change in capacitance (some pF) into an electrical signal. The advantage of this approach is higher sensitivity in comparison to the piezo-resistive effect, which is described below.

Piezoresistive strain measurement

Most solid state sensors for mechanical measurements are based on this effect. The change in specific conductivity due to an applied strain is defined as piezoresistance. The first silicon micromachined accelerometers with integrated packaging used this detection principle [2]. Two great advantages of the piezoresistive principle are that a true DC response can be measured (in contrast to most piezoelectric sensing techniques), and secondly, that no electric circuitry is needed for the detection of voltage change.

Optical intensity measurement

Intensity-modulated sensing, like all optical communication systems finally, is based on the detection of optical intensity. In low frequency, intensity-based optical sensors, the detected optical power and desired bandwidths are usually such that the sensitivity of detection is principally limited by the shot noise [3]. Thermal noise and dark current at the input to the detection electronics are not significant. Under these circumstances, the signal-to-noise ratio (SNR) in the photo current power of the detector diode can be expressed as

$$SNR = \frac{\bar{i}^2}{\sigma_i^2} = \frac{\bar{i}}{2eB} \qquad (3.4)$$

where

$\bar{i} = e\eta\Phi$ photocurrent mean

$\sigma_i^2 = 2e\bar{i}B$ photocurrent variance

η = quantum efficiency of the detector

e = elementary charge

Φ = photon flux

B = bandwidth of the optical receiver

In an operational system there are further sources of noise. Noise can be generated by the light source itself as well as by the source driver electronics and power supplies. Photocurrent amplification also contributes noise (1/f) [4] to the final voltage output.

3.2 Accelerometer mass displacement detection with shutter modulation

In Chapter 2 the light power transmission was modeled and measured as a function of micromachined shutter position. Shutter displacement sensitivities (slope of the light power transmission ratio versus shutter displacement curve) in the order of 0.04 μm^{-1} for an LED source and up to 0.08 μm^{-1} for an SLD source were obtained with single-mode fiber packaging. As discussed previously the optical power detection is limited by the shot noise. This means that theoretically, with an LED injecting 10 μW into a multi-mode optical fiber and a detection bandwidth of 1 kHz, a shutter displacement resolution of clearly less than a nanometer can be achieved.

Accelerometer design considerations using shutter modulation

Important parameters for accelerometer mass displacement detection are the shutter displacement available and the displacement sensitivity. Displacement sensitivity is highest for a shutter position where half of the light is blocked and the other half of the light is coupled into the receiving fiber (fig. 3.1). If the fibers are ideally aligned, this position is also the center of a linear shutter displacement response (fig. 2.11). An accelerometer must therefore be designed in such a way that the shutter may be found in this particular half power position at zero acceleration.

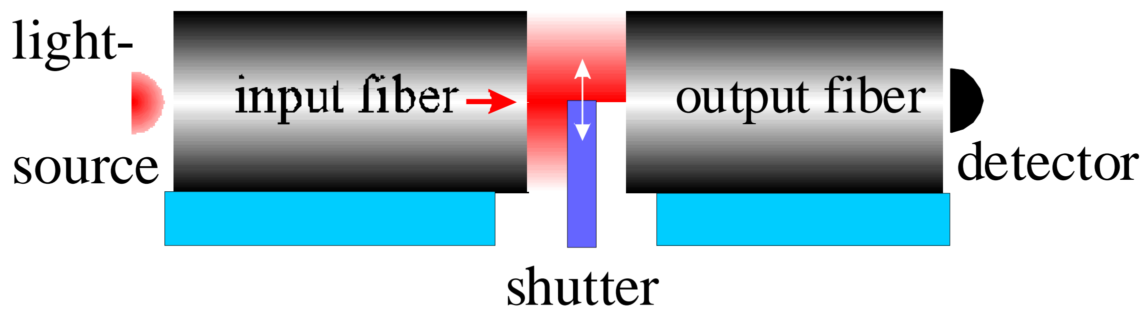

Figure 3.2: detection principle in more details

In Chapter 2 the experimental curves (fig. 2.11 and 2.13) show a linear response for shutter displacements of more than 6 µm. In this range the linearity is better than 2%. These curves are plotted with the half power position (transmission ratio of 0.5) at a shutter displacement value of zero microns. This is done to ensure graph clarity, but also because the precise core center position of the multi-mode fibers is unknown. Indeed, in reality the half power position can vary from one device to another due to alignment errors. One error is the transversal misalignment of the fiber cores (figure 2.8). A second alignment error source is the relative position of the shutter compared to the core center of the transmitting fiber. Experience has shown that the half-power position varies with a similar magnitude of ±1.5 microns. Assuming that the linear range center varies with a similar magnitude results in a reduced useful linear range remaining for mass displacement detection. In the worst case, this displacement measurement range (linear range of 6 microns) would be ±1.5 µm (fig 3.3).

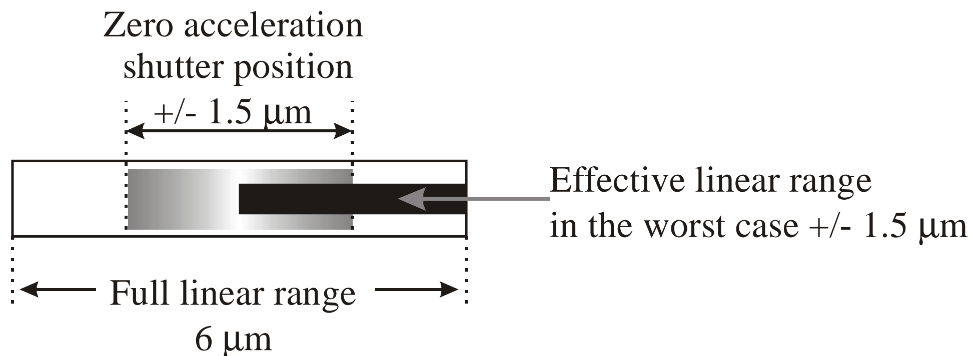

Figure 3.3: Linear range for mass displacement measurement. Assuming a worst case situation where the zero acceleration position of the mass (shutter) is not centered in the linear range of transmission versus shutter position curve.

For accelerometer mass displacement detection, a measurement range of ±1µm should therefore not be exceeded.

Another practical limitation for acceleration measurement is maximum acceleration amplitude limit. On earth, gravity corresponds to an acceleration of 1g. The seismic mass acceleration, depending on the orientation of the accelerometer, can be biased by a value of –1g up to 1g. The lowest acceleration amplitude measurement range for an accelerometer from a practical stand point of view is therefore ± 2g. With these two limiting values inserted into equation 3.2 yields another important value, namely the higher limit for the mass over stiffness factor. This factor in its reciprocal form determines the resonance frequency of an accelerometer. Assuming that the mass center displacement is limited to ±1µm, the lowest resonance frequency possible is 700 Hz.

3.3 Mechanical design considerations

In an accelerometer there are various ways to suspend the seismic mass using beams. The most common configurations are the cantilever and the bridge suspensions [1]. Another possibility is, for instance, the torsional beam suspension. In the previous chapter, a cantilever test structure for analyzing shutter modulation was discussed. In order to have a similar configuration and also because mass displacement can be measured externally by interferometric methods, a vertical seismic mass displacement with cantilever suspension was chosen for the first accelerometer design (fig 3.3).

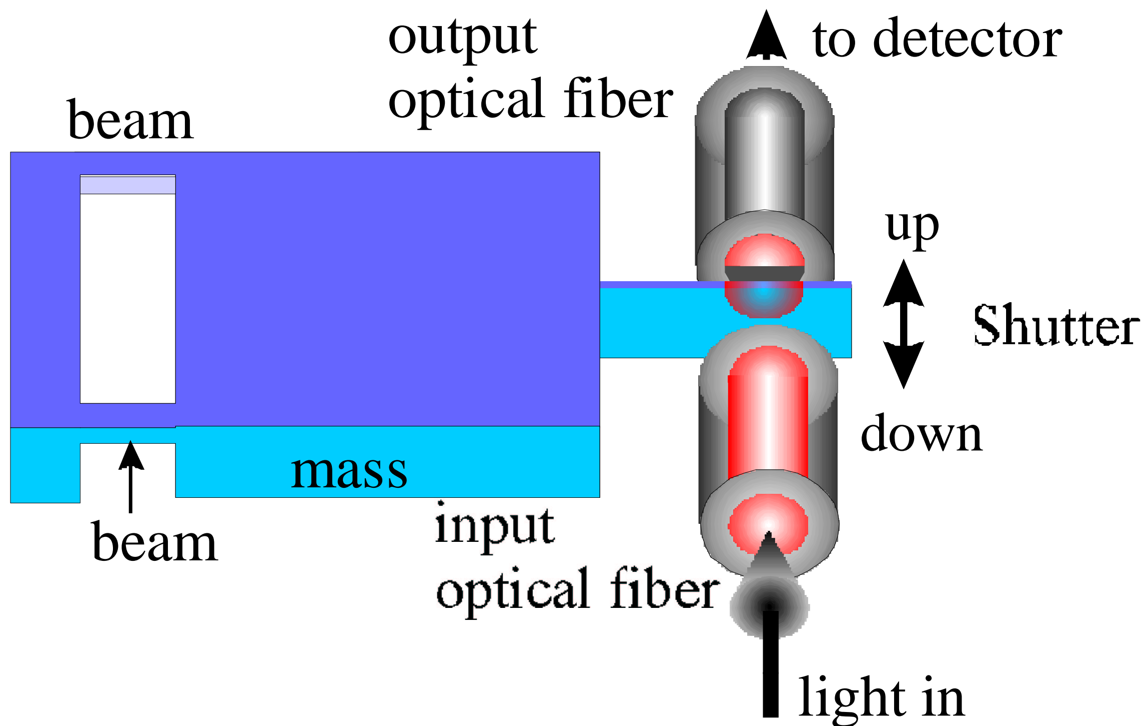

Figure 3.4: Basic principle. As the shutter moves up or down, less or more light is coupled from one fiber to the other.

Formulae for the cantilever-type accelerometer

For analytical calculations the structure shown in (fig. 3.4) is replaced by a massless beam structure with well-defined boundary conditions [5]. The force and momentum equations are therefore:

Table 3.1 Analytical formulae for the cantilever-type accelerometer

Beam deflection	$z(x)=\frac{m\cdot a}{2\cdot E\cdot I_y}\cdot x^2\cdot\left\{\left(L+\frac{S}{2}\right)-\frac{1}{3}x\right\}$	for x≤L,
"	$z(x)=z(L)+\frac{dz}{dx}(x=L)(x-L)$	L ≤ x ≤ L+S
Stress at surface	$\sigma_x(x)=\frac{m\cdot a\cdot T}{2\cdot I_y}\cdot x^2\cdot\left\{\left(L+\frac{S}{2}\right)-x\right\}$	
Resonance frequency	$f_0=\frac{1}{2\Pi}\sqrt{\frac{E\cdot I_y}{m\cdot L^3}\cdot\frac{4+6\frac{S}{L}+3\left(\frac{S}{L}\right)^2}{\frac{4}{3}+4\left(\frac{S}{L}\right)+\frac{21}{4}\left(\frac{S}{L}\right)^2+\frac{7}{2}\left(\frac{S}{L}\right)^3+\left(\frac{S}{L}\right)^4}}$	

L=beam length

T=beam thickness

W=beam width

E=young's modulus

$I_y=\frac{1}{12}WT^3$ = moment of inertia

n= number of beams (n≥2)

a= acceleration

m= seismic mass

x= coordinate axis with origin at the frame end

S= length of the rectangular seismic mass

Design

The goal of the first design was to fabricate a device using the shutter modulation technique described in the previous chapter. As there were no precise technical specifications to specify, the fabrication process could be kept as practical and simple as possible. In order to be able to measure small mass displacements with an external interferometer, a sensitive accelerometer was most suitable. Therefore, the accelerometer was designed for the lowest acceleration amplitude range of ±2g. Following a similar fabrication process as for the test structures presented in the previous chapter, the beam thickness was kept same as the shutter height and fiber groove depth. The beam thickness was dictated by the shutter-height, which needed to be equivalent to the fiber radius, i.e. 62.5 μm, for optimum performance. The accelerometer was designed for a shutter displacement of approximately 0.33 μm for 1g vertical acceleration. This yielded a full scale displacement of ± 0.66 μm, which corresponds to two thirds of the limit deduced previously. The proposed design parameters are summarized in the following table:

Table 3.2: accelerometer design parameters, calculated using the formulae in Table 3.1

beam length	L= 250 μm
beam thickness	T= 61 μm
beam width	W= 125 μm
number of beams	2 side by side
seismic mass thickness	Tm= 370 μm
Length of the seismic mass	Lm= 6 mm
Width of the mass	Wm= 1.0275 mm
Mass	m=5.3 mg
Resonance frequency	1.1 kHz

3.4 Fabrication

Double-sided photolithography with 10 µm of AZ 4562 photo-resist was performed on a silicon-on-insulator (SOI) wafer containing a 61 µm top and 307 µm bottom silicon layer with a buried 2 µm layer of oxide in between. The vertical shutter (fig. 3.5), the fiber grooves (fig. 3.6), the cantilever beams and the front side mass structure were fabricated by DRIE. Backside etching to shape the mass and to liberate the moving part of accelerometer was also performed in this way. (Fig. 3.6) shows the shutter and (fig. 3.7) the cantilever beams and a part of the mass viewed from the backside. The buried oxide layer serves as a double-side etched stop. After stripping the photoresist and cleaning with piranha (conc. H_2SO_4 : 30% H_2O_2, 3:1) the remaining buried oxide was removed in a buffered hydrofluoric acid (BHF) bath. To have optically sufficient shutter quality, a gold layer was deposited by e-beam evaporation. Finally, the fibers were inserted and bonded with UV sensitive glue.

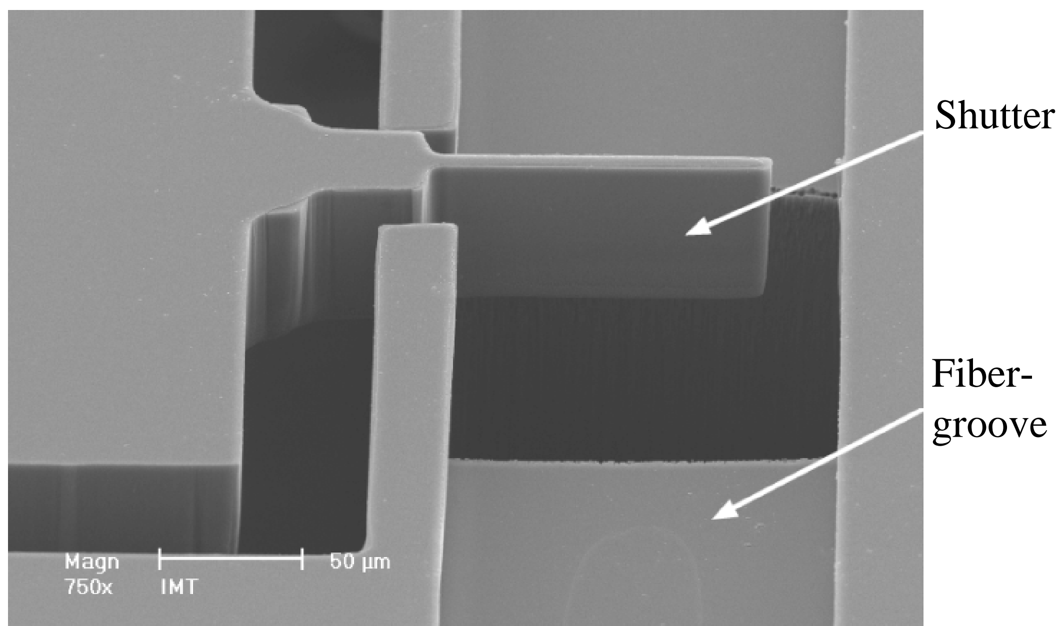

Fig 3.5: SEM of shutter and fiber grooves.

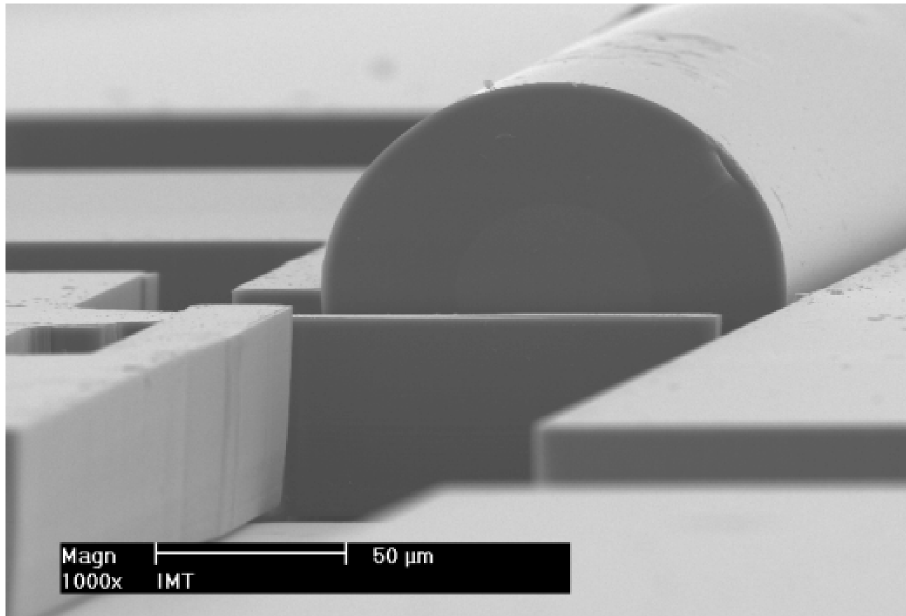

Fig 3.6: SEM picture of a multi-mode fiber behind the shutter.

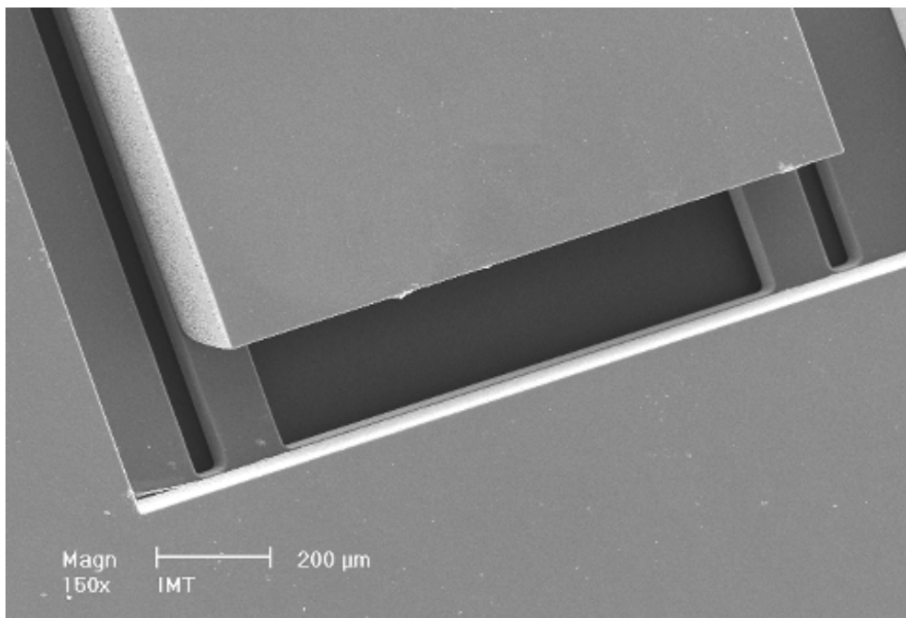

Fig 3.7: SEM picture of the back part and cantilever beams

3.5 Characterization

The characterization consisted of three sets of experiments. All of them were performed with an SLD light source. In the first set, the frequency and amplitude response were measured using a lock-in amplifier. The second part involved demonstrating the use of an economic LED as next-generation accelerometer light source. The noise-equivalent acceleration was also measured. Finally, the seismic mass displacement was measured directly with an interferometric vibration measurement set-up.

Frequency and amplitude response

For the characterization of the accelerometer, the input (transmitting) fiber was connected to a SLD source with a wavelength of 840 nm. The output (receiving) fiber was connected to a photodiode, the signal of which was converted by a current to voltage conversion circuit with a bandwidth of 3.5 kHz. Maximum detected power in these experiments was 50 μW. The reference accelerometer and the prototype accelerometer were mounted on a shaker. The amplitude (~1g) of the accelerations was monitored by the reference accelerometer. The output signal of the prototype devices was recorded using a lock-in amplifier [6]. (Figure 3.8(b)) shows the result of the frequency response measurement. The measured resonance frequency of 1089 Hz corresponds well with the calculated value of 1079 Hz. Amplitude response measurement was performed at 133 Hz, and shows a linear range of ±5g (fig. 3.8(a)).

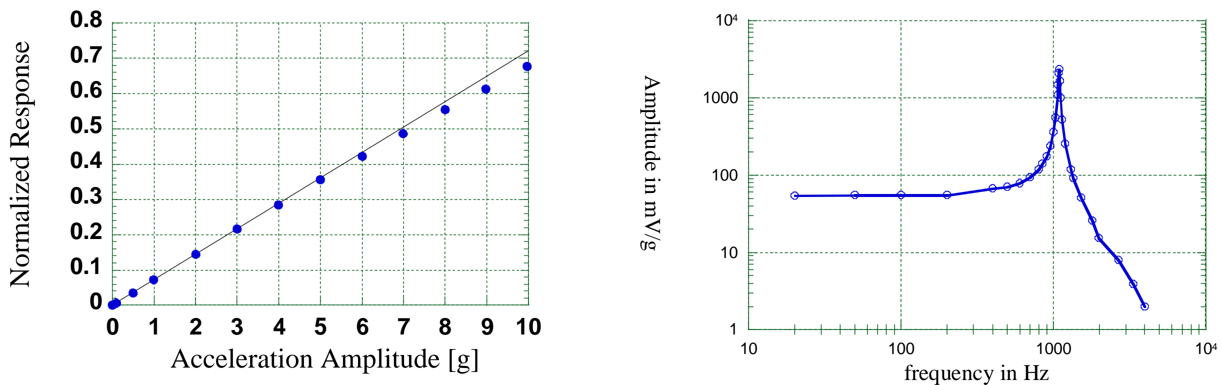

Figure 3.8: (a) Amplitude and (b) frequency response

Time domain measurements with low light power

This part of the characterization invoked a low input power experiment to simulate an LED light source. The SLD source coupled 1.8 µW into the transmitting fiber of the accelerometer. The photodiode amplifier had a bandwidth of 500 Hz. (Figure 3.9) shows the photodiode amplifier output signal for three different acceleration values around 1g at 133Hz. The voltage amplitudes at this frequency were around 650mV (fig 3.9). The noise level of the voltage output of the photodiode amplifier was measured with the shaker switched off. The standard deviation of this voltage output was 1.25 mV, which corresponds to an acceleration of 2 mg. Assuming that real shutter displacement sensitivity is close to the designed value of 0.35 µm/g a displacement resolution less than 1nm is obtained. The real shutter displacement value was measured in the following experiment.

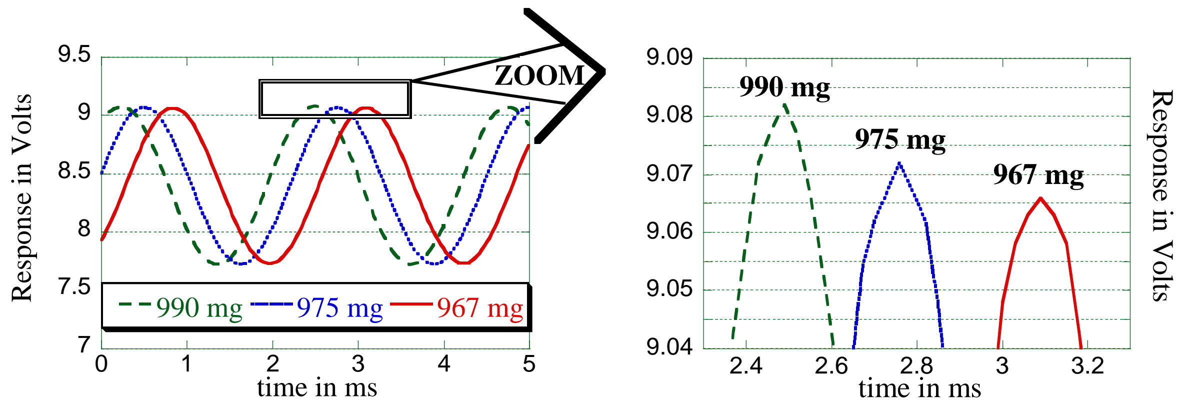

Figure 3.9: Time domain response to accelerations around 1g amplitude at 133 Hz

Direct mass displacement measurement

A Mach-Zehnder interferometer allows the determination of resonance frequencies and mass displacement in function of the acceleration. For this experiment the sensor chip was mounted on a piezoceramic disc. Hence only extremely small displacements and accelerations could be applied. In spite of the small accelerations applied, the high resolution of the interferometer (on the order of Angströms) allows the determination of the amplitude of mass motion. The mass-movements measured in this way resulted in a displacement sensitivity of 0.34 µm/g. The displacement resolution was therefore below 1 nm. Using the measured shutter displacement sensitivity and linear acceleration amplitude range at 133 Hz, the linear shutter displacement range (linearity is better than 1%) was ±1.3 µm.

3.6 Conclusions on the first generation accelerometer

The combination of DRIE and multi-mode optical fibers made possible the fabrication of a simple but sensitive fiber optic accelerometer machined on a single chip and capable of detecting acceleration direction. Its structure was based on a mass suspended by two side-by-side cantilever beams. A vertical shutter at the free end of the mass would move vertically in the optical path between two multi-mode optical fibers. This micromachined optical shutter modulation technique was investigated in the previous chapter and applied to this simple accelerometer, where it exhibited a displacement resolution of less than 1nm. This corresponds to an improvement of a factor 10 compared to a recently published integrated wave-guide accelerometer [7] using a laser source. The shutter displacement range, where linearity is better than 1%, is ±1.3 µm, which is close to the value estimated in the previous chapter. The time response to a sinusoidal acceleration shows no apparent non-linearity. The decision made in the previous chapter to neglect possible diffraction effects in the model was therefore correct for small displacements about the half power point.

References:

[1] H.H. Bau, N.F. de Rooij and B. Kloeck, “Sensors”, Volume 7, VCH Verlagsgesellschaft, Weinheim, 1994.

[2] L. M. Roylance, J. Agnell ,“A batch-fabricated silicon accelerometer”, IEEE Trans. on Electron Devices, ED-26 (1979), 1911-1917.

[3] B. Culshaw and J. Dakin, “Optical fiber sensors” Volume 2, Artech House, Inc., 1989.

[4] Jerald Graeme, “photodiode amplifier”, McGraw-Hill, New York, 1996.

[5] J. M. Gere and S. P. Timoshenko, “Mechanics of materials”, PWS-Kent publishing company, Boston, 1984.

[6] O. Bochobza-Degani, et al., “Comparative study of novel micro-machined accelerometers employing MIDOS”, Proc. IEEE, MEMS 1999.

[7] Ollier E., P. Lebey and P. Mottier,” Integrated micro-opto-mechanical vibrations sensor connected to optical fibers”, Electron. Letters, 6, 525-526, 1997.

4. Fiber optic MEMS accelerometer with integrated damping

In the previous chapter, a basic micro shutter-modulated optical-fiber-based accelerometer was designed, fabricated and characterized. The goal of the second generation accelerometer presented in this chapter was to use the same detection method as the first generation, but optimized for a damped resonance. Resonance damping is important against breakage, increases the usable frequency range and avoids detection non-linearity. Today all important commercial silicon microfabricated accelerometers are damped. With respect to detection the sensitivity to light source fluctuations was greatly reduced.

4.1 Introduction to viscous damping

Every accelerometer sensor chip is a resonant structure and therefore has to be damped in order to increase its useful frequency range and reduce the risk of breakage. Up to now, this has generally been achieved by enclosing the moving mass into a small cavity. The seismic mass immerged in gas or liquid layers can result in a flat response over a wide frequency range. The viscosity of the damping fluid as well as the thickness of the damping layer determines the damping characteristics. Since damping methods are mainly

based on viscous damping, section 4.2 is dedicated to this theory. A summary of publications on electronic accelerometer encapsulation and damping is given in [1]. In the case of capacitive accelerometers, the distance between the electrodes is so small (few microns) that air pressure needs to be reduced to just a few Torr's. For piezoresistive accelerometers, no electrodes are needed. The air cavity thickness can be increased to achieve critical damping at atmospheric pressure. To our knowledge, only one micro-machined optical accelerometer reported to date has been damped [2]. However that sensor most likely suffered from non-linear amplitude response. This chapter demonstrates how damping structures can be integrated into a fiber optic based accelerometer without increasing fabrication and packaging complications.

Squeeze film theory, discussed in this section, is based on the fact that for fluid films, the damping force is proportional to the velocity of the moving body (=c$\dot{x}$). This condition is called viscous damping and may be exploited in conjunction with the accelerometer presented here. In order to calculate the cavity size required for critical damping with a particular fluid the main characteristics of a viscous-damped, spring–mass system are viewed in this section. The differential equation of motion for forced vibration of a viscous-damped, spring-mass system is:

$$m\ddot{x} + c\dot{x} + kx = Q\cos(\omega \cdot t) \qquad (4.1)$$

where k is the spring constant, c is the coefficient of viscous damping, m is the seismic mass and Q is the amplitude of forced vibration.

The general solution of equation 4.1 is:

(4.2) $$x = e^{-dt}\left(C_1 \cos p_d t + C_2 \cos p_d t\right)$$

where $b^2 = \frac{k}{m}$, $d = \frac{c}{2m}$, $p_d = b^2 - d^2$ and C_1 and C_2 are constants determined from the initial conditions.

A particular solution of equation 4.1 is:

(4.3) $$x = \frac{Q}{k}\beta \cos(\omega t - \theta)$$

in which β is the magnification factor and θ the phase angle. β is given by:

(4.4) $$\beta = \frac{1}{\sqrt{\left(1-\omega^2/b^2\right)^2 + (2\gamma\omega/b)^2}}$$

where γ the damping ratio given by:

(4.5) $$\gamma = \frac{d}{b} = \frac{c}{2\sqrt{km}}$$

(4.6) $$\theta = \tan^{-1}\left(\frac{2\gamma\omega/b}{1-\omega^2/b^2}\right)$$

The general solution represents damped free vibrations, whereas the particular solution represents damped forced vibrations. The free vibrations have a frequency p_d , whereas the forced vibrations have a frequency ω,

which is identical to the period of the disturbing force that produces them. As indicated by the factor e^{-dt}, the free vibrations gradually subside, leaving only the steady-state forced vibration represented by the particular solution. Steady-state forced vibration with viscous damping is a simple harmonic motion having constant amplitude β Q/k, phase angle θ and period $2\pi/\omega$.

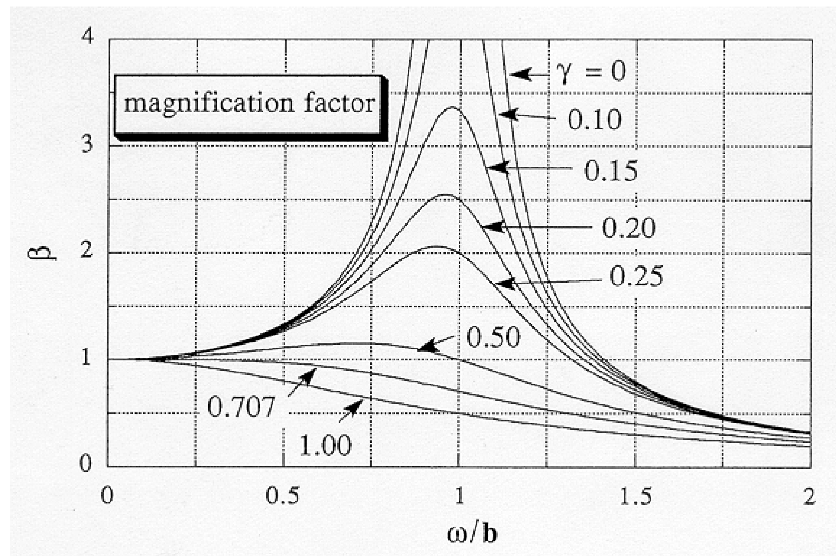

Figure 4.3: Magnification factor β plotted against the ratio ω/b for various levels of damping.

From equation 4.3, it can be seen that the amplitude of the steady-state forced vibration is obtained by multiplying the static-load displacement Q/k by the magnification factor β. This factor depends not only upon the frequency ratio ω/b, but also upon the damping ratio γ. Figure 4.3 shows the magnification factor β plotted versus the ratio ω/b for various levels of damping. From these curves it can be observed that when impressed angular frequency ω is small compared with the natural angular frequency b, the value of the magnification factor is about unity. Thus, during vibration the displacements x of the suspended mass are approximately those which would be produced by the static action of the perturbing force Qcos(ωt).

When ω is large compared to b, the value of the magnification factor tends towards zero, regardless of the amount of damping. As the value of ω approaches that of b, the magnification factor grows rapidly, and its value at or near resonance is very sensitive to changes in the amount of damping. It should also be noted that the maximum value of β occurs for values of ω/b slightly less than unity and $\gamma > \sqrt{2}/2$. Setting the derivatives of β with respect to ω/b equal to zero, we find that the maximum β occurs when

(4.7) $$\frac{\omega}{b} = \sqrt{1-2\gamma^2} = \sqrt{1-\frac{c^2}{2mk}}$$

If $\gamma = \sqrt{2}/2$, the system is called critically damped and β reaches a maximum for ω=0, the magnification factor is ≤ 1 for any frequency. For $\gamma > \sqrt{2}/2$ the spring mass system is over-damped, while for $\gamma < \sqrt{2}/2$ it is under-damped. The phase relationship between the steady-state vibrations and the perturbing force is represented by the phase angle θ in equation 4.3. The curves in (fig. 4.4) show the variation in the phase angle θ with the ratio ω/b for several levels of damping γ. When damping is present there is a continual change in θ as the ratio ω/b increases. Also, regardless of the amount of damping, $\theta=\pi/2$ is found at resonance. The damping factor γ depends on the viscosity of the fluid [3]. Therefore, the damping characteristics depend on pressure and temperature. Basically, there are two ways to define a fluid viscosity:

a) Dynamic viscosity η [Pa s]

b) Kinematic viscosity ν [m^2/s], defined as the dynamic viscosity divided by the density, $\nu=\eta/\rho$, where ρ=density.

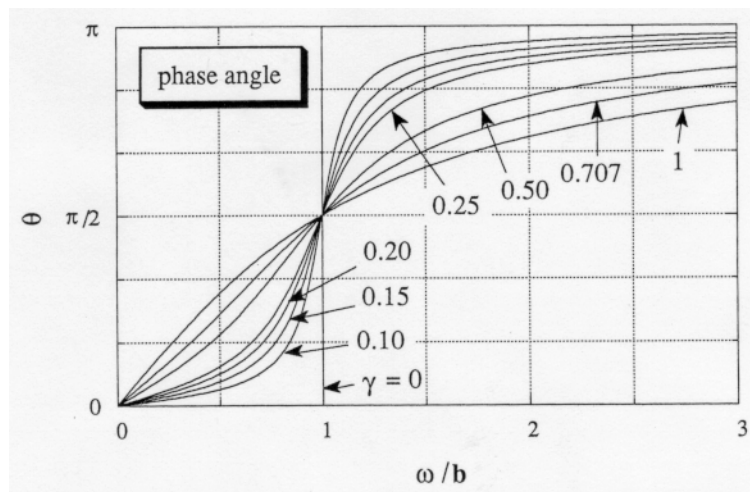

Figure 4.4: Phase angle θ plotted against the ratio ω/b for various levels of damping γ.

Temperature dependence of viscosity:

The dynamic viscosity of liquids decreases with increasing temperature due to the temperature dependence of the inter-molecular attractive forces, which act between the different liquid particles. However, the dynamic viscosity of gases and vapors increases with increasing temperature. There are no formulas for the description of the temperature dependence of viscosity. Furthermore, the viscosity in liquids is in general more temperature dependent than in gases.

Gas damping has certain advantages over liquid damping. The temperature dependence of the viscosity is lower for gases. Additionally, the buoyant force, which acts on the vibrating structure immersed in the liquid, leads to significant loss in sensitivity. Also, an accelerometer damped with air at atmospheric pressure can be realized without being hermetically sealed.

4.2 Gas-damped accelerometer

The damping is due to the internal friction of the flowing fluid in small clearances between moving elements. Micromachining offers the possibility to shape structures which incorporate very thin fluid layers. These thin fluid layers are an excellent means of viscous vibration dissipation even if the fluid is a gas. To our knowledge, the first theory of squeeze film for the design of accelerometers was published by J. Starr [4]. In this section, the main formulae of the squeeze film theory published by J. Blech [5] are reviewed. Based on the formulae of a compressible squeeze film, the spring and viscous damping forces of a thin air-film will be calculated. Theory shows that the spring force is negligible compared to the viscous damping force. The theory is known for the calculation of squeeze film between two rectangular parallel plates moving one with respect to the other (fig 4.2). Damping arises from the internal friction of the flowing gas in small clearances between the moving plates. Following text is partly taken from the thesis of Tschan [1].

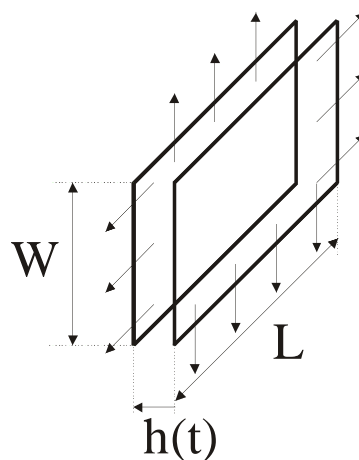

Fig. 4.5: damping plates

If film conditions are steady, the momentum equation may be combined with the continuity relation to give the Reynolds equation, a single differential equation relating pressure, density, surface velocities and film thickness. The combination of momentum and continuity allows the distributed film velocity to be eliminated and replaced by film surface velocities. Unless slip is present, these velocities are identical to the velocities of the adjacent surfaces. Slip flow can become important only with gas films. The Knudsen number, $Kn = \lambda/h$, (λ is the mean free molecular path and h is the film thickness) is a measure of the average number of molecular collisions in a given length. When $Kn < 0.01$, flow may be treated as continuum. When $0.01 < Kn < 15$, slip flow becomes significant, and for $Kn > 15$ fully developed molecular flow results. The mean free path of air molecules at room temperature and atmospheric pressure is about 0.09 μm. Thus, theoretically for a film thickness of < 9 μm, slip flow is not quite negligible. However, experience has shown that damping with a film thickness of 8 μm still is in good agreement with the theory valid for continuous fluids [1].

To solve the Reynolds equation, the following assumptions are made:

- The surface of the plates are substantially parallel and most of the motion is perpendicular to plate surfaces.
- The gas flow between the plates is assumed to be laminar and primarily viscous. This assumption implies low Reynolds numbers and parabolic velocity distribution across a gas film.
- The relationship between pressure p and density ρ at any point in the gas film is assumed to be described by a polytropic process with

exponent n: $\frac{p}{\rho^n} = constant$ (since our case the film is assumed nearly isothermal, we take n≈1)

- The separation h of the plates is very small compared with the linear dimensions of the plates.
- The variation of plate spacing is assumed to be small compared with the mean spacing h_0

$$h = h_0 + e \text{ where } e << h_0.$$

When the motion is of the nature just described above, we get:

$$\frac{h^3}{12\eta}\left(\frac{\partial}{\partial x}\left(p\frac{\partial p}{\partial x}\right)+\frac{\partial}{\partial y}\left(p\frac{\partial p}{\partial y}\right)\right)=\frac{\partial}{\partial t}(ph) \tag{4.8}$$

where p is pressure, h is film thickness, t is time and η is fluid viscosity. The boundary condition for (eq. 4.8) is

(4.9) $p=P_a$ at the plate boundaries, where P_a is ambient pressure

Equation 4.8 is a nonlinear partial differential equation which can be solved only for special cases by numerical methods. However, due to the fifth assumption, the variation in p will be small compared with the ambient pressure level P_a:

$$p=P_a+\delta p \tag{4.10}$$

where $\delta p << P_a$.

When eq. (4.10) is substituted into eq. (4.8) and second-order terms are neglected, a linear equation results. This equation, written in dimensionless form, yields:

(4.11) $$\Delta\psi - \sigma\frac{\partial\psi}{\partial\tau} = \sigma\frac{\partial\xi}{\partial\tau}$$

where $\psi = \partial p / P_a$ the non-dimensional pressure perturbation, σ is squeeze number as defined later in eq. 4.20, $\xi = e/h_0$, the dimensionless plate displacement, and τ is ωt, non dimensional time. The film response to a simple harmonic motion excitation can now be calculated. The plate spacing variation is given by:

(4.12) $$e = e_0 \cos\tau$$

where e_0 may vary over the plate surface, but is not a function of time. Equation 4.12 is in dimensionless form.

(4.13) $$\xi = \chi \cos\tau \quad \text{where } \chi = \frac{e_0}{h_0}$$

Equation 4.11 becomes

(4.14) $$\Delta\psi - \sigma\frac{\partial\psi}{\partial\tau} = -\sigma\chi\sin\tau$$

Assuming the solution to equation 4.14 has the form

(4.15) $\psi = \psi_0 \sin\tau + \psi_1 \cos\tau$

the pressure distribution has a component ψ_1 cos(τ) which is in phase with the film thickness perturbation $e_0$cos(τ), and a second component which is out of phase with the film thickness perturbation, but in phase with the squeeze velocity $e_0$sin(τ). Another interpretation of eq. 4.15 is that the fluid film acts as a spring and as a viscous damper ψ_0. Inserting eq. 4.15 into eq. 4.14 and equating coefficients of cos(τ) and sin(τ) separately one obtains:

(4.16) $\Delta\psi_1 - \sigma\psi_0 = 0$

(4.17) $\Delta\psi_0 - \sigma\psi_1 = -\sigma$

with trivial boundary conditions on both ψ_0 and ψ_1. The cutoff frequency is that frequency where the spring and damping force amplitudes are equal in f_0 and f_1

(4.18) $f_0 = f_1$

where f_0 and f_1 are the non-dimensional damping and spring pressure force amplitudes, respectively. The forces themselves are obtained by multiplying f_0 and f_1 by $P_a A$.

(4.19) $f_i = (-1)^{-i} \frac{1}{A} \int_A \psi_i \, dA;$ i=0,1

The squeeze number of a rectangular plate of dimension $l \times w$ is defined as

(4.20) $$\sigma = \frac{12\eta l^2}{P_a h_0^2}\omega$$

The solution of eq. 4.16 and 4.17 are

(4.21) $$\psi_0 = \chi \sum_{\substack{m,n \\ odd}} a_{mn} \cos m\pi x \cdot \cos\frac{n\pi y}{\alpha}$$

(4.22) $$\psi_1 = \chi \sum_{\substack{m,n \\ odd}} b_{mn} \cos m\pi x \cdot \cos\frac{n\pi y}{\alpha}$$

where

$$\alpha = \frac{w}{l} = \text{plate aspect ratio}$$

$$a_{mn} = \frac{16\sigma(-1)^{\frac{m+n}{2}}\left[(m\pi)^2 + \left(\frac{n\pi}{\alpha}\right)^2\right]}{\pi^2 mn\left\{\left[(m\pi)^2 + \left(\frac{n\pi}{\alpha}\right)^2\right]^{-2} + \sigma^2\right\}}$$

$$b_{mn} = \frac{16\sigma^2(-1)^{\frac{m+n}{2}}}{\pi^2 mn\left\{\left[(m\pi)^2 + \left(\frac{n\pi}{\alpha}\right)^2\right]^{-2} + \sigma^2\right\}}$$

The non dimensional damping and spring force amplitudes for a rectangular plate are obtained by eq. 4.19

(4.23) $$f_0 = \frac{64\sigma\chi}{\pi^6}\sum_{\substack{m,n\\ odd}}\frac{m^2+(n/\alpha)^2}{(mn)^2\left\{\left[m^2+(n/\alpha)^2\right]^2+\sigma^2/\pi^4\right\}}$$

(4.24) $$f_1 = \frac{64\sigma\chi}{\pi^8}\sum_{\substack{m,n\\ odd}}\frac{m^2+(n/\alpha)^2}{(mn)^2\left\{\left[m^2+(n/\alpha)^2\right]^2+\sigma^2/\pi^4\right\}}$$

Equating the force amplitudes gives an algebraic equation for the cutoff frequency. In general it is enough to maintain one term in the summations of this equation. This leads to a cutoff squeeze number of

(4.25) $$\sigma_c = \pi^2\left(1+\frac{1}{\alpha^2}\right)$$

Equating 4.20 and 4.25, ω_c, the cutoff frequency is obtained

(4.26) $$\omega_c = \frac{\pi^2 P_a h_0^2}{12\eta}\left(\frac{1}{l^2}+\frac{1}{w^2}\right)$$

In this way the cutoff frequency for the second generation accelerometer design can be calculated. Taking a damping plate length of 2 mm, a width of 125 µm, a plate spacing of 9 µm, ambient pressure of 1 bar, and viscosity of air at 25 °C =1.82 * 10^{-5} Pa s, results in a cutoff frequency of ≈ 2 MHz which is much greater than the designed resonance frequency of the accelerometer. Consequently, the squeeze film acts like a viscous damper for any cavity > 9 µm.

The non-dimensional spring and damping forces versus the squeeze number σ for different plate aspect ratios α are plotted in (fig. 4.3). The damping force reaches its maximum value approximately at the cutoff frequency. Excitation above or below this frequency results in a decreased damping force. When the relative velocity between the plates is low, the film is effectively incompressible and has enough time to escape from in between the plates. At high velocities, the film approaches a purely compressible state with no fluid flow, and the situation may be compared to a piston and cylinder. Consequently at low velocities, viscous damping forces are predominant, whereas at high velocities the spring force take over. If the frequency ω is much below the cutoff frequency $\omega \ll \omega_c$, only the first order terms of σ have to be considered as the squeeze number is then $\sigma<1$. Thus with eq. 4.23 and 4.24 with the first order approximation we find

(4.27) $$f_0 = \frac{64\sigma\chi}{\pi^6} \frac{1}{1+\left(\frac{1}{\alpha}\right)^2}$$

$f1 \approx 0$

Thus the plates at frequencies much below the cutoff frequency act as a viscous damper having the following damping constant c_{sq}

(4.28) $$c_{sq} = \frac{768\eta l^3 w}{h_0^3 \pi^6} \frac{1}{1+\left(\frac{1}{\alpha}\right)^2}$$

expressed in plate dimensions w and l only:

(4.29) $$c_{sq} = \frac{768\eta}{{h_0}^3\pi^6}\frac{l^3w^3}{l^2+w^2}$$

4.3 System design considerations

The design approach taken in this chapter is to combine as many mechanical and optical functions in a device made using simplest as possible fabrication and packaging process. A single mask fabrication process to fabricate the damped mass, suspension beams, shutters and fiber grooves is therefore optimal. The micro optical shutter modulation technique studied in chapter 2 and implemented in chapter 3 is extended to a differential detection method using two oppositely moving shutters instead. This allows a mass displacement signal which is nearly independent of the light source fluctuations to be obtained. The principle is shown in (fig. 4.2). The shutters are designed to couple half of the light beam from the input fiber to the output fiber through the air gap at zero acceleration. As the mass is displaced, for instance to the left, the coupling between the two left fibers is decreased and more light is coupled between the optical fibers on the right side.

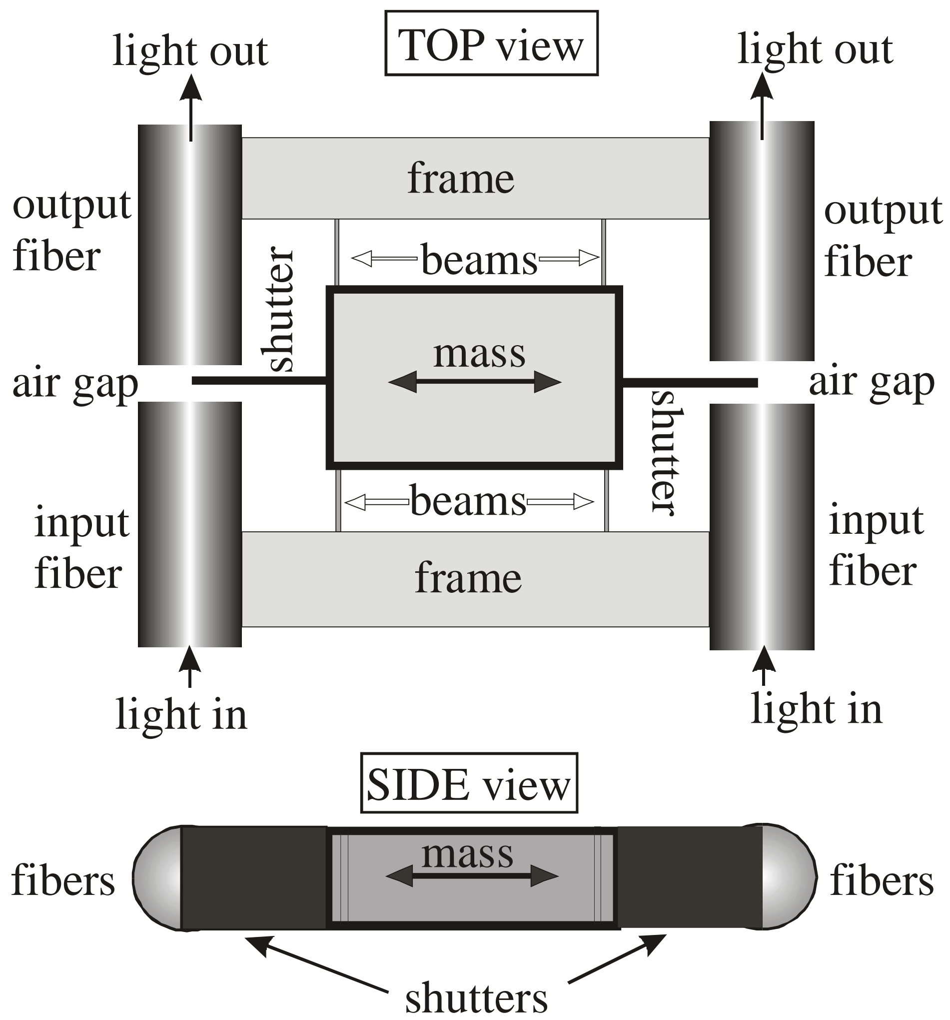

fig. 4.6: Accelerometer system.

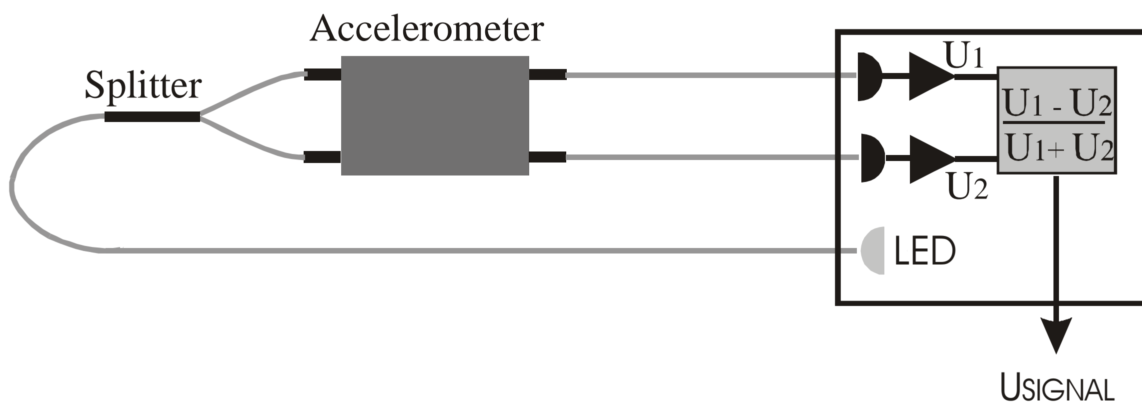

fig. 4.7: Accelerometer system. The electronics is contained in a box a few meters away from the accelerometer

The overall accelerometer system is based on an LED source, a multi-mode fiber coupler (50%:50%), the accelerometer chip, two detectors, two photodiode amplifiers and a signal processor, as shown in (figure 4.7). The concept is shown in figure. The shielded electronic box can be set up in a controlled environment meters away from the accelerometer itself. The output voltage U_{signal} of the accelerometer is the normalized difference of both photodiode amplifier outputs.

Mechanical design

The mechanical design of the accelerometer is optimized to achieve squeeze air film damping at room temperature and atmospheric pressure. The theory described in the previous section was developed for rectangular damping plates. The damping constant c_{sq} is then given by the equation 4.29. In the present design the damping plates are vertical to the wafer surface since the mass is moving laterally. The plate height is therefore given by the thickness of the upper layer of the SOI wafer. The silicon layer thickness is defined in the present design to correspond to the optical fiber diameter (125 µm), so that the optical fibers fit precisely into the fiber grooves. Viscous damping in air at atmospheric pressure and room temperature is theoretically ensured for air film thicknesses of 9 µm and greater. In practice however, a film thickness of 8 µm is still consistent enough with theory [1]. The theory (eq. 4.29) used in this chapter is valid under certain conditions. One condition is that the distance between the plates is assumed to be very small compared with the linear dimensions of the plates. In the present design the plate

height (or width) is 125 μm and the plate separation in air is minimized. Previously published damping plates had dimensions in the order of millimeters and plate separations of 4 μm to 13 μm. Their damping characteristics were consistent with theory [1]. In a first design it is therefore careful to choose at least the plate length of the present accelerometer in these dimensions. Other conditions for the damping theory validity is that the variation of the plate spacing be kept small compared with the mean separation, and that plates remain parallel under motion.

The fixed design parameters are:

- height of the moving structure must be equal to a fiber diameter (125 μm).

- width of the moving structure must be ~10 μm. To release the moving structure from the oxide layer, the chip is placed in a BHF bath. However the oxide layer under static structures may then also be etched away. Therefore, it is important to set an upper limit to etch time.
- width of static structures must be > 20 μm. To ensure that they are not released in the BHF bath, static structures need to be at least double the width of the moving structures.

- damping must function in air at atmospheric pressure and room temperature.

- To insure that the damping plates stay parallel during mass acceleration, the mass is suspended by four beams in a bridge-like arrangement (fig. 4.6). The analytical formulae for a bridge type accelerometer are listed in (table 4.1).

Table 4.1: Analytical formulae for bridge-type accelerometer (taken from Tschan [1])

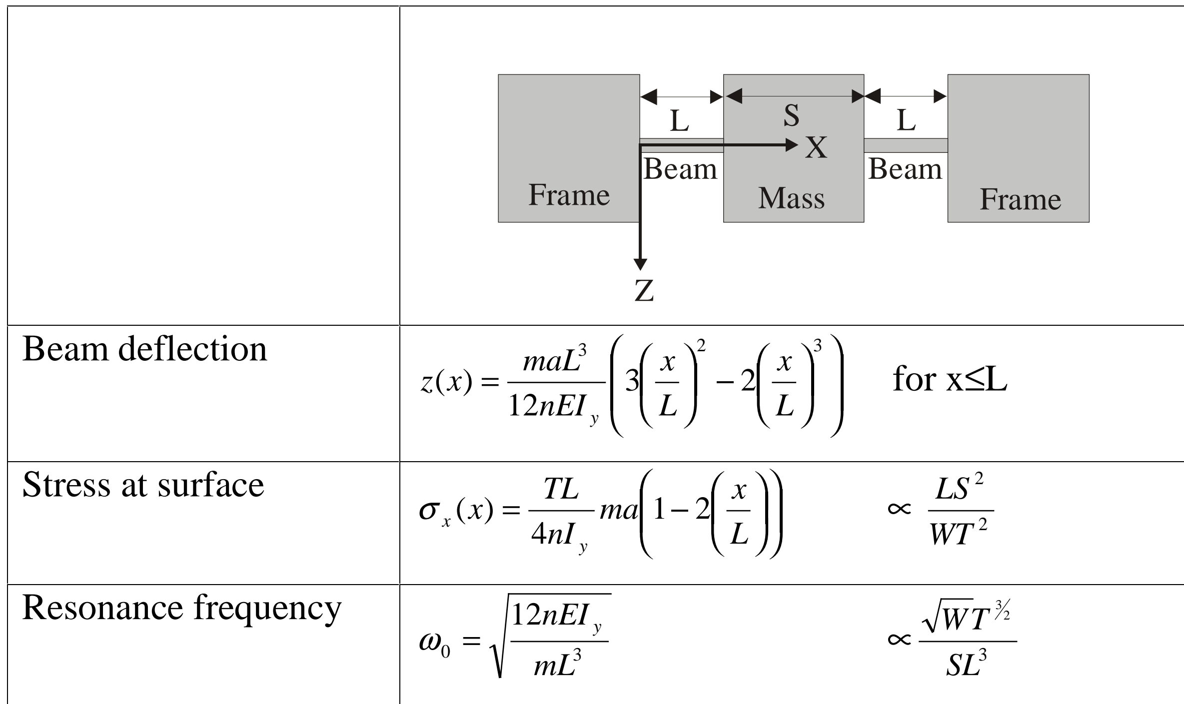

Beam deflection	$z(x) = \frac{maL^3}{12nEI_y}\left(3\left(\frac{x}{L}\right)^2 - 2\left(\frac{x}{L}\right)^3\right)$ for x≤L
Stress at surface	$\sigma_x(x) = \frac{TL}{4nI_y} ma\left(1 - 2\left(\frac{x}{L}\right)\right) \quad \propto \frac{LS^2}{WT^2}$
Resonance frequency	$\omega_0 = \sqrt{\frac{12nEI_y}{mL^3}} \quad \propto \frac{\sqrt{W}T^{3/2}}{SL^3}$

L is the beam length, T is beam thickness, W is beam width, I_y is the moment of inertia ($I_y = \frac{1}{12}WT^3$), n is the number of beams (n≥2), a is the acceleration, m the seismic mass, x is the coordinate along beam axis x with origin at frame end, S is the length of the quadratic seismic mass at the surface

The fixed design parameters lead to:

- A structural height of 125 µm determines the damping plate width. In order to have a very small plate separation compared to plate dimensions the mean air film thickness is set to a lower limit of 8µm.

- The mass displacement must be limited to a range which is much smaller compared the mean damping plate separation of 8µm. In order to fulfill this condition a mass displacement of ~ 0.1 µm/g seems to be adequate.

- thin damping plates with lengths in the millimeter range have certain criteria to fulfill in order to insure proper functioning:
    - damping structure resonance frequency must be much higher than the mass-spring structure.
    - The analytical solutions for viscous damping are valid for damping plates immersed in air at steady ambient pressure (fig. 4.5). The silicon plates must be fabricated in a manner as close as possible to the assumptions made to solve the Reynolds equation earlier in this chapter. Considering a series of vertical plates machined in a SOI wafers, this is not trivial. First, air flowing in or out of a damping plate pair may influence air flow into or out of another plate pair situated close by. Second, the bottom edge of a vertical damping plate is very close to the handle wafer surface. In general the distance between the moving structures and the bottom (handle) wafer is equal to the oxide layer thickness (2 µm). The air trapped at the bottom between two plates can in these conditions not freely flow in or out as assumed in theory. Device design and fabrication need to take constrains into account (fig 4.8).

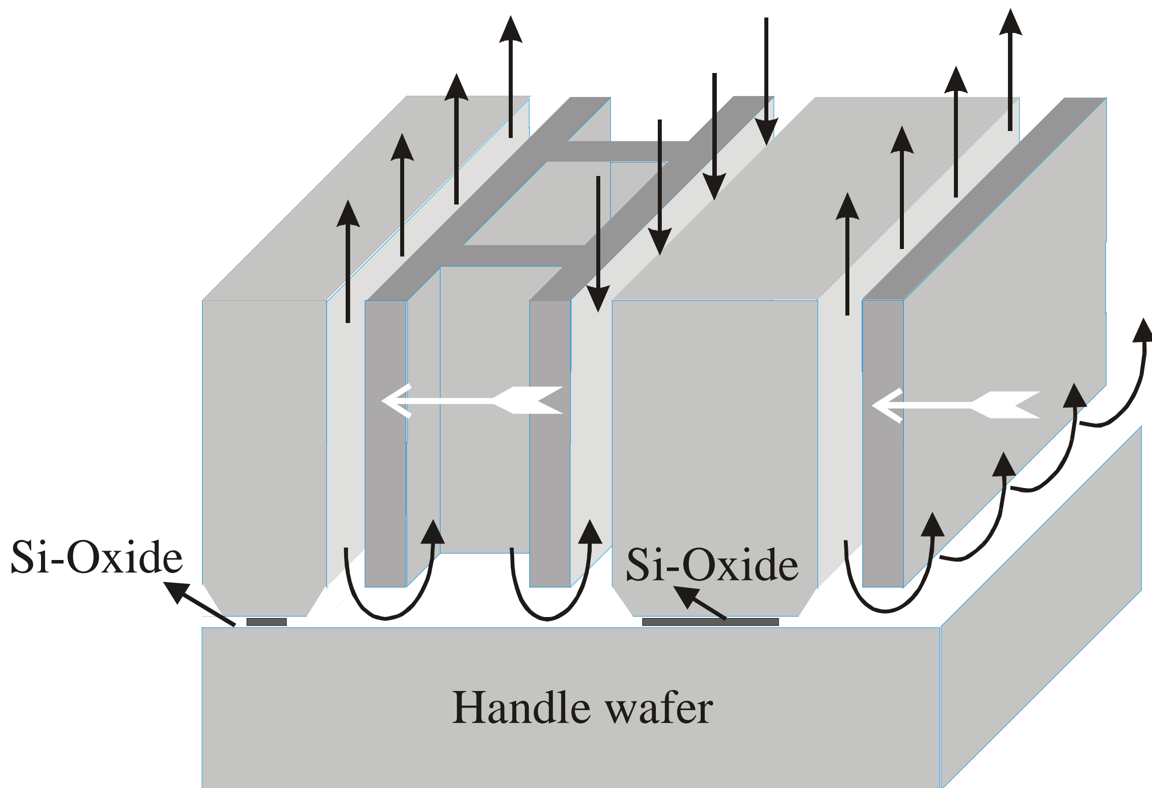

fig 4.8: Damping structures fabricated on a SOI wafer. The fixed damping plates are bonded with silicon oxide to the handle wafer. The moving damping plate structures (part of the accelerometer mass) are released. The black arrows show the air flow direction for a low frequency mass acceleration to the left. A real structure is shown in figure 4.

Fig. 4.8 shows a possible way to build damping structures in a more or less in acceptance with theory. The bottom part of the moving plates is etched away so that air can flow freely between the plates and the ambient pressure reservoirs, which are simply rectangular shaped holes in the moving structures. In order to fulfill their task of maintaining ambient pressure the volume of these reservoirs need to be much higher than the air volume displaced between the damping plates. It should also be noted that these reservoirs exchange air with two air gaps when moving. For a mass moving towards the left (fig. 4.4), some air flows from the left gap into the reservoir

and about the same amount of air flows from the reservoir into the right air gap.

Design parameters:

From the previous design considerations, the following design dimensions were calculated for device fabrication (tab 4.1). With the previously discussed design parameters, calculations show that critical damping can only be achieved with an air film thickness of 7µm. This thickness is below the theoretical limit of 9µm discussed in the previous section. It is however assumed that damping behavior is still close to the viscous model.

Suspension beam width	**10 µm**	(fixed)
Suspension beam length	0.63 mm	
Mass	1.9125 mg	
Square holes in the damping structures:	40*40µm	
Moving structure height	115 µm (**125µm** - 10µm)	
Number of main damping plate structures* (fig. 4.5):	50	
Number of side damping plate structures* (fig. 4.5):	100	
Length of main damping structure:	3.2 mm	
Length of side damping structure:	0.9 mm	
Width of moving damping structures:	60 µm	
Width of fixed damping plates:	60 µm	

*a damping plate structure consists of two moving plates (fig. 4.4)

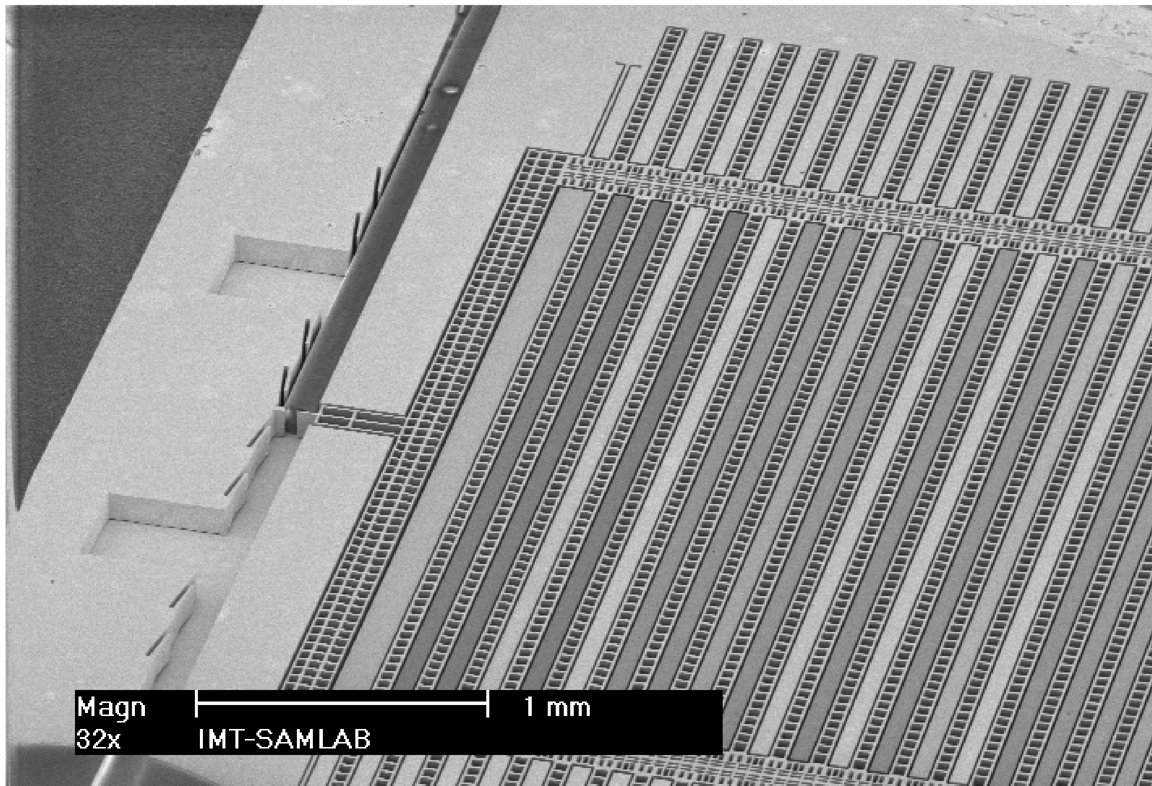

Fig. 4.5: SEM picture of the accelerometer. The mass of the accelerometer is the structure with square holes. On the top and the bottom the side damping plate structures can be seen. The main damping structures are in the central part of the mass. On the left, the shutter and a self aligned fiber can be seen.

4.4 Fabrication

Photolithography with 6 µm thick photoresist is performed on a silicon-on-insulator (SOI) wafer of 127µm top silicon layer thickness on a 2 µm thick buried oxide. The total wafer thickness is 480 µm. Suspension beams (fig. 4.11), a mass with squeeze film damping structures (Fig. 4.10, 4.11, 4.12, 4.13), 2 shutters for light intensity modulation and fiber grooves (fig. 4.10) are fabricated by Deep Reactive Ion Etching (DRIE) (fig. 4.9). After wafer

dicing and stripping of the photoresist the remaining buried oxide is removed in a buffered hydrofluoric acid bath. Since a thin silicon shutter does not block the entire light, a gold layer is deposited by e-beam evaporation. Finally, the fibers are inserted and bonded with UV-sensitive glue.

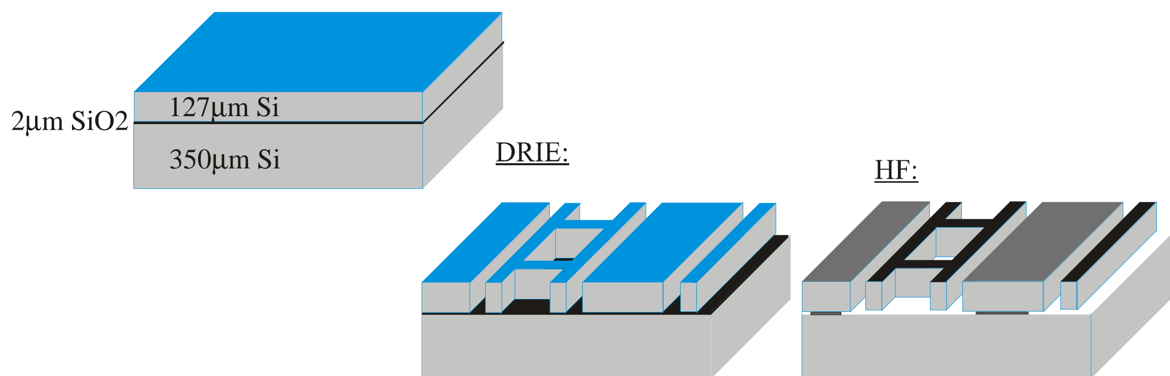

Fig.4.9 : Fabrication steps from left to right.

After fabrication, the accelerometer structure was analyzed using the scanning electron microscope. Due to photoresist mask under-etching and local over-etching at the silicon – oxide interface the final structures differ slightly from the design parameters. The distance between the damping plates was measured to be 8 µm rather than the desired 7 µm. The suspension beam thickness is 8.5 µm rather than 10 µm and the moving structure height is around 100 µm instead of 115 µm. The corrected geometrical parameters are used for the frequency response calculation (fig. 4.13).

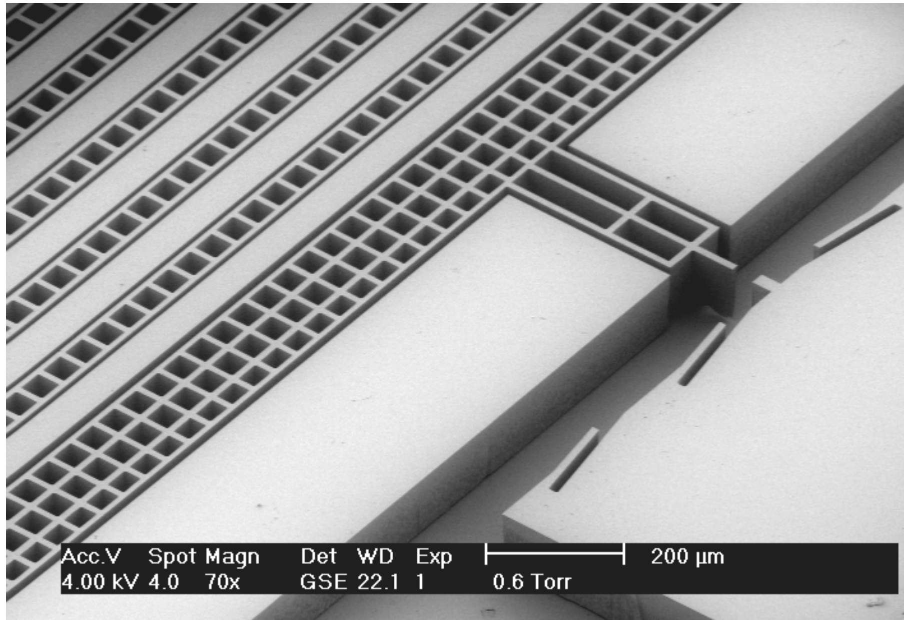

Fig. 4.10*: View of a shutter and fiber grooves. Fiber clamps are along the goove. Squeeze film is obtained with the air gaps of 8 microns between the mass (structures with square holes) and the frame.*

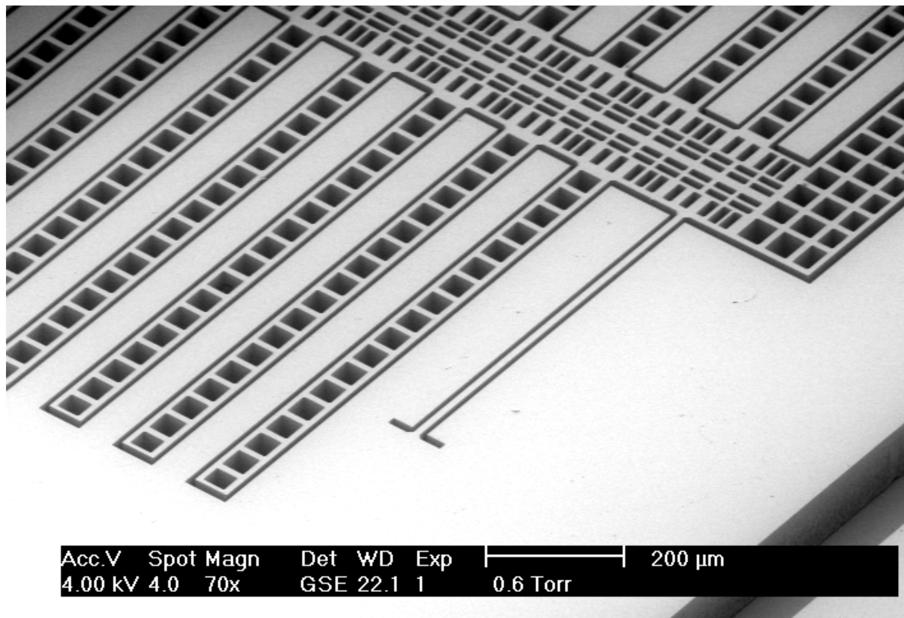

Fig.4.11: Corner view with of the mass with a suspension beam. On the bottom right side the same fiber groove as shown in Fig. 4.2 is visible. The side dampers appear to the left.

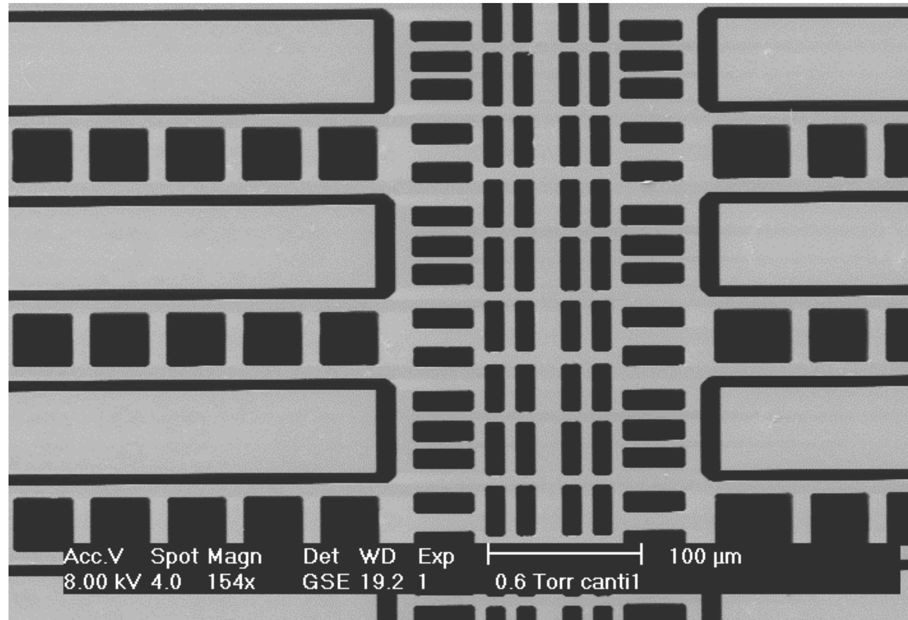

Fig. 4.12: SEM picture of the mass and damping plate structures from the top.

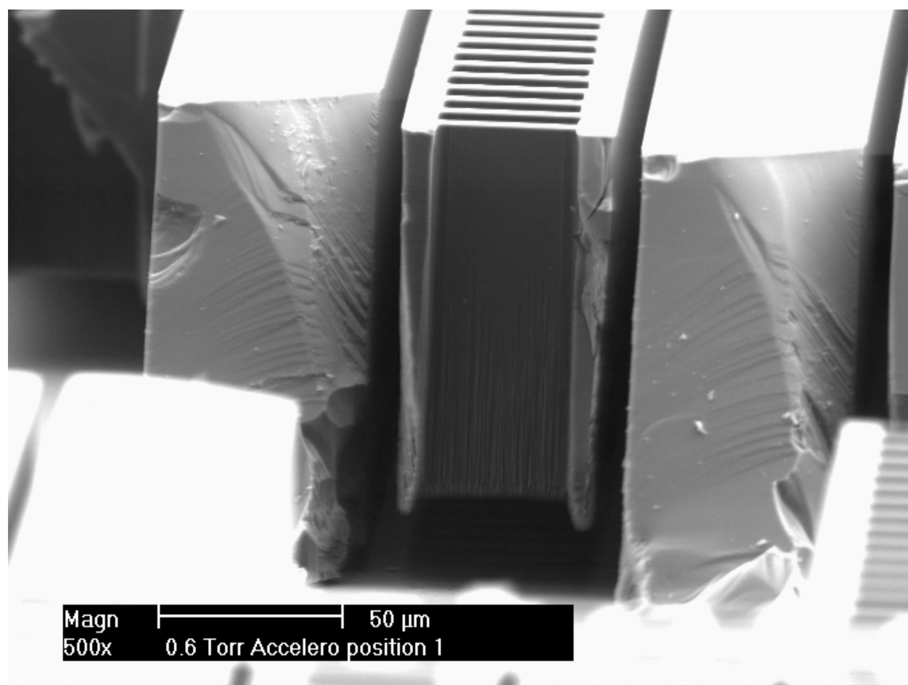

fig. 4.13: SEM picture of broken damping structures. Under-etched and released mass damping structures can be seen. The air film is 8 µm thick. The square shaped holes in the damping structures form an ambient air pressure reservoir and allow the plate structure to be released in a BHF bath.

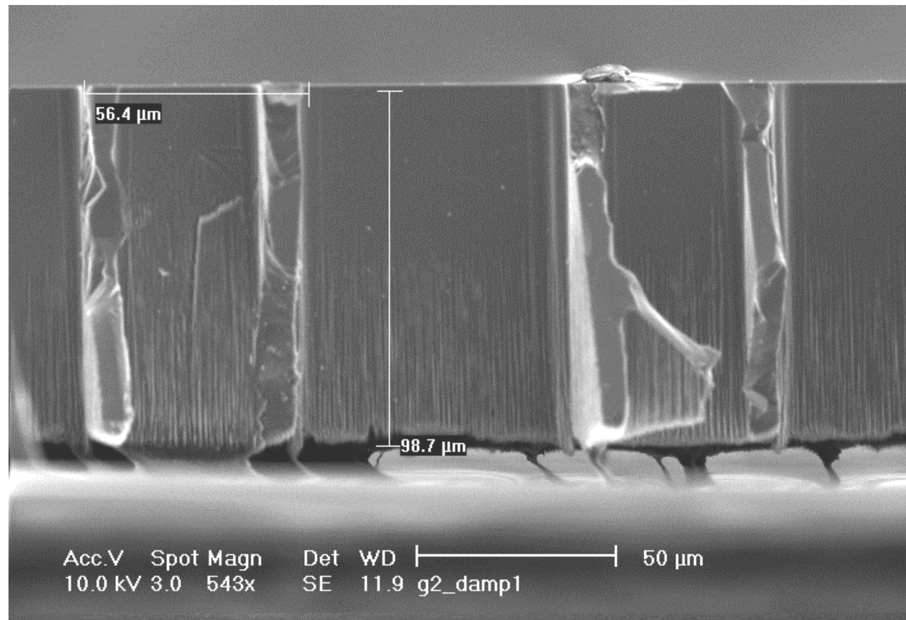

Fig. 4.14: SEM picture of a broken accelerometer mass structure on a conductive tape. The initially 125 µm thick silicon layer has been reduced to a thickness of around 100 µm during fabrication, due to plasma over-etching at the oxide-silicon interface.

4.5. Characterization

Characterization was done using an LED light source. Each of the two accelerometer output fibers was connected to a photodiode (fig. 4.3). Both photo currents were then amplified with photodiode amplifiers. The final accelerometer signal is then the normalized difference of the two amplifier voltages. Frequency response (Fig. 4.13) and amplitude response (Fig. 4.12) were measured using a lock-in amplifier. The frequency response was measured for a partially damped accelerometer and a well damped accelerometer. The partially damped accelerometers are obtained by removing the fixed main damping plates. This is realized with a longer

silicon oxide etching bath in BHF. With the partially damped accelerometer, the resonance frequency could be easily extracted since the peak appears clearly. It resulted in a resonance frequency of 1.6 kHz. Amplitude response measurement (Fig. 4.14) is done at 250 Hz resulting in a linear measurement range of ±40g. An optimized set-up resulted in a sensitivity of 100mV/g for a photodiode amplifier bandwidth of 500Hz. The standard deviation of the accelerometer output signal was below 2 mV when the shaker was switched off. This results in a dynamic range of 2000. The measured frequency responses were consistent with the calculated ones (fig 4.15). For the damped accelerometer, the damping factor was around 0.4, and for the partially damped, 0.2.

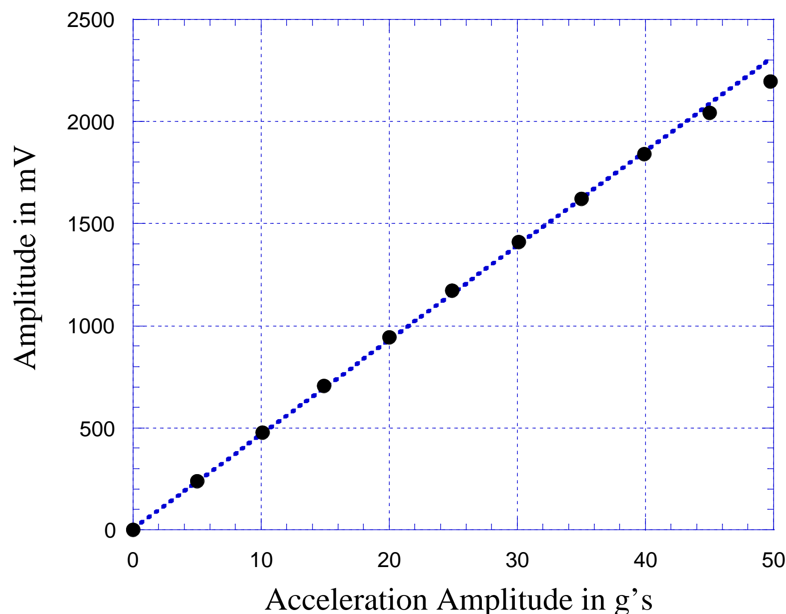

Fig. 4.14: Amplitude response at 250 Hz.

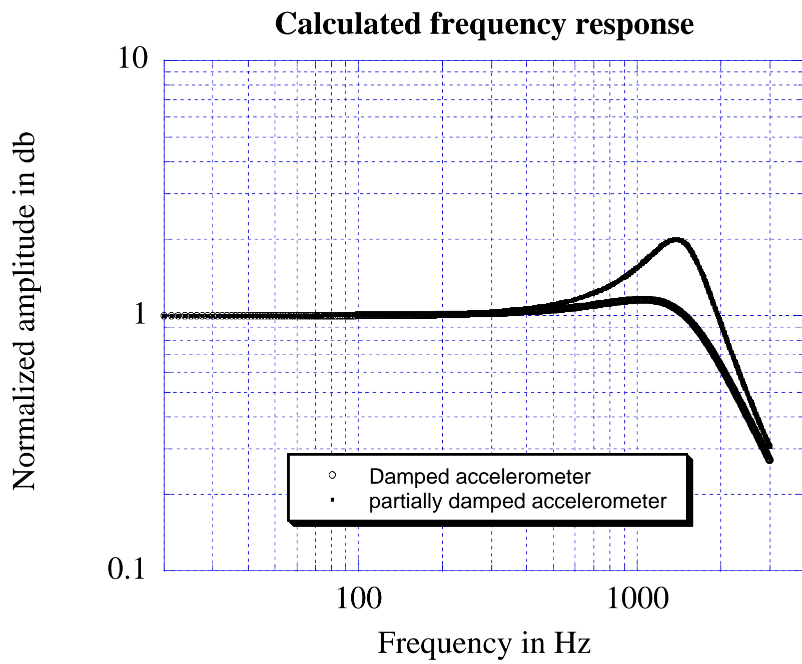

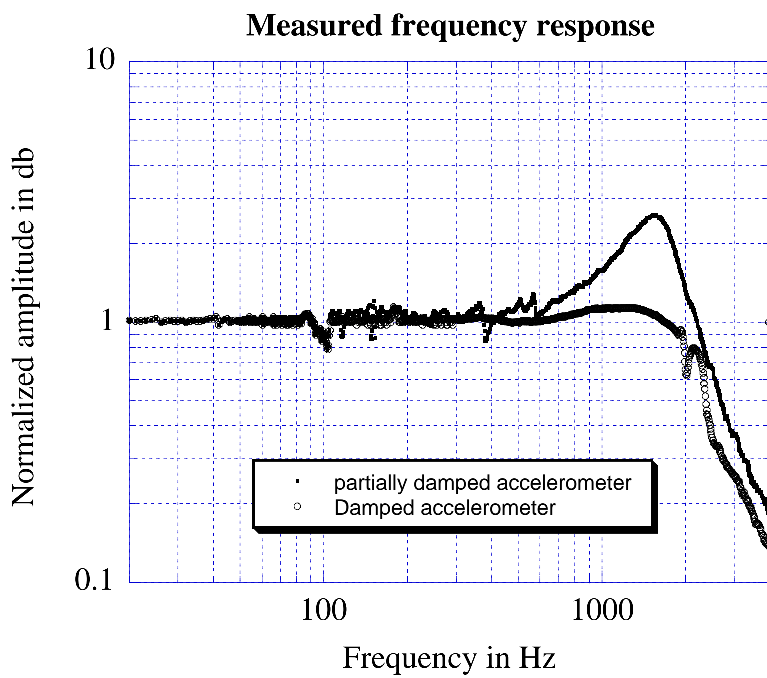

Fig. 4.15: Calculated and measured frequency response at 1g acceleration amplitude.

Light source power fluctuation rejection test

In order to quantify the immunity of the accelerometer signal to light source intensity fluctuations, a SLD light source was preferred. Because the control electronics displayed the output power of the SLD, light power variations could easily be controlled. The experiment involved measuring eventual acceleration amplitude changes for a varying light source power. During this experiment the shaker amplitude (20 g) and frequency (133 Hz) were kept constant. The accelerometer output voltage was indicated by a voltmeter. For an SLD output power of 68 μW down to 10 μW the (RMS) amplitude remained constant at 981 mV. At 6 μW, the measured amplitude droped slightly to 976 mV. For a tenfold light source power drop the output signal change was about 0.5%. The measurement error of the voltmeter was about 0.1 % according to its specs.

4.6 Conclusions

The combination of DRIE and multimode optical fibers made possible the fabrication of a damped fiber-optic based accelerometer with differential detection using one single mask. It is to our knowledge the first damped, optical fiber-based, MEMS accelerometer with a reasonable linear amplitude response and acceleration direction detection capacity. The device published by Asea [2] was damped but most probably had non-linearity problems [6]. The careful damping structure design considerations were adequate, since frequency response calculations were consistent with the measured

characteristics. A measurement range of ± 40 g with 20 mg resolution were obtained. The normalized differential accelerometer signal output proved to be insensitive to large low frequency fluctuations of light power.

References:

[1] Thomas Tschan, “Simulation, Design and characterization of a silicon piezoresistive accelerometer, fabricated by a bipolar-compatible industrial process”, Dissertation, Uni Neuchâtel, 1992

[2] C. Ovrén, M. Adolfsson and B. Hök, “Fiber optic systems for temperature and vibration measurements in industrial applications”, Optics and Lasers in Engineering, 5 (1984), 155-172.

[3] W. Bohl, “Technische Strömungslehre”, Vogel, Buchverlag Würzburg, pp. 22-24

[4] J. Starr, “Squeeze-film damping in solid-state accelerometers”, Tech. Digest IEEE, Solid state sensor and actuator workshop, 1990, 44-47

[5] J. Blech, “Squeeze films”, Technion report EEC-111, (March 1981)

[6] K. M. Taylor, “Misalignment losses in fiber optic joints due to angular misalignment for arbitrary energy distribution”, Opt. Eng. 34 (1995), 12, 3471-3479

5 Fiber optic MEMS accelerometer with high mass displacement resolution

In the previous chapter a micro shutter modulated optical fiber MEMS accelerometer with integrated damping structures has been designed, fabricated and characterized. The goal of the third generation accelerometer presented in this chapter is to use the same detection principle as the two first generations but optimized for a high seismic mass displacement resolution. Seismic mass displacement resolution determines the dynamic range of an accelerometer and therefore also the lowest detectable acceleration amplitude.

5.1 detection electronics

Here, mass displacement resolution depends on two factors, the voltage change detected for a certain displacement (V/μm) and on how well a certain voltage change can be resolved (mV). Dividing the second factor by the first gives the displacement resolution. The first factor depends on the amount of light power converted into electrons for a certain mass displacement multiplied by the current to voltage conversion resistance (A/μm * V/A). The limited or fixed parameters are the LED emission power P (W), the quantum efficiency of the photodiode η (A/W) and the coupling rate from

the input fiber to an output fiber (1/µm). The free parameter involves the current to voltage conversion (V/A). The second factor, which is the noise level on the output voltage, depends on the photo current as well as on the way this current is converted and amplified [1]. In the present case the detection is theoretically limited by the shot noise. However in practice it is observed that the current amplifier introduces a 1/f noise. In order to avoid or reduce the 1/f noise a modulated light source and a synchronous detection are required.

The second generation accelerometer was amplified with the DC component. The normalized differential of the signals was calculated using numerical electronics. It had the advantage of a low DC drift of the division calculation compared to an analog electronics. However the numerical electronics available on place had its limits.

For the third generation accelerometer an analog solution must therefore be found which is also able to eliminate LED power fluctuation effects. ABB [2] published a referenced optical fiber accelerometer where the power fluctuations of the light source are detected and attenuated by a control circuit fed back to the LED driver circuit. Power fluctuations on the input fiber can therefore be eliminated using an analog electronic. This requires in the present case, like for the second generation, a differential measurement approach. Both photo-currents converted into voltages are therefore amplified by a differential amplifier. The sum of both voltages is proportional to the light emitted by the input fiber and can be used as a feedback signal. The feedback control part of the electronic circuitry is however not executed in this work. The detection electronics for the third generation accelerometer is shown in figure 5.1.

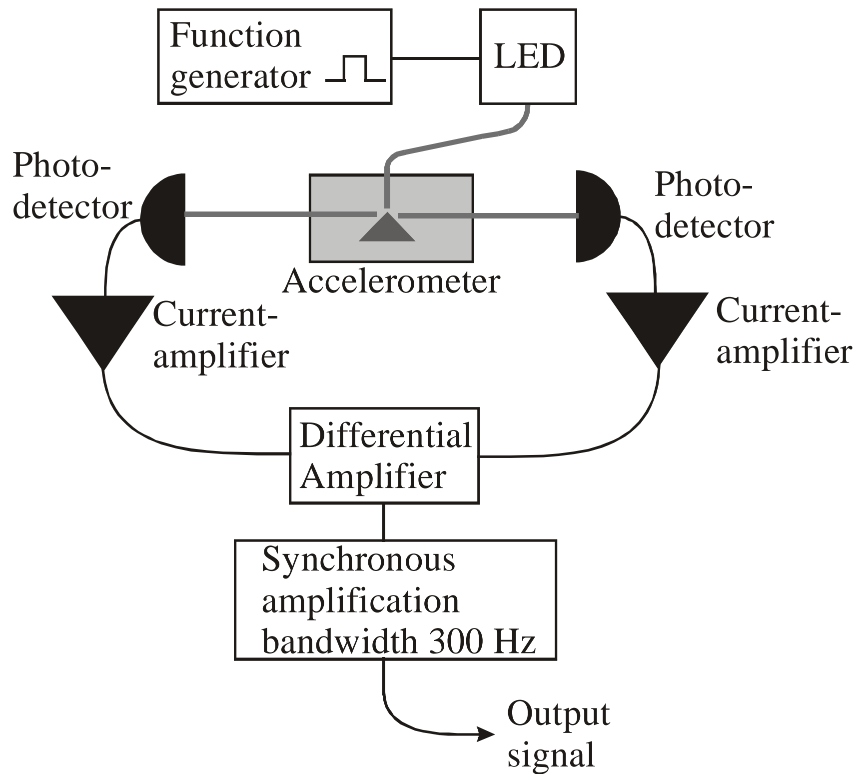

Figure 5.1: Detection electronics

5.2 Accelerometer design considerations

The first two generation accelerometers are based on shutter modulation. This allows a light power coupling between two fibers without being dependent on micro-machined surface quality of the silicon. However this method has the drawback that around the half of the light power is lost. These losses can be reduced using a reflecting beam splitter (fig. 5.2). The arrow shaped beam-splitter approach allows also to get rid of the fiber splitter used in the second generation.

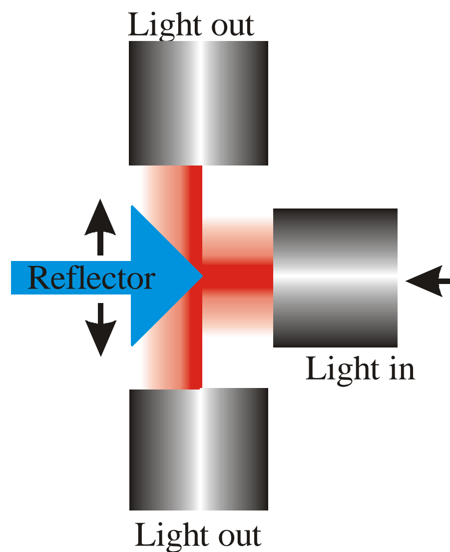

Figure 5.2: displacement detection principle using a reflective beamsplitter

The previous chapter showed that with a single mask process an accelerometer with integrated squeezed air film damping working at ambient pressure can be fabricated. In this chapter the damping structures are simplified with the risk that the conditions for the analytical model to be valid are not fulfilled. The experimental part of the damping is not discussed in this chapter. The other mechanical design parameters are:

Mass	$1.09*10^{-3}$ g
Resonance frequency	1.77 kHz
Suspension beam stiffness	135.5 N/m
Mass displacement sensitivity	80 nm/g

Fabrication process is the same as in the previous chapter. Figure 5.3 shows the overall working principle of the designed and fabricated accelerometer (figure 5.4) and figure 5.5 shows a picture of a fiber-bonded device.

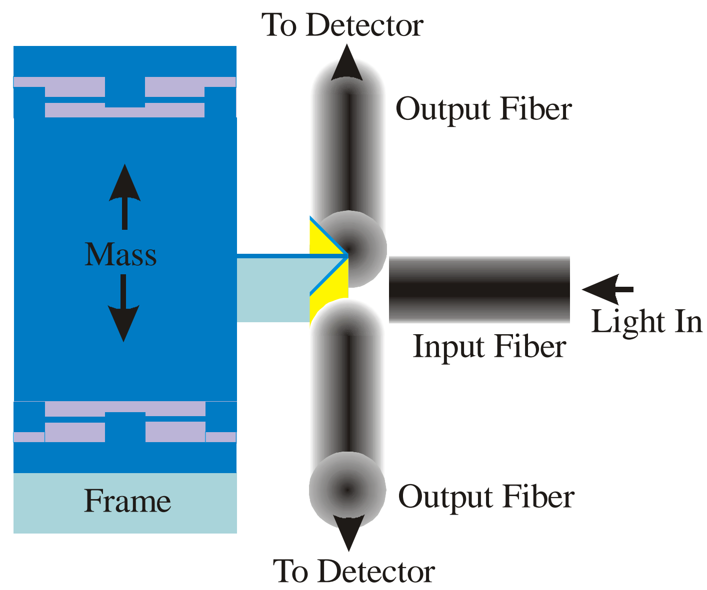

Figure 5.3: functional principle of the third accelerometer

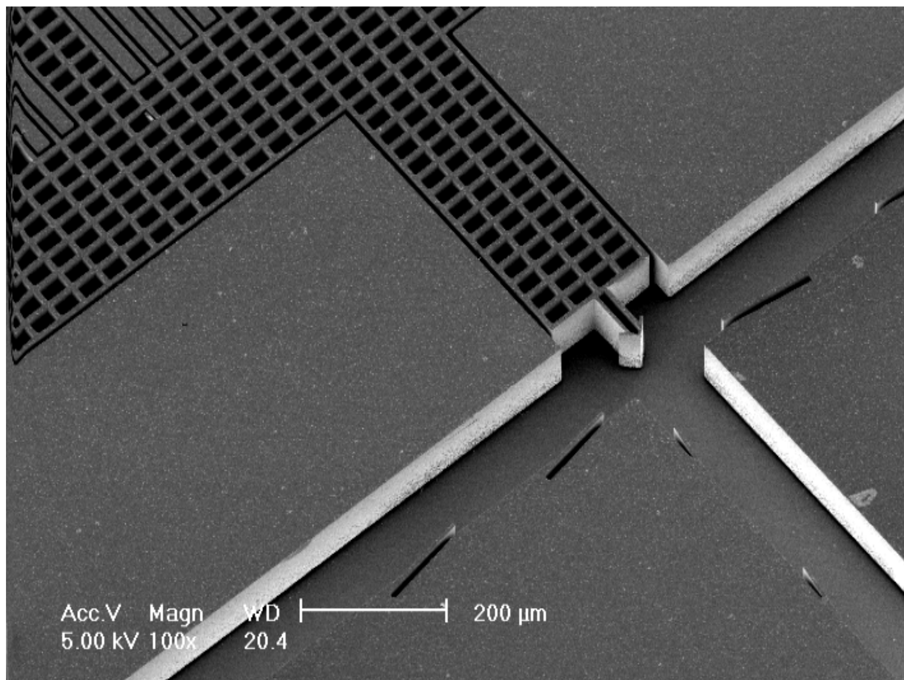

Figure 5.4: SEM picture of the arrow shaped reflector with the optical fiber grooves and clamps.

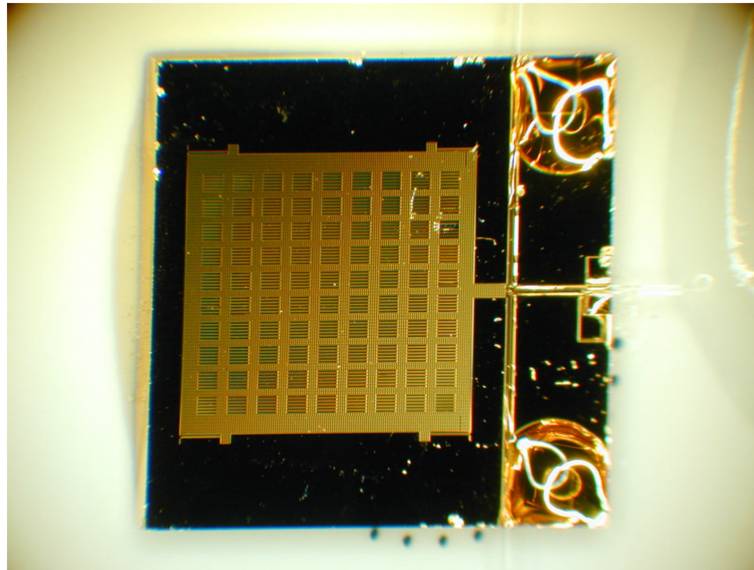

Figure 5.5: Picture of a fiber bonded chip. The damping structures integrated on the mass and the T-shaped fiber arrangement with UV-glue dots on the right corners can be seen.

5.3 Characterization

Frequency and amplitude response (fig. 5.6 and 5.7) measurement is done using a LED source connected to the input fiber. Each output fiber is connected to a photodiode. After differential amplification of the photo-currents the output signal is read. Response, for damped and undamped devices are shown (Fig. 5.6). The analytical model being consistent with measurements the mass displacement under a given acceleration is determined (80nm/g). Amplitude response at 65 Hz is linear up to ±6 g.

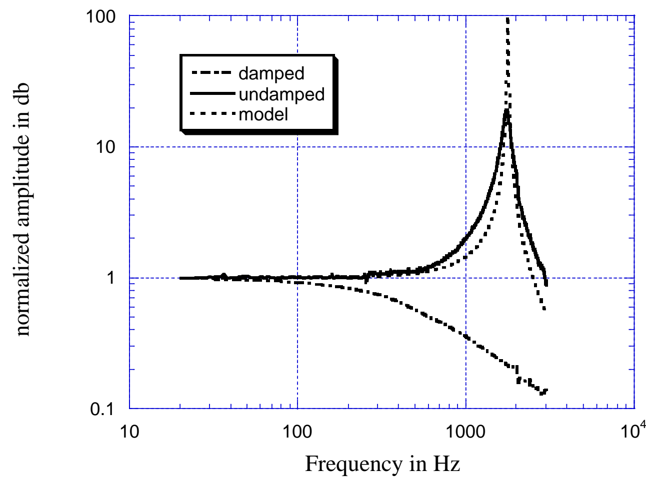

Figure 5.6 : Frequency response measurement at 1 g. The analytical model is consistent with the measured response.

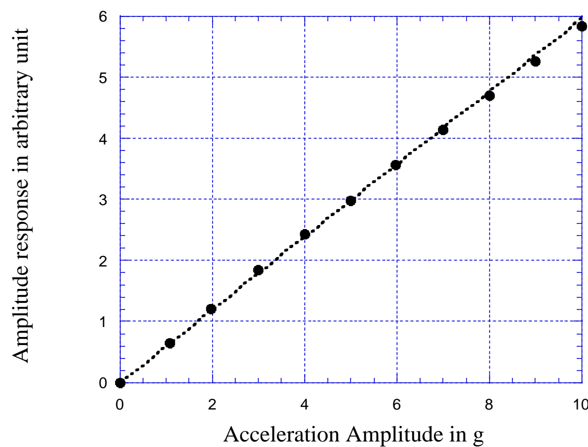

Figure 5.7: Amplitude response measurement at 65 Hz

Then the accelerometer is optimized and set to the working mode (±10V for ±6 g) by modulating the LED and using synchronous amplification of the differential signal with a bandwidth of 300 Hz (fig. 5.1). A sensitivity of 1.66V/g at 65 Hz over ±6g is measured. The noise level on the output voltage is measured on two ways, with a spectrum analyzer (62 µV/√Hz)

(fig. 5.6) and with a standard deviation measurement on an acquisition card (1mV). These noise levels correspond to a mass displacement of 0.055 nm or an acceleration of 0.67 mg.

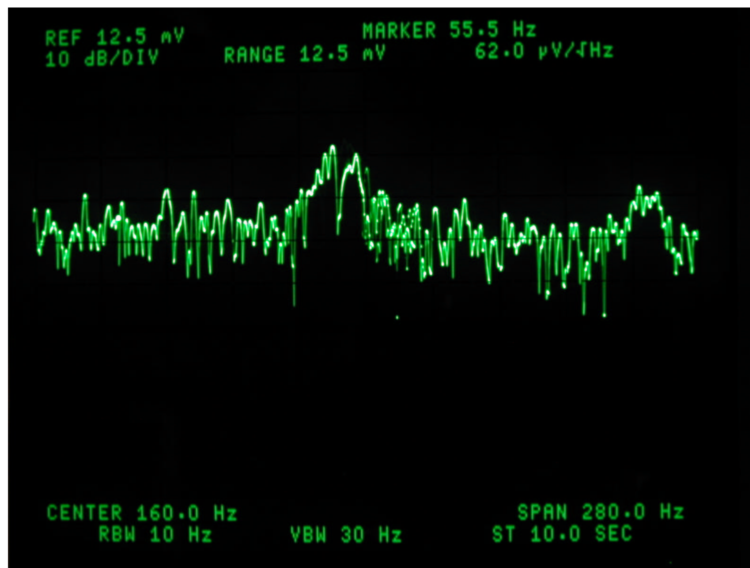

Figure 5.8: Noise level measured on the spectrum analyzer. The peaks at 150Hz and 250Hz are probably noise components from the power net.

5.4 Conclusions

With a single DRIE etch step, multi-mode optical fibers, an LED and synchronous detection electronics a squeezed air film damped accelerometer having a mass displacement resolution in the order of an angström for a bandwidth of 300 Hz has been made possible. An estimated displacement resolution in the order of an Angström outperforms previously published intensity modulated devices [3,4] and is comparable to a more sophisticated and expensive Fabry-Perot based device [5] with an estimated resolution of 0.085 nm. Table 5.1 shows the updated list of the fiber optic MEMS accelerometers published or to be published up to now.

Table 1.1: Fiber Optic MEMS Accelerometers up to 2001. The italic written rows correspond to an accelerometer based on a wavelength dependent detection method.

	Dyn. range	Displacement resolution	referenced	Damped resonance	Fabrication complication	Component costs
1984 [2]	-	-	yes	yes	2	low
1992 [6]	-	-	no	no	2	moderate
1992 [7]	-	-	no	no	2	moderate
1995 [8]	700	-	yes	no	3	low
1996 [10]	-	-	*yes*	*no*	*3*	*high*
1997 [9]	1400	10nm	yes	no	2	moderate
1998 [11]	-	-	*yes*	*no*	*2*	*high*
1998 [5]	*10000*	*1Angst.*	*yes*	*no*	*2*	*high*
2000 [4]	2000	1 nm	no	no	2	low
2001 [12]	2000	-	yes	yes	1	low
2001 [13]	9000	1 Angst.	no	yes	1	low

References:

[1] B.E.A Saleh, M.C. Teich, “Fundamentals of photonics” John Wiley and sons, 1991.

[2] C. Ovrén, M. Adolfsson and B. Hök, “Fiber optic systems for temperature and vibration measurements in industrial applications”, Optics and Lasers in Engineering, 5 (1984), 155-172.

[3] Ollier E., P. Lebey and P. Mottier," Integrated micro-opto-mechanical vibrations sensor connected to optical fibers" Electron. Letters, 6, 525-526, 1997.

[4] B. Guldimann, P. Thiébaud, N. de Rooij "Micromachined, fiber optic based accelerometer with shutter modulation," Proc. IEEE, MEMS 2000, 710-714.

[5] G. Schröpfer et al. "Lateral optical accelerometer micromachined in (100) silicon with remote readout based on coherence modulation", Sensors and Actuators, A 68 (1998), 344-349.

[6] K. Burcham, G.N. De Brabander and J.T. Boyd, "Micromachined silicon cantilever beam incorporating an integrated optical waveguide", SPIE 1793, (1992), 12-18.

[7] D. Uttamchandani, D. Liang and B. Culshaw, "A micromachined silicon accelerometer with fiber optic interrogation", SPIE 1792, (1992), 27-33.

[8] J. Marty, A. Malki, C. Renouf, P. Lecoy, F. Baillieu, "Fiber-Optic accelerometer using silicon micromachined techniques", Sensors and Actuators A 46-47 (1995), 470-473.

[9] E. Ollier, P. Lebey and P. Mottier, "Integrated micro-opto-mechanical vibration sensor connected to optical fibers", Electron. Lett. (1997), 6, 525-526.

[10] Dan Haronian, "Geometrical modulation-based interferometry for displacement sensing using optically coupled suspended waveguides", J. MEMS Vol. 7, Nr. 3, (1998), 309-314.

[11] T. Storgaard-Larsen, S. Bouwstra, O. Leistiko, "Opto-mechanical accelerometer based on strain sensing by a Bragg grating in a planar waveguide", Sensors and Actuators A52 (1996) 25-32.

[12] B. Guldimann, P.A. Clerc, N.F. De Rooij, "Fiber optic MEMS accelerometer with integrated damping", Proc. IEEE Optical MEMS 2000, 141-142.

[13] B. Guldimann, Ph. Dubois, P.A. Clerc, N.F. De Rooij, "Fiber optic MEMS accelerometer with high mass displacement resolution", Proc. Transducers'01, to be published.

6. Conclusions

The approach of the presented work was based on the principle of a maximal simplicity in theory, design, fabrication, light source and detection means. The first chapter analyzed therefore the simplest micro-opto-mechanical approach to obtain a displacement response similar to the response of a single segment of a segmented photodiode. In order to show the principle on a working device, a simple accelerometer was presented. This was done in chapter 3. It shows that a displacement resolution of 1nm can be reached which is already a factor 10 better compared to another intensity modulated device published recently. Chapter 4 showed how the fabrication process can be simplified to a single mask process and how damped resonance and immunity to light source fluctuations can be reached. This chapter demonstrated how damping structures can be integrated into a fiber optic based accelerometer without increasing fabrication and packaging complications. Chapter 5 presented an accelerometer with a mass displacement detection principle based on a micromachined beam-splitter. This mass displacement detection principle is inspired by the conventional light beam position detection principle based on a segmented photodiode. The accelerometer had integrated damping structures, a dynamic range close to 40 dB and an estimated mass displacement detection resolution below an Angström over a bandwidth of 300 Hz. This represented an improvement of again a factor ten compared to the device of chapter 3 and has a

displacement resolution equivalent to a more expensive and clearly more sophisticated Fabry-Perrot based device.

Acknowledgments

First I want to express my extreme gratitude to Professor Nico de Rooij, that he hired me to work in his very well equipped Sensors, Actuators and Microsystems Laboratory (SAMLAB) of the Institute of Microtechnology (IMT). During four years I really appreciated the very high degree of freedom, support and confidence he offered me in my endeavors. He always said “pas de problèmes” when I wanted to go to a conference on Japan, Hawaii and so on.

Special thanks, to the co-examiners of my thesis, namely Hans-Peter Herzig, assistant Professor in Applied Optics at the IMT, and Cornel Marxer, director of Sercalo Ltd.

This work has only been possible with the highly skilled SAMLAB staff. Special thanks to Pierre-André Clerc for his very successful efforts and perseverance in all deep reactive ion etching process developments, as well as his flexibility and high degree of motivation. Many thanks to Gianni Mondin for his flexibility, efficiency and always competent advises. Thanks also to Sylvain Jeanneret for managing the extremely well equipped laboratory and Sylviane Pochon for all bonding advises and wafer dicings. Also many thanks to the SEM team, Massoud Dadras and Mireille Leboef.

A special thank to Dr. Balmer, the best head of the mechanical shop the CSEM ever had, for all his suggestions, his high quality and high speed executions of the work, as well as the interesting discussions.

I'm extremely grateful to Pierre Thiébaud, who voluntarily introduced me into the clean room and taught me microfabrication. In the same time I want to thank Cynthia Beuret and George Racine for all their help and sharing their huge lab experience. I also want to thank Cornel Marxer for the use of his fiber bonding infrastructure at Sercalo and all the interesting discussions.

Thanks very much to Sabeth Verpoorte for all her more than just english text corrections (abstracts, articles, thesis) and suggestions. Many thanks also to Bart van der Schoot for advising and encouraging me in all my important work strategies.

During the past four years, I regularly needed computer support from Mathias Schulz, Christophe Kottelat, Claudio Novelli as well as Laurent Dellmann.

In alphabetic order I want specially thank:

Terunobu Akiyama for many fruitful discussions on AFM's and Japan. Vincent Auger for the funny beach-volley matches. Marc Boillat from Seyonic SA for having supervised me on the flow-sensor project. Danick Briand for sharing his lab experience and especially for sharing the office with me (he deserves a diploma) and the now mythical chesterton water pump (he needed ear protections). Laura Ceriotti for the italian lessons.

Antoine Daridon and Bas (coffie) de Heij for taking the coffee break with me. Laurent Dellmann for his patience with my computer (un-)skills, taking SEM pictures, sharing his lab experience and for the pleasant time at the conferences and on the snowy slopes in Verbier. Arash Dodge for the funny beach-volley matches. Philippe Dubois for sharing his lab experience, helping me in the lab when I had a conference deadline to hold and the pleasant time spent on the snowy slopes. Olivier Guenat, for sharing his experience, always motivating me in my endeavors and all the interesting discussions. Andreas Kuoni for his sharing his micro fluidic and rotating machinery experience. Gian-Luca Lettieri for the funny beach-volley matches. Jan Lichtenberg for the great bike tours and barbecues. Gregor Schürmann for teaching me the only relative importance of snowboarding and work. Urs Staufer for his very good physicist eye and therefore for the good questions on my work. Peter Van der Waal, from Friesland, for the very useful epoxy advises, taking care on the books and articles I ordered and for all the good beer evenings.